DEVELOPMENT OF TRANSITION-METAL DOPED Cu_2O AND ZnO DILUTE MAGNETIC SEMICONDUCTORS

By

MATHEW P. IVILL

A DISSERTATION PRESENTED TO THE GRADUATE SCHOOL
OF THE UNIVERSITY OF FLORIDA IN PARTIAL FULFILLMENT
OF THE REQUIREMENTS FOR THE DEGREE OF
DOCTOR OF PHILOSOPHY

UNIVERSITY OF FLORIDA

2007

© 2007 Mathew P. Ivill

To my family and friends, especially to my parents and Kathryn, for their love and support.

ACKNOWLEDGMENTS

Graduate school has proven to be quite a wild ride, filled with moments of great accomplishment, balanced with moments of insane frustration. Luckily, I've had the privilege of collaborating with amazing people who have helped me while I worked on this dissertation. It would be impossible to list everyone who has helped. Nevertheless, I will do my best to name those who made my years (and all the many hours and late nights in the lab) at the University of Florida an educational, memorable, and enjoyable experience.

First of all, I thank my advisor, Dr. David Norton, for taking me into his research group. I am deeply grateful for his constant encouragement and support throughout my graduate studies. He has helped me grow both academically and personally, and has been an exceptional role model. Without his help this dissertation would not be possible. I also thank the other members of my committee: Dr. Stephen Pearton, Dr. Cammy Abernathy, Dr. Art Hebard, and Dr. Susan Sinnott for their help and guidance.

I am grateful to Dr. Brent Gila, a person who possesses a vast amount of practical knowledge. I learned something new every time we chatted in lab.

I've spent many enjoyable hours working with my fellow group members. I am happy to thank them all, both past and present, for their support and friendship in and out of the lab, including Dr. Seh-Jin Park, Dr. Beong-Seong Jeong, Dr. Hyung-jin (Johnny) Bae, Dr. Kyunghoon Kim, Dr. Jennifer Sigman, Dr. George Erie, Dr. Yaunjie Li, Dr. Seemant Rawal, Mitesh Patel, Vijayram Varadarajan, Micheal Jones, Hyunsik Kim, Li-Chia Tien, Patrick Sadik, Charlee Callender, Lii-Cherng (Daniel) Leu, Joe Cianfrone, Fernando Lugo, Ryan Pate and Zivin Park. I am especially grateful to both Dr. Young-Woo Heo and Dr. Yongwook Kwon, both of whom took me under their wing when I started graduate school, and whose kindness and personality have been a great inspiration. Young-Woo taught me many of the lab techniques I used throughout grad school, including how to deposit films using PLD, and was always kind enough to lend a hand with my research, even when he was extremely busy with his own. Yongwook also taught me many things; he introduced

me to LabView programming, electrical characterization, and also taught me some Kendo along the way! I wish them all great success and happiness.

I thank the members of Dr. Abernathy's research group, including Dr. Rachel Frazier, Dr. Jennifer Hite, and Dr. Gerald Thaler for discussions pertaining to magnetic semiconductors. I also thank my collaborators and friends from the physics department, Ritesh Das, Dr. Josh Kelly, and Dr. Ryan Rairigh for providing the SQUID measurements presented in this dissertation and their insightful discussions interpreting the data.
Also Rajiv Misra who offered some very useful advice regarding electrical transport measurements.

I thank Dr. John Budai and Dr. Matthew Chisholm for collaboration with high-resolution XRD and TEM on selected samples. I also thank Dr. Valentin Craciun and Eric Lambers from the Major Analytical Instrumentation Center (MAIC) for their help with material characterization using XRD and XPS.

I thank Dr. Sarah Russell Gonzalez, one of the friendliest people I know, for introducing me to the LaTeX typesetting program in which this dissertation was written.

I thank my parents and my brother for their love and unwavering support. They've always been around when I needed them and they continue to support me in my decisions. I would have never made it this far without them and I am very fortunate to have them in my life.

Finally, I thank my fiancée, Kathryn Kennedy, for her endearing love and support (and hours of proofreading). She was always there to cheer me up when experiments went wrong, to inspire me when life became overly frustrating, and to celebrate with me when things finally went right.

TABLE OF CONTENTS

page

ACKNOWLEDGMENTS 4

LIST OF TABLES 9

LIST OF FIGURES 10

ABSTRACT 13

CHAPTER

1 INTRODUCTION 15

1.1 Charge and Spin 15
1.2 What is Spintronics? 16
1.3 Dilute Magnetic Semiconductors 17

2 REVIEW OF DILUTE MAGNETIC SEMICONDUCTORS 19

2.1 Magnetic Semiconducting Materials: A Short History 19
2.2 DMS Theory: The Physical Origins of Ferromagnetism in DMS 22
2.2.1 Dietl's Mean-field Theory 22
2.2.2 First-principles Design: DFT Calculations 23
2.2.3 Ferromagnetism in Disordered Alloys 24
2.2.4 Ferromagnetism in a Spin-split Conduction Band 25
2.3 Experimental Progress in ZnO DMS 26
2.3.1 Mn-doped ZnO 27
2.3.2 Co-doped ZnO 28

3 THIN FILM DEPOSITION AND EXPERIMENTATION 34

3.1 PLD as a Tool for Thin Film Oxides 34
3.2 PLD System Used for This Work 35
3.2.1 The Growth Environment 35
3.2.2 The Laser Source 36
3.3 Typical Growth Procedure 37
3.3.1 Substrate Preparation 37
3.3.2 Thin Film Growth 38
3.4 Fabricating PLD Ablation Targets 39
3.5 Thin Film Characterization 40
3.5.1 X-ray Diffraction 40
3.5.2 Magnetoresistance and Hall Effect Measurements 41
3.5.3 Electron Dispersive Spectroscopy (EDS) 42
3.5.4 Optical Absorption 43
3.5.5 SQUID 45

4 PROPERTIES OF Mn-DOPED Cu_2O DMS 49

4.1 Introduction 49
4.2 Cu_2O: A Wide-bandgap P-type Semiconductor 49
4.3 Experimental 51
4.4 Results and Discussion 52

5 PROPERTIES OF ZnO CODOPED WITH Mn AND Sn 70

5.1 Introduction 70
5.2 Experimental 71
5.3 Results and Discussion 71

6 PROPERTIES OF ZnO CODOPED WITH Mn AND P 82

6.1 Introduction 82
6.2 Experimental 82
6.3 Results and Discussion 83

7 PROPERTIES OF COBALT-DOPED ZnO 100

7.1 Introduction 100
7.2 Experimental 100
7.3 Results and Discussion 101
7.3.1 Chemical Composition 101
7.3.2 Structure and Phase Analysis 101
7.3.2.1 Films with precipitation 101
7.3.2.2 Films without precipitation 102
7.3.3 Optical Properties 103
7.3.3.1 Optical absorption 103
7.3.3.2 Photoluminescence 105
7.3.4 Magnetic Characterization 106
7.3.5 Electrical Transport 107
7.3.5.1 Hall effect 107
7.3.5.2 Magnetoresistance 110
7.3.6 Effects of Annealing 113

8 CONCLUSION 139

8.1 Mn-doped Cu_2O 139
8.2 Mn-doped ZnO 140
8.3 Co-doped ZnO 142

APPENDIX

A HALL EFFECT SYSTEM AND EQUIPMENT 144

A.1 Introduction 144
A.2 Hall Effect Equipment 144

A.3 Sample Geometry and Measurement Technique 147
A.4 Hall Effect Method 150
A.5 Limitations and Tips for Better Measurements 151

REFERENCES 157

BIOGRAPHICAL SKETCH 171

LIST OF TABLES

Table page

2-1 List of ZnO-based DMS experimental results 33

5-1 Resistivity as a function of Sn content in codoped ZnO:3%Mn films. 76

7-1 Possible cobalt-induced secondary phases. 116

7-2 Transport data for a 30%Co-doped ZnO film with cobalt precipitation. 132

LIST OF FIGURES

Figure page

2-1 Schematic representation of magnetic exchange between two Mn ions mediated by a delocalized hole. . . . 30

2-2 Predicted Curie temperatures based on Dietl's calculations . . . 31

2-3 Illustration of bound magnetic polarons. . . . 32

3-1 Schematic of pulsed laser deposition system. . . . 47

3-2 Visualization of Bragg's law for x-ray diffraction. . . . 48

4-1 Cubic unit cell of Cu_2O. . . . 57

4-2 Phase Stability curves for the Cu-Cu_2O-CuO system. . . . 58

4-3 X-ray diffraction data for epitaxial Cu_2O on (001) MgO . . . 58

4-4 X-ray diffraction data for Mn-doped Cu_2O films grown on (001) $MgAl_2O_4$ in an oxygen pressure of 1mTorr. . . . 59

4-5 X-ray diffraction data for Mn-doped Cu_2O films grown on (001) $MgAl_2O_4$ in an oxygen pressure of 0.1mTorr. . . . 60

4-6 X-ray diffraction data for Mn-doped Cu_2O films grown on (001) $MgAl_2O_4$ in vacuum. . . . 61

4-7 Phase assemblage for films grown under different conditions. . . . 62

4-8 Magnetic behavior for an epitaxial Mn-doped Cu_2O film grown at 300°C and 1mTorr of oxygen. . . . 63

4-9 Magnetic behavior for $MgAl_2O_4$ substrate. . . . 64

4-10 Magnetic behavior for an epitaxial Mn-doped Cu_2O film . . . 65

4-11 Low temperature photoluminescence spectra for Mn-doped Cu_2O films. . . . 66

4-12 Transport data for 1% Mn-doped Cu_2O films. . . . 67

4-13 Temperature-dependent transport data for 1% Mn-doped Cu_2O film. . . . 68

4-14 Field-varying transport measurements for a 1% Mn-doped Cu_2O film. . . . 69

5-1 X-ray diffraction of ZnO films codoped with Mn and Sn . . . 77

5-2 X-ray diffraction of an epitaxial ZnO film doped with 3%Mn and 0.1%Sn . . . 78

5-3 XPS spectra for ZnO:3%Mn film codoped with 0.01%Sn. . . . 79

5-4 Plot showing the dependence of the coercive field on Sn concentration at different SQUID measurement temperatures. 80

5-5 Magnetization measured at 300K for epitaxial ZnO:3%Mn films that are codoped with 0.001% Sn, 0.01%Sn, 0.1% Sn, and no Sn. 81

6-1 X-ray diffraction of ZnO films codoped with Mn and P both before and after annealing. 90

6-2 High-resolution ω-rocking curves on ZnO films codoped with Mn and P before and after annealing. 91

6-3 AFM scans on epitaxial ZnO:3%Mn, 2%P films before and after annealing. . . . 92

6-4 Resistivity and carrier concentration behavior of P-doped ZnO films. 93

6-5 Transport data for the as-deposited ZnO:3%Mn, 2%P film at 300K. 94

6-6 XPS spectra for ZnO:3%Mn film codoped with 2% P. 95

6-7 Room temperature optical transmission for ZnO:3%Mn, 2%P films 96

6-8 Room temperature SQUID measurements for epitaxial ZnO:3%Mn,2%P films . 97

6-9 SQUID measurement at 10K for epitaxial ZnO:3%Mn, 2%P films before and after annealing. 98

6-10 Field-cooled and zero field-cooled magnetization measurements for a ZnO:3%Mn, 2%P film annealed at 600C in O_2. 99

7-1 EDS results for a select number of films grown under different conditions. 116

7-2 XRD scans for a series of films grown in vacuum at 400°C. 117

7-3 TEM micrographs of a sample doped with 30%Co 118

7-4 Convergent beam TEM diffraction patterns of ZnO film doped with 30%Co . . . 119

7-5 XRD scans for ZnO films doped with 30%Co. 120

7-6 Thermodynamic predominance diagram for cobalt oxides. 121

7-7 UV-Vis transmission of Co-doped ZnO films 122

7-8 Optical band-gaps of Co-doped ZnO films. 123

7-9 PL results for Co-doped ZnO films 124

7-10 SQUID magnetization curves for Co-doped ZnO films deposited at 400°C in vacuum. 125

7-11 SQUID magnetization curves for Co-doped ZnO films 126

7-12 Anomalous Hall effect in 30%Co-doped ZnO. 127

7-13 The magnetoresistance of an undoped ZnO film. 128

7-14 The magnetoresistance of 5%Co-doped ZnO films. 129

7-15 Magnetoresistance of 30%Co-doped ZnO films. 130

7-16 Magnetoresistance of 30%Co-doped ZnO film at temperatures between 10K to 100K. 131

7-17 Temperature dependent resistivity measurements for 5% and 30% Co-doped ZnO films. 132

7-18 Hall resistivity and magnetoresistance for a 30%Co-doped ZnO film with cobalt precipitation. 133

7-19 SEM micrographs at different magnifications of the surface of a Co-doped ZnO film that has been annealed in H_2/Ar at 500°C for 60min. 134

7-20 θ-2θ XRD for a 30%Co-doped ZnO film before and after annealing in forming gas at 500°C. 135

7-21 High-resolution XRD scans for 30%Co-doped ZnO film that has been annealed in forming gas at 500°C. 136

7-22 SQUID magnetometry for a 30%Co-doped ZnO film before and after annealing in forming gas at 500°C. 137

7-23 SQUID magnetometry for 30%Co-doped ZnO films deposited under differerent conditions. 138

A-1 The resistivity and Hall measurement system. 154

A-2 Circuit diagrams for 2-point and 4-point resistivity measurements. 155

A-3 Circuit shunt capacitance and settling time. 156

Abstract of Dissertation Presented to the Graduate School
of the University of Florida in Partial Fulfillment of the
Requirements for the Degree of Doctor of Philosophy

DEVELOPMENT OF TRANSITION-METAL DOPED Cu_2O AND ZnO DILUTE MAGNETIC SEMICONDUCTORS

By

Mathew P. Ivill

August 2007

Chair: Dr. David Norton
Major: Materials Science and Engineering

The field of spintronics has recently attracted much attention because of its potential to provide new functionalities and enhanced performance in conventional electronic devices. Oxide materials provide a convenient platform to study the spin-based functionality in host semiconducting material. Recent theoretical treatments predict that wide band-gap semiconductors, including ZnO, can exhibit high temperature ferromagnetic ordering when doped with transition metals. This work focused on the possibility of using wide band-gap oxide semiconductors as potential spintronic materials. The structure, magnetic, and electronic transport properties of transition-metal doped ZnO and Cu_2O were investigated. Mn and Co were used as transition metal dopants. Thin films of these materials were fabricated using pulsed laser deposition (PLD).

The Mn solubility in Cu_2O was found to be small and the precipitation of Mn-oxides was favored at high growth temperatures. Phase pure Mn-doped Cu_2O samples were found to be non-magnetic. Samples were p-type with carrier concentrations on the order of 10^{14}–10^{16} cm^{-3}.

The effects of carrier concentration on the magnetic properties of Mn-doped ZnO were studied using Sn and P as electronic codopants. Sn acts as an n-type dopant providing extra electrons to the ZnO. P acts as a p-type dopant that supplies excess holes to compensate the native electron concentration in ZnO. The electron concentration was decreased using P, but the films remained n-type. An inverse correlation was found

between the ferromagnetism and the electron concentration; the ferromagnetic coupling between Mn spins increased with decreasing electron concentration.

The nature of ferromagnetism in Co-doped ZnO was also investigated. Ferromagnetism was found in films deposited at 400°C in vacuum, while films deposited in oxygen or at higher temperatures were non-magnetic. Films deposited under vacuum had rather high electron concentrations and were presumably doped with oxygen vacancies. The Co-doped films also exhibited peculiar magnetoresistance (MR) that had a strong dependence on the carrier concentration. At low temperatures, a progression from positive to negative MR was observed with increased electron concentration as the films crossed over the metal-to-insulator transition (MIT).

CHAPTER 1
INTRODUCTION

1.1 Charge and Spin

The microelectronics industry has been at the forefront of information technology, providing the devices necessary for fast and efficient information *processing* and *storage*. The integrated circuit, packed with transistor arrays fabricated from semiconducting silicon material, has remained the workhorse of the information *processing* industry over the past 50 years. These devices utilize the charge properties of electrons (or holes) to control the flow of current through the circuit. By the proper organization of transistors on a chip, information can be computed by the digital logic of electronic charge. Increase in the raw computational power and speed of these transistors over the past 50 years has been propelled by one important trend—miniaturization. Steadily following the early prediction by Gordon Moore (commonly called Moore's Law) miniaturization has led to the number of transistors on a chip to double about every 18 months. Intel's cutting-edge processors are currently fabricated with 65nm line-widths, and next generation 45nm architectures are hitting the market soon [1].

On the other hand, the technology of information *storage* relies on another fundamental property of electrons: the quantum mechanical electron spin. Magnetism in solids is a direct consequence of the spin property of electrons. Electrons have two available spin states, spin-up and spin-down. Permanent magnetic materials contain an imbalance in the number of spin-up and spin-down electrons. Binary information may be encoded in the form of non-volatile magnetic domains within the grains of ferromagnetic material. As the size of these domains shrink, more information can be stored per unit area of material. Increases in magnetic storage density have occurred at rates faster than any other industry in history, with storage density increasing over 50 million times since the creation of the first hard disk drive in 1957 [2]. The areal density of drives continues to increase at a rate of about 100% per year and contemporary state-of-the-art disks have been developed with

densities over 100 Gbits/in^2 [3]. Advances in perpendicular recording are projected to push areal densities even higher by deterring the superparamagnetic limit to 1Tb/in^2, and research into novel recording schemes could push densities even higher [4, 5]. While the charge and spin properties of the electron have separately spawned two of the most rapidly improving technologies of our time, little has been done to combine the two to function simultaneously in the same material, an idea that may lead to further enhancements in information technology beyond the limits of miniaturization.

1.2 What is Spintronics?

The nascent field of spin electronics (or spintronics) stands to assimilate these two fundamental properties of the electron—charge and spin—to form the basis for a new class of device design [6–10]. Operating by the manipulation, transport, and detection of charge carrier spins, spintronics is expected to improve upon traditional electronic and photonic devices, allowing for enhancements in the form of reduced power consumption, faster device operation, and new forms of information computation. Spintronics may lead to devices such as spin-polarized LEDs, spin-FETs, and spin-based qubits for quantum computers. Increased functionalities are also expected, such as integrated magnetic/electronic operations on the same chip.

Currently, very few spintronic devices have appeared on the market but have already made an astounding impact on technology. For example, metallic-multilayered structures displaying large amounts of magnetoresistance (so-called Giant Magnetoresistance) have replaced conventional hard-disk read heads, leading to huge increases in hard-disk storage [6]. These devices consist of a sandwich structure where layers of ferromagnetic and non-ferromagnetic material are alternately stacked. The resistance through the device depends on the relative magnetic orientation of the ferromagnetic layers. When the layers are magnetically aligned so that their directions of magnetization point opposite to one another (180 degrees misalignment), the resistance through the device is large. Conversely, when the magnetic layers are aligned parallel, the resistance is reduced. These sensors

have become the prominent form of solid-state magnetic sensing technology. As the size of magnetized bits shrink and areal densities continue to increase, sensors must become even more sensitive to the small changes in magnetization. The advent of GMR technology has become a multi-billion dollar industry and revolutionized the read heads used in hard disk technology.

1.3 Dilute Magnetic Semiconductors

Of particular interest is the creation and control of spin-polarized currents in semiconducting material. Ferromagnetic semiconductors provide easier integration of spintronics into existing semiconductor devices. For instance, highly efficient spin injection is possible between semiconductor/semiconductor interfaces, whereas only spin polarizations of a few percent are possible between a ferromagnetic metal/semiconductor interface due to the conductivity mismatch [11]. Ferromagnetic semiconductors allow the 'tools' of conventional semiconductor technology to be utilized. These tools include p-n junctions and heterostructures, which provide a convenient platform for a wide variety of devices that allow for electronic gain and light emission. However, in order to fully realize semiconductor-based spintronics, significant challenges related to the lifetime, control, and detection of spin polarized carriers in semiconductors must be addressed. Materials that can retain their ferromagnetism comfortably above room temperature are crucial to the practical application of spintronic devices.

These reasons have created interest in developing a class of materials known as dilute magnetic semiconductors (DMS). DMSs are semiconductors doped with a few percent of magnetic atoms. The magnetic atoms occupy lattice sites and induce ferromagnetism in the otherwise non-magnetic semiconductor host. DMSs typically have ordering temperatures much lower than room temperature. There has been some success in attaining room temperature ferromagnetism in various semiconductors, but the results are non-reproducible among research groups and contradictory to some theoretical predictions. Thus there is a great research opportunity for the study of ferromagnetism

in semiconductors for both real-world applications and for the added knowledge to fundamental physics.

CHAPTER 2
REVIEW OF DILUTE MAGNETIC SEMICONDUCTORS

The idea of magnetism in semiconductors is not new. The question of whether charge and spin can coexist in the same material to enhance material properties has been addressed for many years. While magnetism in metallic and insulating materials was well known, the possibility of magnetic ordering in semiconductors was not discovered until the mid 1900s. From rather difficult beginnings, the field of magnetic semiconductors has seen significant progress, especially in the advancement of magnetically doped semiconductors. Significant challenges still remain related to the preparation and growth of materials, understanding the physical origins of ferromagnetism in semiconductors, and raising the magnetic ordering temperatures, just to name a few. This section will first provide a glimpse into the history of experimental progress surrounding magnetic semiconductors. Next, a review of the leading theories that delve into the physical origins of magnetic coupling in DMS is given. Lastly, a brief review of the recent progress in magnetically doped ZnO is presented.

2.1 Magnetic Semiconducting Materials: A Short History

The story of magnetic semiconductors originates from humble beginnings. In the 1960s and 1970s, semiconducting behavior in ferromagnetic material was uncovered with the discovery of the europium chalcogenides (EuO) and chromium spinels ($CdCr_2S_4$, $CdCr_2Se_4$). These materials are true ferromagnetic semiconductors in the sense that they have magnetic atoms "built-into" the crystal sublattice. The elegant interplay between band electrons and localized magnetic ions in these materials brought about extensive research and scientific interest into the field. However, these materials have not progressed beyond the field of academic research for several reasons [12, 13]. First of all, their crystal structures are incompatible with conventional semiconductors, like Si and GaAs, making their integration with contemporary electronics difficult. The synthesis of these materials is also cumbersome and hard to reproduce, making industrial production of the crystals

expensive. And lastly, low ferromagnetic ordering temperatures (Tc $<$ 100K) make them less attractive for practical applications.

Moving in a slightly different direction, other work has focused on making non-magnetic semiconductors magnetic by doping them with small amounts (typically a few percent) of magnetic atoms. This class of materials has attracted renewed interest in the development of magnetic semiconductors. Such compounds are known as diluted magnetic semiconductors, or DMS, because of the dilute concentrations of magnetic impurities. Notice, these materials are fundamentally different than the Eu chalcogenides and Cr spinels since the magnetic atoms are artificially added into the lattice; the magnetic atoms are not a part of the periodic crystal structure of the parent material.

Early studies of DMS materials began with Mn-doped II-VI alloys of the form $A^{II}_{1-x}Mn_xB^{VI}$ (where A^{II} = Zn, Cd, Hg and B^{VI} = S, Se, Te). These materials were heavily studied in the 1980s and comprehensively reviewed by Furdyna [14]. It is worthwhile to review some aspects of these materials since ZnO also belongs to the II-VI family of semiconductors. The ternary nature of these compounds makes them amenable to tuning the lattice and band parameters by varying alloy composition, making them an attractive candidate for the preparation of heterostructure devices. The alloys crystallize into either the zinc-blende or wurtzite structure and are formed by sp^3 tetrahedral bonding, incorporating the valence s-electrons from the group II metal and the p-electrons from the group VI element. Elemental Mn has a half-filled 3d-shell and two valence ($4s^2$) electrons. Manganese atoms may substitute on the group II sites as Mn^{+2} by giving up these two valence electrons. High solubilities of Mn in the host materials while maintaining the zinc-blende or wurtzite structures are possible, which is thought to arise from the chemical similarity of Mn^{+2} to the group II element. The 3d-shell of Mn is exactly half-filled and requires substantial energy to add an electron; this makes the $3d^5$ orbit act chemically similar to a $3d^{10}$ orbit. The magnetic properties of these alloys are dictated by the exchange interactions between local atomic moments (provided by the

Mn) and the sp-band electrons, and have dramatic effects on the optical and electrical properties of the material, such as giant Faraday rotation and bound magnetic polaron formation. Driven mostly by superexchange mechanisms—an indirect exchange interaction mediated through the anion—these systems exhibit high temperature paramagnetism, low temperature spin-glass phase, and type III antiferromagnetic ordering [14]. Neutron diffraction studies show that the antiferromagnetic ordering of these structures is limited to short ranges, implying that the magnetic ordering is confined to the formation of small cluster regions [14]. Recently, however, ferromagnetic ordering has been achieved in low-dimensional quantum wells driven by hole-mediated exchange, but with low Curie temperature (Tc $<$ 2K) [15]. An additional obstacle to the practical applicability of II-VI material is the capability of doping the material both n-type and p-type (bipolar doping). Again, these materials are not practical since the materials that did show ferromagnetism were restricted to low ordering temperatures (Tc just a few degrees above 0K).

In the early 90s, a technological breakthrough in the advancement of DMS occurred with the discovery of ferromagnetism up to $\sim$35K in Mn-doped InAs [16–18]. InAs is an established III-V compound semiconductor material. Transition metal species are known to have very low solubility in host III-V materials, but the problem was overcome by non-equilibrium epitaxial growth using low temperature molecular beam epitaxy (LTMBE). III-V materials find widespread application in the electronics and optoelectronics industries as high-speed digital devices, visible and infra-red light-emitting diodes and lasers, and magnetic sensors. The demonstration of ferromagnetism in InMnAs offered the intriguing opportunity to study spin-based phenomena in these well established semiconductor devices.

Eventually, the success of LTMBE growth of InMnAs led to the development Mn-doped GaAs DMS. Segregation of Mn secondary phases, namely the MnAs phase, was suppressed using low temperature growth (Tg=250°C). If, however, the temperature was raised or the Mn flux was too high, phase segregation could occur. Mn acts as an acceptor

dopant when substituted on the group III sites leading to high hole concentrations which, as explained later, is a necessity for ferromagnetism in the material. The coupling of the charge and spin-based processes have been repeatedly proven in GaMnAs, including the realization of spin-polarized light emission [19] and electrical and optical control over the ferromagnetism [20]. Unfortunately, despite efforts to raise it, GaMnAs is limited by its low Curie temperature of 170K (well below room temperature). Raising the Curie temperature has been the biggest challenge for GaMnAs based DMS.

2.2 DMS Theory: The Physical Origins of Ferromagnetism in DMS

Understanding the physical mechanism behind magnetic ordering in DMS materials is an essential ingredient to their further development. Indeed, if both a conceptual and quantitative foundation to the origin of ferromagnetism in these materials is developed, they may provide the direction necessary to a successful recipe for the fabrication of higher Tc materials. At the present time, however, there is an incomplete understanding of the origin of ferromagnetism in DMS material and the subject remains an issue of active debate. This section will discuss the contemporary theories on the subject and the path they provide for subsequent research.

2.2.1 Dietl's Mean-field Theory

The motivation for studying ZnO for spintronics began with the work of Dietl et al. [21]. Dietl and coworkers employed a mean-field model of ferromagnetism, as originally described by Zener, to the case of III-V and II-IV compound semiconductors. Zener's model proposed that ferromagnetism is driven by the exchange interaction between carriers and localized moments. Zener's early model was abandoned because it was found inappropriate to describe the magnetism of transition metals. However, Dietl found that it could be used to accurately predict the ferromagnetic Curie temperatures of GaMnAs and ZnMnTe.

The model assumes that the ferromagnetic exchange interactions occur between localized spins doped into the semiconductor matrix and are mediated by charge carriers.

These spins are assumed to be randomly distributed throughout the host semiconductor lattice. Specifically, the doped Mn ions reside on group II or III sites and provide the localized spins. Conceptually, the affect may be envisaged as a feedback between the magnetic spins and the carriers by a spin-spin process; the localized magnetic spin induces carrier polarization which then induces magnetic polarization and so on (Figure 2-1) [22, 23]. The model suggests that high values of Tc are obtainable in p-type material, while the Tc of n-type material should be constrained to lower temperatures. This can be attributed to both the large p-d exchange integral ($N_o\beta$) and density of states of the valence band, while the conduction band's s-d exchange ($N_o\alpha$) and density of states are significantly smaller [24]. Note that in the case of III-V semiconductors, Mn also acts as an acceptor dopant whereas it substitutes isovalently in the II-VI semiconductors. Dietl extended his calculation to predict the Curie temperatures of other semiconductor systems and oxides. The predictions were based on a Mn concentration of 5% and a hole concentration of $3.5\text{x}10^{20}\text{cm}^{-3}$. The results are summarized in figure 2-2 as a function of bandgap. Of particular importance, are the predicted Curie temperatures in excess of room temperature for GaN and ZnO.

Diet's theory has proven useful in understanding the experimental results for GaMnAs. However, it does not appear to be consistent with the experimental results of transition metal doped wide band-gap semiconductors, such as the predictions for GaN and ZnO. This stems from several reasons, including the difficulty in experimentally preparing p-type ZnO material and the many observations of ferromagnetism in n-type ZnO DMS. Nevertheless, Dietl's original theory has led to multiple experimental and computational studies of transition metal doping in ZnO.

2.2.2 First-principles Design: DFT Calculations

Sato and Katayama-Yoshida have employed first-principles design to investigate ferromagnetism in both semiconductor and oxide spintronics [25–27]. The magnetic stability of transition metal doped ZnO was calculated using density functional theory

(DFT) within the framework of the local density approximation (LDA). The random distribution of transitional metal ions over the lattice (creating disorder in the alloy) was inherently included in the calculations by the coherent potential approximation (CPA). Magnetic stability was calculated by comparing the total energy difference between the ferromagnetic and spin-glass state, the lower of the two representing the ground state of the system. In the case of Mn, their results are consistent with Dietl's theory that the ferromagnetic state is stabilized with the addition of hole doping, and without holes the spin-glass state is favored. However, V, Cr, Fe, Co, and Ni impurities were predicted to be ferromagnetic without the need of additional charge carriers. Electron doping further stabilized the ferromagnetic state in these alloys. Their work also points to a contribution of d-states at the Fermi level, hinting at some delocalization of d-states. It was suggested that this could lead to ferromagnetic ordering through a double-exchange interaction, in which ferromagnetic alignment is stabilized by the hopping of 3d electrons between neighboring TM sites. This mechanism is driven by partially unoccupied up-spin (or down-spin) states in the 3d-band and is therefore not possible in the case of Mn, which exhibits a half-filled 3d band. In the case of p-type doping, however, the transference of weakly-bound 3d electrons between Mn ions may be mediated by the presence of holes. The valence band p-states hybridize with the 3d-states of Mn and itinerant holes can retain their d-like character. This stabilizes the ferromagnetic phase for Mn doping.

2.2.3 Ferromagnetism in Disordered Alloys

An additional theoretical approach considers whether ferromagnetic ordering between the localized spins can originate from localized carriers. Again, the model is developed in the mean-field treatment but accounts for positional disorder in the alloy. Numerical studies within the mean-field treatment show that the nature of ferromagnetism is strongly affected by this disorder and that the Tc can be pushed to higher temperatures with increasing randomness in the position of Mn ions [28].

Ferromagnetism in this localized carrier regime can be explained through the formation of bound magnetic polarons (BMPs) [29, 30]. A BMP is a quasi-particle comprised of the localized carrier and the magnetic atoms encompassed within its radius (Figure 2-3). The localized carrier is bound to its associated defect (such as a donor atom if the carrier is an electron) in a hydrogenic orbital of radius, $r_h = \epsilon(m/m^*)a_o$, where ϵ is the high frequency dielectric constant, m^* is the effective mass, and a_o is the Bohr radius (53pm) [31]. This radius can be large (~8Åin ZnO) extending over several lattice constants, and can encompass a number of magnetic dopants depending on their concentration. The exchange interaction between the bound carrier and the magnetic moments tends to align the moments parallel to one another inside the BMP. At high temperatures, the BMPs may be isolated from one another. However, as the temperature is lowered, the BMP radius grows and the individual BMPs begin to overlap. Overlapping BMPs become correlated and their spins align, producing long range ferromagnetic interactions [29]. At a critical temperature, the overlapping BMPs are percolated throughout the sample and the transition to ferromagnetism occurs. The BMP model is equally applicable to n-type or p-type material [30].

The BMP model allows for ferromagnetism in an insulating or semi-insulating regime. This is especially attractive in the case of ZnO where high p-type doping, as required by Dietl's model, is inherently difficult.

2.2.4 Ferromagnetism in a Spin-split Conduction Band

Coey et al. have proposed another model for ferromagnetism in DMS materials based on a spin-split donor impurity band [31]. The model is consistent with the observed magnetization for n-type transition-metal doped ZnO. In this model, donor defects (which could arise from either oxygen vacancies or zinc interstitials in the case of ZnO) overlap at large concentrations to form an impurity band. The impurity band can interact with local magnetic moments through the formation of bound magnetic polarons (BMP). Within each BMP, the bound carrier interacts with the magnetic dopants inside its radius and

can align the spins of the magnetic dopants parallel to one another. Ferromagnetism is achieved when the BMPs start to overlap to form a continuous chain throughout the material, thus percolating ferromagnetism in the DMS. However, Coey showed that in this model, to achieve a high Tc, a fraction of the polaronic charge must delocalize (or hybridize) onto each magnetic dopant. In a band scheme, this occurs when the impurity band overlaps with unoccupied d-levels of the magnetic dopant. It was shown that for Sc, Ti, and V, the spin-up states of the 3d TM metal are aligned with the impurity levels, resulting is significant alignment. Similarly for Fe, Co, and Ni doping, the spin-down states perform the same function. Interestingly, Mn and Cr doping would not lead to strong magnetization due to small hybridization.

Within the framework of Coey's model, Kittilstved et al. have performed detailed spectroscopic experiments on cobalt-doped ZnO [32]. Their results show that the singly ionized Co^{+} state lies close to the conduction band, similar in energy to a shallow donor state. Since the energies are similar, charge transfer can occur between the cobalt atoms and the donor impurities, thus leading to the hybridization necessary for ferromagnetism. Kittilstved et al. has also shown that this leads to an inherent polarity difference for ferromagnetism in cobalt and manganese-doped ZnO. Whereas ferromagnetism in cobalt-doped ZnO is closely tied to the presence of shallow donors, manganese-doped ZnO is closely tied to the presence of shallow acceptors. The difference lies in the location of the singly ionized Mn^{+3} state, which sits close to the valence band in ZnO. This idea is described further at the end of the next section.

2.3 Experimental Progress in ZnO DMS

On the experimental front, there has been a wide distribution in the magnetic properties reported for transition metal doped ZnO. Experiments have now covered a broad range of parameters, including various transition-metal dopants (every element in the first row of the transition metal series has now been surveyed), compositional variations, preparation techniques and growth conditions, and post-growth processing.

The observed results are often conflicting and non-reproducible between research groups. The discrepancy in the observed properties (and their interpretation) likely stems from different growth techniques and conditions, and insufficient characterization. Most of the difficulties arise in determining if the material is a true DMS (TM atoms randomly substituting Zn lattice sites) or if ferromagnetism originates from TM clustering or dopant-induced secondary phases. In any case, the results indicate that the underlying mechanisms of ferromagnetism in ZnO DMS are quite sensitive to growth conditions and must be clearly delineated by careful analysis.

Describing all the experimental trials in ZnO DMS over the past several years would be tedious and overwhelming. There are already several reviews covering the subject [33–36]. A compilation of some results is listed in Table 2-1 [36]. Instead, to provide a flavor of the experimental progress, a brief summary of the important achievements surrounding transition-metal doped ZnO is provided.

2.3.1 Mn-doped ZnO

By far, the two most studied magnetic dopants in ZnO have been Mn and Co. Fukumura and coworkers were the first to study Mn-doped ZnO DMS using PLD [37]. A large solubility of 35% Mn was achieved while retaining the wurtzite structure of ZnO (reminiscent of the earlier studies on II-Mn-VI compounds discussed earlier). This is over the thermodynamic solid-solubility limit of Mn in ZnO and is a testament to the non-equilibrium conditions obtainable by thin film growth. They later showed the heavily doped alloy to exhibit spin-glass behavior with a spin-freezing temperature of $\sim$13K due to strong antiferromagnetic exchange coupling between neighboring Mn atoms [38]. The high solubility of Mn achieved in ZnO motivated other experimental efforts into the synthesis of ZnMnO. While some groups reported ferromagnetism, others observed antiferromagnetic, spin-glass, or paramagnetic behavior (for example, refer to reference [36]).

Sharma and coworkers were the first to report ferromagnetism above room temperature in dilute Mn-doped ZnO bulk and thin film samples [39]. Bulk pellets with a nominal concentration of 2 at% Mn (EDS showed the actual concentration to be much lower: ∼0.3 at%) sintered below 700°C were found the have a Curie temperature of 420K. Additionally, thin films deposited by PLD with 2.2 at% Mn were shown to exhibit ferromagnetism at room temperature. However, using similar preparation techniques to Sharma et al., Kundaliya and coworkers [40] convincingly demonstrated that the observed high-temperature ferromagnetism resulted from a metastable phase (oxygen-vacancy-stabilized $Mn_{2-x}Zn_xO_{3-\delta}$), and not from the proposed carrier-mediated ferromagnetism between Mn atoms. There is also discrepancy in the reported overall distribution of Mn atoms. For example, a homogenous distribution of Mn was observed by Cheng and Chien [41], while Jin et al. [42] found clustering of Mn atoms. Clearly, thorough characterization is needed to fully appreciate and understand the origin of ferromagnetism in these materials.

2.3.2 Co-doped ZnO

One of the early works on cobalt-doped ZnO DMS was by Ueda et al. [43]. They found the material to be ferromagnetic above 280K with 5-25%Co and 1%Al (added as an n-type dopant) without the addition of secondary phases. Differences in the magnetization were attributed to differences in the conductivity; films with higher carrier concentrations ($\sim 10^{20} cm^{-3}$) showed ferromagnetic features with higher Ms and Tc. Since then, additional experimental studies have investigated the properties and origin of ferromagnetism in cobalt-doped ZnO. Again, the results are conflicting with reports of ferromagnetism in phase pure films [44, 45], ferromagnetism from clusters [46], and no observed ferromagnetism [47].

The first report of reversible (controlled) switching of ferromagnetism in any DMS was demonstrated by Schwartz and Gamelin in cobalt-doped ZnO [48]. The reversibility was mediated by the incorporation and removal of Zn interstitials. The Zn interstitial (Zn_i) is a known n-type dopant that produces a shallow donor level below

the conduction band. Diffusing Zn_i into the lattice lowers the conductivity and activates room temperature ferromagnetism. Removing Zn_i, by heating in air, returned the films to an insulating state and subsequently quenched the ferromagnetism. The process was reversible over many cycles. This reversibility is evidence that free carriers activate ferromagnetism in cobalt-doped ZnO. The process was observed in both MOCVD grown films and ZnO:Co nanoparticle films prepared by spin coating. Strong hybridization of Zn_i donor states with Co^{+2} states near the conduction band (which, as explained earlier, is theoretically believed to cause ferromagnetism) was used to explain the magnetic ordering. Conduction electrons, derived from the Zn_i donors, delocalize over several Co^{+2} ions and ferromagnetically align their spins through a double exchange interaction.

Importantly, from the same group, Kittilstved was able to demonstrate a chemical polarity difference between the ferromagnetism in ZnCoO and ZnMnO [49]. Specifically, p-type ZnMnO led to ferromagnetism, while ferromagnetism in ZnCoO was activated by n-type doping. Doping of the ZnMnO was done on a local level by N-capping ZnMnO nanoparticles with amines. ZnCoO nanoparticle films were made n-type by capping with oxygen. Reversing the capping layers, ZnCoO:N and ZnMnO:O, led to the disappearance of ferromagnetism in both sets of films. Optical absorption, MCD, and photoconductivity measurements were employed to understand this inherent polarity difference [32]. For n-type ZnCoO, the authors showed that a resonance in the charge transfer ($Co^{+1} \rightarrow Co^{+2} + e^{-}_{CB}$, $\Delta E \approx 0.27eV$) and donor state energies can lead to a large hybridization necessary for ferromagnetism. For ZnMnO, a similar resonance was observed but derived from the Mn^{+3} state close to the valence band ($Mn^{+3} \rightarrow Mn^{+2} + h^{+}_{VB}$, $\Delta E \approx 0.22eV$) with acceptor state energies.

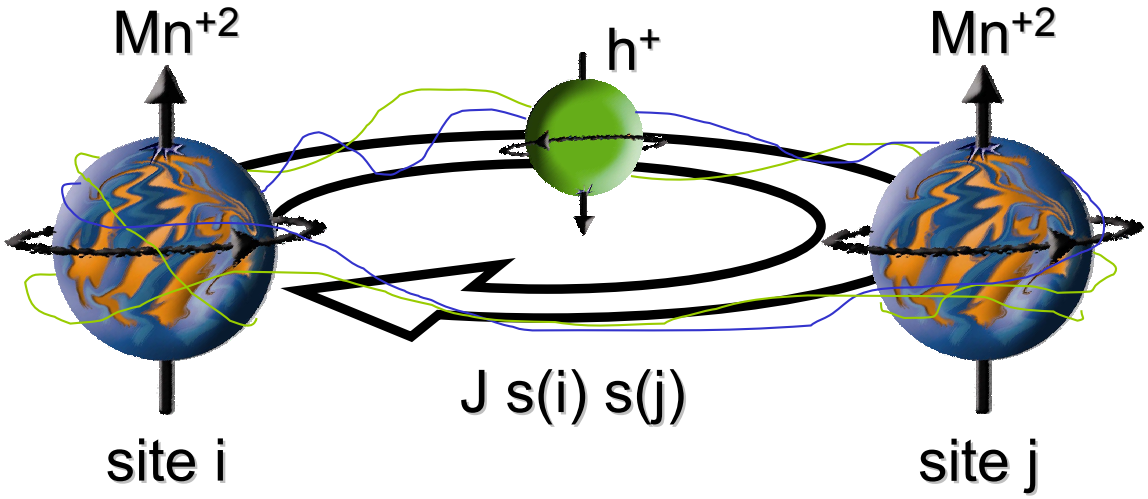

Figure 2-1. Schematic representation of magnetic exchange between two Mn ions mediated by a delocalized hole. Adapted from [22].

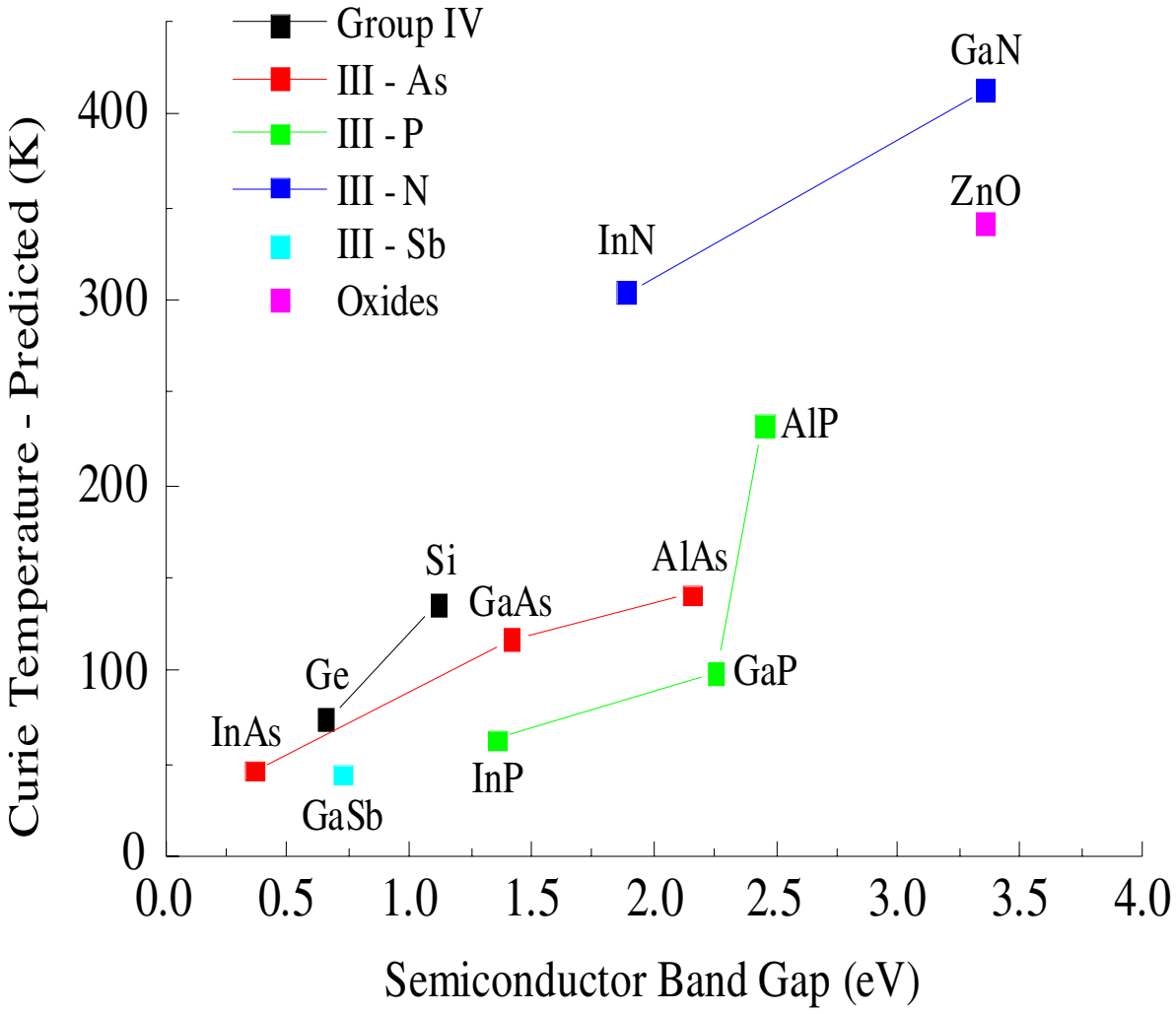

Figure 2-2. Predicted Curie temperatures based on Dietl's calculations [21] for 3%Mn and a hole concentration of 3.5x10^{20}cm^{-3} (After [50]).

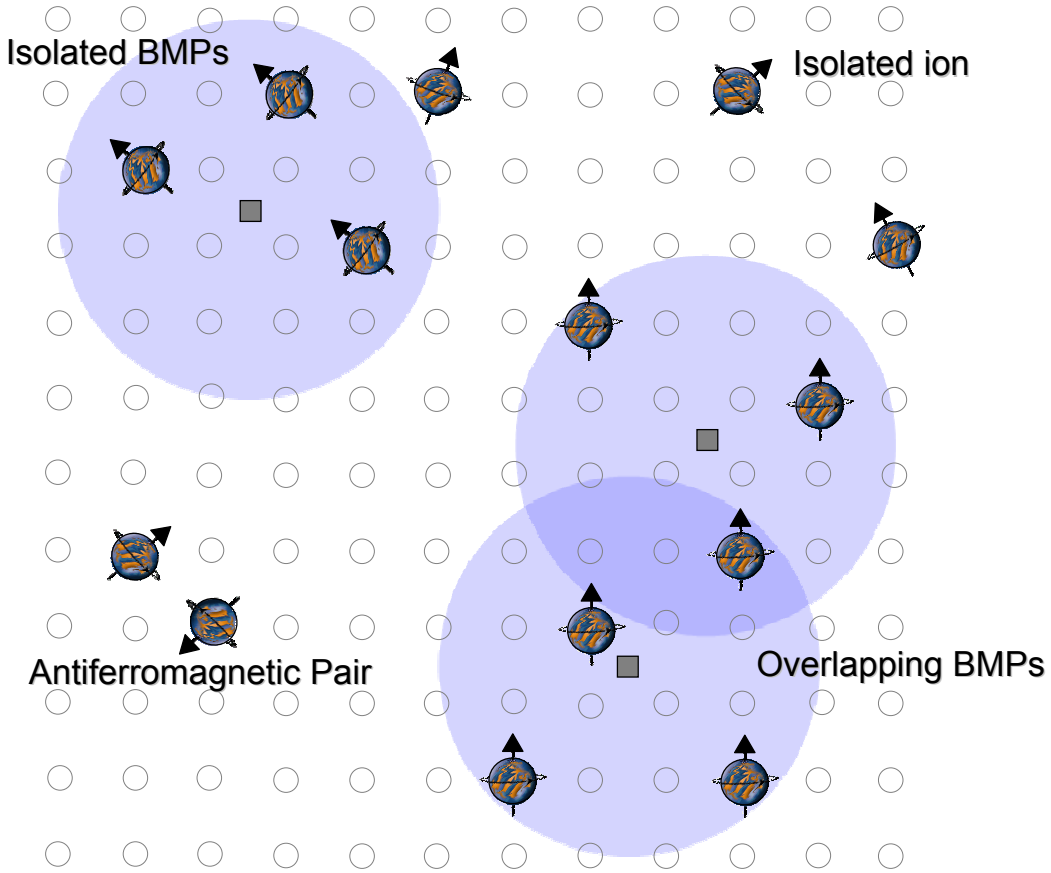

Figure 2-3. Illustration of bound magnetic polarons. An electron bound within its hydrogenic orbital couples to magnetic impurities causing them to align parallel to one another inside the orbit radius (Adapted from [31]).

Table 2-1: List of ZnO-based DMS experimental results (After [36])

Compound	TM content	Substrate	Fabrication method	Growth temp(°C)	O_2 pressure (Torr)	Post-annealing	Tc (K)	Notes	Refs
ZnO:Mn	<0.35	c-sapphire	PLD	600	$5x10^{-5}$		N/A		[37]
ZnO:Mn	0.36	c-sapphire	PLD	600	$5x10^{-5}$		N/A	Spin-glass	[38]
$Zn_{1-x}TM_xO$		c-sapphire	PLD	500-600	10^{-9} to 10^{-6}		N/A		[47]
ZnO:Co	0.02-0.5	c-sapphire	PLD	300-700	10^{-6} to 10^{-1}			Spin-glass	[51]
ZnO:Mn	.01-0.36	c-sapphire	PLD	610	$5x10^{-5}$			Paramagnetic	[41]
ZnO:Mn	0.07	a-sapphire	sputtering	400	0.06			Paramagnetic	[41]
ZnO:Mn	0.03-0.2	GaAs(100)	sputtering	500-600	8x10-4				[52]
ZnO: (Co, Mn, Cr, or Ni)	0.05-0.25	r-sapphire	PLD	350-600	$2\text{-}4x10^{-5}$		280-300	$2\mu_B$/Co	[43]
ZnO:Ni	0.01-0.25	c-sapphire	PLD	300-700	$1x10^{-5}$			Superpara- or ferromagnetic	[53]
ZnO:V	0.05-0.15	r-sapphire	PLD	300	10^{-5} to 10^{-3}		>350	$0.5\mu_B$/V	[54]
ZnO:(Co, Fe)	<0.15	SiO_2/Si	Magnetron sputtering	600	$2x10^{-3}$	600°C, 10min, $1.0x10^{-5}$ Torr	>300	12-15 emu/cm^3	[55]
ZnO:Co	0.03-0.05	Bulk ZnO	Ion implantation			700°C, 5min, under O_2	>300	Oriented Co precipitates	[56]
ZnO:Co	0-0.25	c-sapphire	Sol—gel	<350		700C, 1 min	>350	$0.56\mu_B$/Co	[57]
ZnO:Mn	0-0.3	c-sapphire	PLD				>30-45	$0.15\text{-}0.17\mu_B$/Mn	[58]
ZnO:Mn	<0.04		Sintered pellets	500-700	Air, atm. pressure		>425	0.006emu/gm single phase	[39]
ZnO:Mn	0.02	Fused quartz	PLD	400			>425	0.05 emu/gm, single phase	[39, 59]
ZnO:(Fe, Cu)	0-0.1		Solid-state reaction	897			550	$0.75\mu_B$/Fe	[60]
ZnO:Co	0.015		PLD	650	$5x10^{-5}$		>300	Ferromagnetic	[61]
ZnO:(Co,Al)	0.04-0.12	Glass	RF sputtering		$1x10^{-2}$ in Ar		>350	$0.21\mu_B$/Co	[62]
ZnO:(Mn,Sn)	0-0.3		Implantation			700°C, 5min	250	Ferromagnetic	[63]
ZnO:Mn, Sn	Mn=0.03, Sn<0.1%	c-sapphire	PLD	400-600	0.02		>300	Ferromagnetic	[64]
ZnO:Mn and Co	0.05-0.15		Crystalline precursor					Antiferromagnetic	[65]
ZnO:Mn and Co	<0.05	Bulk	Melt growth	1000				Paramagnetic	[66]
ZnO:Co	0.1	O-face ZnO	PLD					Antiferromagnetic	[67]
ZnO:Co	<0.35	r-sapphire	MOCVD	350-600	40	500°C, 20 min in vacuum	>350	Ferromagnetic	[67]
ZnO:Co and Fe	<0.15	SiO_2/Si	Magnetron sputtering	600	$2x10^{-3}$	600°, 10 min 10^{-5} Torr	>300	Ferromagnetic 12-15emu/cm^3	[68]
ZnO:Mn	0.1	r-sapphire	PLD	650	0.1		>300	0.075 μ_B/Mn	[69]
ZnO:Mn and Cu	0.05-0.1	r-sapphire	PLD	650	0.1		400	0.1 μ_B/Mn	[69, 70]
ZnO:Sc,Ti,V, Fe,Co or Ni	0.05	r-sapphire	PLD	600	0.1-750		>300	0.5 μ_B/Ti,5.9 μ_B/Co $0.3\mu_B$/Sc	[60]
ZnO:Mn	0.02	Bulk pellets	Powder, pellets and laser-ablated films	500			>300	0.16 μ_B/Mn	[39, 59]
ZnO:Cr		STO	PLD				>400	Ferromagnetic	[71]
ZnO:Mn	0.08	Tetrapods	Evaporation	600			43	(Zn,Mn)Mn_20_4phases	[72]
ZnO:Mn	0.05	ZnO sub	PLD	200-600			250	High Tc lower TG	[73]
ZnO:Mn	0.02	Poly pellets pellets and thin films	Powder and PLD	400-800	0.4		>300	0.18 μ_B/Mn	[40]
ZnO:Mn	0.02-0.1	Pellets	Powder	400		500-800°C	>300	Interfacial phase	[74]

CHAPTER 3
THIN FILM DEPOSITION AND EXPERIMENTATION

Pulsed Laser Deposition (PLD) was used for all the film deposition presented in this dissertation. This section will cover the experimental apparatus and methods for these film depositions. A brief discussion of the basic PLD process will be given first. This is followed by a description of the specific PLD system used for deposition, including the growth chamber and UV excimer laser. Then the exact experimental steps used to deposit films in this work will be described, including the preparation of oxide targets (the source materials) and the typical growth procedure for obtaining epitaxial thin films.

3.1 PLD as a Tool for Thin Film Oxides

PLD has evolved into a successful and widely-used research tool for the fabrication of thin-film complex oxides [75, 76]. PLD is a physical deposition method. High-intensity laser pulses (upwards of 100s MW cm^{-2}) are used to vaporize atomic species from a target of desired chemical composition. The target material is typically a solid source, but liquid sources, such as organic liquids, are also feasible [77]. The laser energy is absorbed by the target and a rapidly expanding plume, containing electrons and ground- and excited-state neutral atoms and ions, is ejected from the target surface [76]. This plume is highly directional. It is emitted perpendicular to the target surface and has an angular distribution given by $f(\theta)=(\cos\theta)^n$, where $f(\theta)$ is the distribution of ablated flux and n$\sim$5-25 [76]. The ablated material is collected onto a heated substrate located several centimeters from the target.

PLD growth offers several advantages in the realm of thin film deposition [76]:

1. Congruent (stoichiometric) transfer of the target material to the deposited film. The various chemical components of complex oxides, or other multicomponent materials, are evaporated simultaneously. This allows the control of film composition by simply preparing targets of the desired composition. Typically, the compositional stoichiometry of the target is accurately reproduced in the film.

2. Almost anything can be ablated, including high melting temperature oxides.

3. The laser beam is capable of imparting considerable amounts of kinetic energy to the ablated chemical species. The additional kinetic energy can lead to larger sticking coefficients and enhanced adatom mobility on the growth surface, permitting epitaxy at reduced growth temperatures.

4. Deposition in a background gas is permissible. The highly energetic plume can readily undergo gas-phase reactions with ambient gases, such as O_2, H_2O, and NO_2, providing an addition degree of freedom in the growth parameters of thin film oxides.

3.2 PLD System Used for This Work

3.2.1 The Growth Environment

A commercial PLD system built by Neocera was used for the thin film depositions described in this dissertation. A diagram of the system is provided in Figure 3-1. The system is composed of one main vacuum chamber which is used for growth. This chamber is evacuated by a pair of pumps that are situated underneath the chamber and can be sealed-off by the gate valve. The laser used for target ablation is separate from the system. The other components of the system are contained within the growth chamber.

The Neocera system uses a Pfeiffer turbo pump to create and maintain the low pressures needed for growth. The turbo pump consists of a series of rapidly spinning blades to transfer gas out of the chamber. Essentially, gas molecules collide with the blades and are kinetically driven toward the pump exhaust. This is accomplished through multiple stages until the exhaust gas is compressed to the fore-line pressure of the backing pump. The turbo pump is water cooled by a recirculating chiller to suppress overheating. The system's turbo pump is backed by an oil-less four-chamber diaphragm pump. This backing pump serves two purposes. Before the turbo pump can be switched on, the backing pump rough pumps the growth chamber down from atmosphere to an inlet pressure manageable by the turbo pump. The growth chamber is evacuated to a pressure of at least 240 Torr before the turbo pump is switched on. The backing pump serves its second purpose by maintaining the fore-line pressure for the turbo pump to operate efficiently and removing the exhaust gas into the atmosphere. Since there is no load-lock,

the chamber has to be evacuated from atmosphere for every growth run. The ultimate base pressure of the system is 2 x 10^{-6} Torr.

The pressure inside the growth chamber is monitored by a pair of vacuum gauges. Pressures above 1mTorr are monitored with a Granville convectron gauge. Pressures below 1mTorr are monitored using a cold-cathode gauge.

The ablation targets are mounted onto a rotating carousel. A total of six targets can be mounted at one time and each target can be accessed during growth by rotating the carousel to the position of the desired target. This allows for the growth of film stacks that can be used for device fabrication, compositionally graded layers, superlattices, etc. The ablation target is also rotated around its center axis during deposition. Target rotation helps maintain uniform target ablation and film deposition.

The substrates are mounted onto a solid block, resistive heater. The heater is mounted to a vacuum flange that can be removed to mount the samples and provide access to the growth chamber to exchange targets.

Laser access into the growth chamber is granted through an optical window made from SUPRASIL fused silica, which has a large optical transparency to UV radiation in order to minimize attenuation of the laser energy.

3.2.2 The Laser Source

A Lambda-Physik Compex 205 KrF pulsed laser is used as the ablation source. This laser produces a coherent beam with a 248nm wavelength. The laser energy and pulse repetition can be varied to suit a particular experiment. Most of the growth in this dissertation was done at energies around 300mJ with repetition rates ranging from 1 to 10 Hz. The laser output is directed into the PLD chamber by a series of four mirrors. One of the mirrors is mounted to a microprocessor driven rotational stage. This stage can be programmed to repeatedly scan the laser across the surface of the ablation target. There is an approximate 10% loss of beam energy at each mirror. The beam is focused using two plane focusing lenses to focus both the horizontal and vertical width of the

beam. Typically, the beam was focused to a spot size of 4-6 mm^2. The Compex 205 is a chemical excimer laser that emits ultra violet (UV) light at a wavelength of 248nm. The term 'excimer' is derived from EXCIted diMER. The Compex uses a KrF excimer, derived from ultra-high purity Kr and F_2 gases, as the source of light emission. The excimer is formed by supplying electrical energy to the gas mix. Since Kr is a noble gas, the bonded KrF complex is a highly unstable excited state and quickly decomposes to the unbonded ground state. The stored chemical energy is released in the form of a photon with the characteristic decomposition energy (the lasing energy):

$$2KrF(g) = 2Kr(g) + F_2(g) + energy(248nm)$$

3.3 Typical Growth Procedure

A typical growth run using the PLD system is described next. Describing the deposition process in detail can alleviate ambiguity at each step and provide a means of tracking down differences in film preparation between users. The process is described in two steps, substrate preparation and film growth.

3.3.1 Substrate Preparation

The sapphire substrates used for ZnO film growth typically came in the form of 2" diameter wafers. Square substrates 6.5mm x 6.5mm were cleaved from the larger wafers using a diamond scribe. The $MgAl_2O_4$ and MgO substrates used for the Cu_2O films came pre-cut in 1cm x 1cm squares and were cut into four 5mm x 5mm squares for film growth.

Before each deposition the substrates were chemically degreased in sequential baths of TCE, acetone, and methanol. The degreasing method was the same for all substrates. First, about 15mL of each solvent was poured into separate 50mL beakers. The bottoms of the beakers were then placed into an ultrasonic bath of tap water to aid the solvent in removing any contamination or residue inside the beaker. The beakers were ultrasonicated for at least 5 minutes. Next, each beaker was dumped out and refilled with about 20mL of fresh solvent. The substrates were first placed into the beaker of TCE and ultrasonically rinsed for at least 5 minutes. To keep the substrates off the bottom of the beaker, the

substrates were held with plastic tweezers (which were pinched closed using a binder clip). The substrates were then subsequently cleaned in the acetone beaker and then the methanol beaker. In order to keep the substrates clean of dried solvent residue, they were immediately blown dry with N2 after being removed from the methanol.

After cleaning the substrates they were mounted to the heater block. The heater block was cleaned before attaching the substrates. The block was scraped clean of dry silver paint (left from the previous deposition) using a stainless steel razor blade, etched in 1:1 Nitric acid/Di H_2O, and wiped with acetone. The substrates were attached to the block with silver paint (Ted Pella 'Leitsilber 200' silver paint) and allowed to dry for 20min inside a fume hood. A glass petri dish was placed upside-down over the substrates to protect them from dust during the drying time.

3.3.2 Thin Film Growth

After drying, the samples and heater assembly are mounted inside the chamber by reattaching the heater flange to the system. The gate valve is opened and the backing pump is switched on to rough pump the growth chamber from atmosphere. When the pressure drops below 250 Torr, the turbo pump is then turned on. The system is allowed to pump for a few hours until a pressure below 1 x 10^{-5} Torr is reached. The temperature controller is ramped to the desired substrate temperature at a rate of 10°C/min. Oxygen is flowed in to fill the chamber with 10mTorr of O_2. This is thought to help drive off any hydrocarbon contamination from the substrate during heating. When the set temperature is reached, the sample shutter is closed to block the substrates from the target, the oxygen flow is stopped, and the target is pre-ablated at 300mJ for at least 1000 laser pulses. Pre-ablation cleans the target surface before actual film growth. Since the chamber pressure rises from vaporized species off the chamber wall during heating, the chamber is left at temperature in 10mTorr O_2 until the base pressure drops below 1 x 10^{-5} Torr. To start the film deposition, the shutter is flipped open, oxygen is introduced into the chamber at the desired growth pressure, the laser energy and reprate are set and the laser

is switched on. During the growth, the laser beam is scanned and the target is rotated to provide uniform ablation across the target surface. Once the growth is completed, the temperature is ramped back to room temperature. The oxygen overpressure is usually maintained at the growth pressure during cool down. The samples are then removed from the system and stored in a desiccator until needed.

3.4 Fabricating PLD Ablation Targets

Ceramic targets of known composition were used as the source material for the PLD film growth. Films were deposited by ablating these targets inside the growth chamber. The ablation targets were fabricated using the solid-state reaction of mixed oxide powders. The high purity source powders (>99.99% pure) were purchased from Alfa-Aesar. Targets were prepared based on atomic percent concentrations of the dopant species (in contrast to weight percent). For example, a $Zn_{0.97}Mn_{0.03}O$ target contains 3at% Mn doped into the ZnO. Standard dimensional analysis using atomic weights from the periodic table were used to convert at% to weight percent so the appropriate amounts of powder could be weighed. The powders were weighed in a plastic weighing dish using an electronic scale. After weighing, the powders were transferred to an alumina mortar. Methanol was added to the powders to aid with mixing and the powders were ground and thoroughly mixed using an alumina pestle. The powders were then allowed to dry in air. A uniaxial press was used to compact the powders into a 1" diameter disc using a stainless steel die. The applied pressure was typically 2–4 metric tons. Each disc was placed on a thin piece of alumina and placed inside a high temperature box furnace. The pellets were then covered with an alumina crucible. The box furnace was raised to 1000°C at a rate of 10°C/min. The targets were sintered at 1000°C in air for 12 hours and allowed to cool to room temperature.

3.5 Thin Film Characterization

3.5.1 X-ray Diffraction

X-ray diffraction (XRD) is a versatile tool for studying the crystalline nature of materials. Analysis of grain size, film quality, and phase identification are possible through XRD techniques. I used powder XRD to investigate the structural information of the deposited films. Specifically, crystalline phases of material were determined by theta-2theta diffraction scans.

The films were measured with a Philips APD 3720 diffractometer. The system uses a Cu x-ray source that emits primarily Cu $K_{\alpha 1}$ photons with a wavelength of 1.5405 Å. A Ni filter absorbs most of the other characteristic wavelengths from the source, although some Cu $K_{\alpha 2}$ and K_{β} photons escape toward the sample. These wavelengths are important because they generate extra diffraction peaks in the collected data.

In XRD, the incident x-rays interact with the material through constructive and destructive interference from the periodic lattice planes of the crystal. The condition for constructive interference is governed by Bragg's Law:

$n\lambda = 2d \sin\theta$

where λ is the x-ray wavelength, d is the distance between atomic planes, and θ is the angle between these planes and the x-ray source (Figure 3-2). Therefore only specific d-spacings satisfy the Bragg condition at a certain angle.

The Philips system is configured in Bragg-Brentano geometry. The x-ray source is pointed at the sample and held in a fixed position. The sample rotates around the angle θ, and the detector rotates around 2θ. In this θ-2θ geometry, only planes parallel to the sample surface can satisfy the Bragg condition. This provides crystalline orientation information of the deposited film.

The x-ray intensity is plotted as a function of 2θ to reveal the diffraction pattern for a sample. Phase identification is possible by comparing the diffraction peaks to

known material standards in the JCPDS catalog. With this method, recognition of any dopant-induced secondary phases within the semiconductor host was determined.

Additional x-ray characterization for select samples was carried out on a Philips X'pert high-resolution diffractometer. ω-rocking curves were used to assess the lattice parameter and crystalline quality of the deposited films. The epitaxial quality between films was quantified by the ω-rocking curve FWHM (full-width at half maximum). Φ-scans were used to measure the in-plane orientation and film texture to confirm epitaxial registry with the substrate.

3.5.2 Magnetoresistance and Hall Effect Measurements

Transport measurements provide valuable insight into the electronic structure of materials. Electrical properties are sensitive to material imperfections, including electrical dopants, atomic impurities, lattice strain, and structural defects. The transport properties of films grown in this work were probed by magnetoresistance and Hall effect measurements.

Samples were measured using either Van der Pauw or Hall bridge geometries. Van der Pauw samples were approximately 6.5mm x 6.5 mm square. Hall bridge specimens were patterned during film growth by depositing through a stainless steel shadow mask. Contacts were soldered to the samples using indium metal. The films were mounted inside a Quantum Design Physical Property Measurement System (PPMS) to control the ambient temperature and magnetic field near the sample, and the electrical data was collected using a Keithley high-impedance Hall effect system. Details of the configuration are provided in the appendix.

The Hall effect provides valuable information about the charge carriers in a material. The Hall effect is caused by the interaction of moving charge carriers with an applied magnetic. This interaction is dictated by the Lorentz force and leads to an accumulation of charge at the sample edge. The accumulated charge distribution induces a potential drop (the Hall voltage) between the sample edges until the Lorentz force is balanced. The

carrier type, mobility, and density can be determined from measurements of the induced Hall voltage. Hall effect measurements become especially valuable in the study of magnetic materials. In a ferromagnetic material, the Hall resistivity is described by the empirical expression:

$\rho_{xy} = \mathrm{R}_s\mathrm{M} + \mathrm{R}_o\mathrm{B}$

R_o is termed the ordinary Hall coefficient and is caused by the Lorentz force. R_s is the anomalous Hall coefficient that results from a finite sample magnetization. While the ordinary term is caused by classical physics, the anomalous term derives from quantum mechanical effects. The anomalous term results from spin-dependent scattering between charge carriers and moment carrying centers. The physical origin of this interaction is the spin-orbit coupling of the charge carrier as it passes by a magnetic impurity. The strength of this term is given by the strength of the spin-orbit coupling and the relative density of spin-up and spin-down electrons.

Magnetoresistance can provide key insights into the transport properties of magnetic semiconductors, including the potential landscape of impurities, lattice disorder, and electron-electron interactions [78]. Magnetoresistance was typically measured simultaneously with the Hall data.

3.5.3 Electron Dispersive Spectroscopy (EDS)

EDS was used to determine chemical compositions. The EDS analysis was performed inside a JEOL 6335F field-emission scanning microscope fitted with a liquid nitrogen cooled EDS detector.

EDS measures the emitted x-ray spectrum of a material when bombarded by a beam of energetic electrons. The high energy electrons are focused onto a sample where they transfer their kinetic energy into the lattice through a series of collisional events. A small fraction of these events are capable of ionizing an atom by ejecting an inner shell electron. The atom then reverts back to its ground state by filling the vacancy with an electron from a higher energy orbital, and either a photon or Auger electron is emitted.

The emitted photons have a characteristic energy depending on the atom that emits it. Therefore, elemental information can be determined. The relative amount of each element can be calculated by comparing the peak heights and applying the corresponding ZAF corrections, where Z is the atomic number, A is absorption, and F is the x-ray fluorescence.

3.5.4 Optical Absorption

Information related to the electronic band structure of semiconductors can be inferred from their interaction with light. The absorption of an optical photon necessarily involves the transition of an electron from an occupied energy state to a vacant state of higher energy. Energy and momentum must be conserved in the process.

Consider a semiconductor with a filled valence band and empty states at the bottom of the conduction band. If the photon energy is below the lowest allowed electronic transition, in this case the band-gap energy, the photon is not absorbed and passes through the material; the material is transparent to the particular photon energy. If, however, the photon energy is greater than the gap energy, the photon is absorbed by an electronic transition from the valence to the conduction band. Therefore, the onset of optical absorption is $h\nu \geq$ Eg. The semiconductor acts as a low-pass optical filter.

The absorption coefficient, α, for direct interband transitions is given by the relation [79]:

$(\alpha h\nu) = A_o(h\nu - Eg)^{\frac{1}{2}}$

where, $h\nu$ is the photon energy, Eg is the band-gap, and A_o is a parameter associated with the transition probability and refractive index. α is calculated from the absorbance data using $\alpha = \frac{2.3 \times A}{t}$, where A is the absorbance and t is the film thickness. If a plot of $(\alpha h\nu)^2$ vs. $h\nu$ reveals a straight line, the sample has a direct gap absorption. The band-gap is determined by extrapolating the linear portion to zero.

Transitions where the wave vector is not conserved, $\Delta k \neq 0$, are also possible. These are indirect transitions across the gap. In order to conserve the total momentum, these

transitions require exchanging momentum with the lattice through the absorption or creation of a phonon. Compared to direct transitions, the required electron-phonon interaction makes these transitions less likely to occur. The absorption coefficient for indirect transitions is [79]:

$(\alpha h\nu) = A_1(h\nu - Eg)^2$

Besides band-to-band absorptions, other transitions are also possible, including impurity-to-band (discussed below), impurity-to-impurity, excitonic, and intraband transitions [79].

Perturbations in the band structure of the material can lead to the formation of band tails [79]. The perturbations are caused by imperfections in the crystal lattice, such as impurities, structural defects, and lattice disorder. The band tailing extends the conduction and valence band states into the energy gap. Electronic transitions between the tails cause an exponentially increasing absorption coefficient known as Urbach's rule: $d(\ln \alpha)/d(h\nu) = \frac{1}{k_B T}$. In the absorption spectrum, these Urbach tails appear as a broadening of the lowest energy transitions.

Ionized impurities will interact with band carriers through the Coulomb interaction. A positively charged donor, for example, will attract conduction band electrons and repel valence band holes causing a local distortion in the band structure. This effect can be more or less strong depending on how many impurities are clustered together at a particular spot in the material. Additionally, impurities can alter the density of states. When doped in large concentrations, the discrete impurity states can evolve into impurity bands. Optical transitions between these bands are permissible.

For the particular case of transition metal oxides, intra-ion transitions between d-states, or d-d transitions, provide an additional avenue for optical excitation. The electronic configuration of the metal ion is perturbed by the local chemical environment, the so-called crystal field splitting. The orbital degeneracy of the d-states is lifted the states are split into different energy levels. The splitting is strongly influenced by

coordination geometry. For example, octahedral sites result in a completely different arrangement of energy states than, say, a tetrahedral symmetry would produce.

The splittings are characteristic of the metal ion and the lattice. Therefore, transition metals doped into oxide lattices will produce characteristic absorption lines that can be used to identify the coordination and valence state of the dopant. This becomes particularly useful at high doping concentrations which may be near the solid solubility limit.

In this work, a Perkin-Elmer Lambda 800 UV/Vis double-beam spectrometer was used for optical absorption measurements. Samples were mounted to rigid opaque panels that contain a small hole, 3mm in diameter, for light to pass through. This ensures that only light passing through the sample is detected. It also keeps the transmitted beam size constant between samples. The samples were held normal to the incident light. Absorbance spectra were measured using unpolarized light with wavelengths between 200nm and 900nm. The data was used to determine the band gap as a function of doping. The optical signature of magnetic dopants was also used to confirm their solubility and valence state in the host lattice.

3.5.5 SQUID

Magnetic measurements were performed by my collaborators in Dr. Art Hebard's research group in the University of Florida's physics department. The measurements were done using a Quantum Design MPMS SQUID (Superconducting Quantum Interference Device) magnetometer. Currently, SQUIDs provide the most sensitive resolutions for magnetic field measurements.

Magnetization versus field loops were taken at various temperatures. Ferromagnetic materials will produce a finite hysteresis in these loops. Therefore, loop hysteresis was used to verify ferromagnetism in my samples. The samples were mounted inside a plastic drinking straw (which has no ferromagnetic components) and placed perpendicular to the applied field.

Additionally, Field Cooled/Zero Field Cooled (FC/ZFC) measurements were used to track the magnetic response as a function of temperature. FC measurements were performed by measuring the magnetization as the sample is cooled down to 10K in a small applied field. ZFC measurements were performed by cooling the sample to 10K in zero field and then applying a small field as the sample was heated back to room temperature while measuring the magnetization.

The diamagnetic response of the sample and substrate were subtracted from the M vs. H data. This was performed for each measurement. The magnet was swept to 5T to reveal the diamagnetic and paramagnetic response of the sample and substrate. The slope of the high field response is the background magnetic susceptibility, $\chi = \frac{M}{H}$. The susceptibility multiplied by the applied field is then subtracted from each data point.

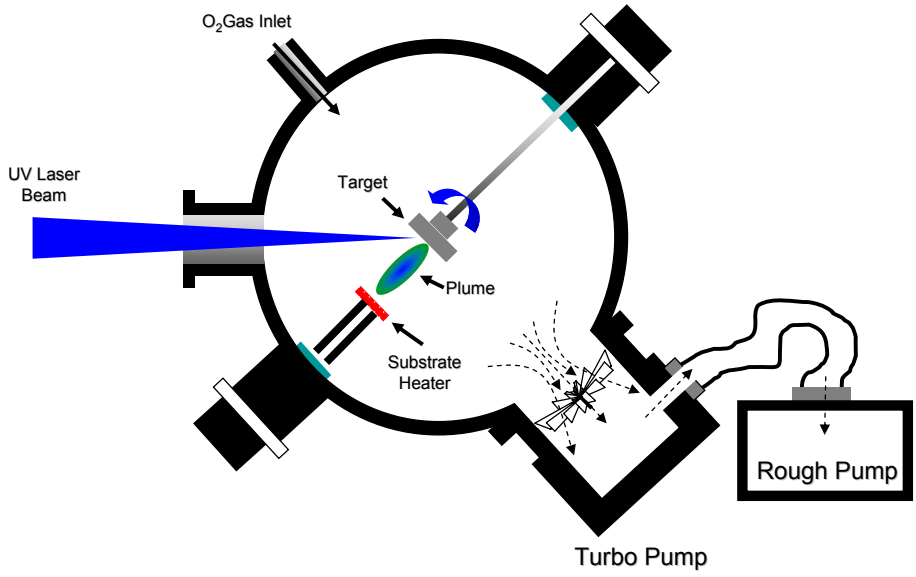

Figure 3-1. Schematic of pulsed laser deposition system.

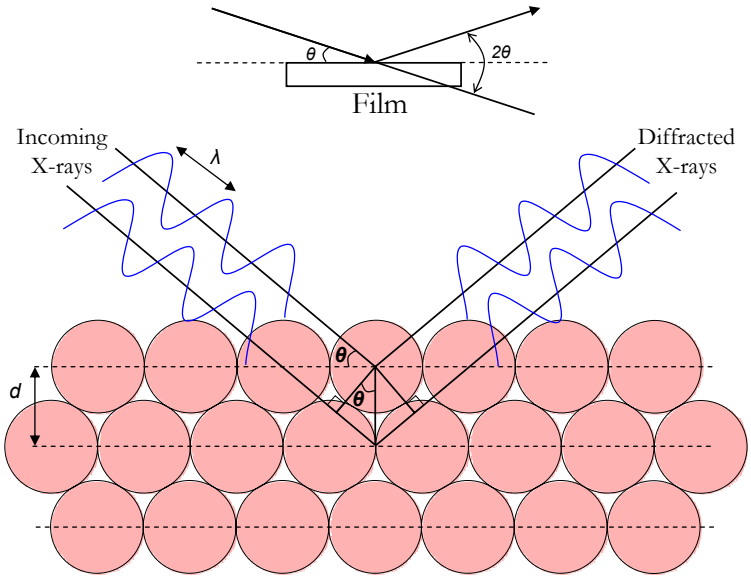

Figure 3-2. Visualization of Bragg's law for x-ray diffraction. Adapted from [80].

CHAPTER 4
PROPERTIES OF Mn-DOPED Cu_2O DMS

4.1 Introduction

Semiconducting oxides offer the potential for exploring and understanding spin-based functionality in a semiconducting host material. Dietl's theoretical prediction suggests that carrier-mediated ferromagnetism should be favored for heavily-doped p-type ZnO. However, this poses a serious challenge experimentally since ZnO is naturally an n-type semiconductor due to intrinsic defects and difficult to dope even moderately p-type. This poses the opportunity of using alternative wide-gap semiconductors that are naturally p-type to fabricate high Curie temperature DMS materials.

In this section, the properties of Mn-doped Cu_2O are explored. Cu_2O is a p-type, direct wide bandgap semiconductor that may hold interest in exploring spin behavior in an oxide DMS. Activities focused on understanding Mn incorporation during thin-film synthesis, as well as electrical transport and magnetic characterization. Ferromagnetism is observed in select Mn-doped Cu_2O films, but appears to be associated with Mn_3O_4 secondary phases. In phase-pure Mn-doped Cu_2O films, no evidence for ferromagnetism is observed above that attributed to the substrate.

4.2 Cu_2O: A Wide-bandgap P-type Semiconductor

Cu_2O (Cuprite) is one of the earliest know semiconductor materials. The development of copper-Cu_2O rectifiers dates back to the early 1920's, decades before silicon devices would dominate the semiconductor market. The rectifiers were easily fabricated by oxidizing pure copper at high-temperature inside a furnace, and were advantageous over earlier "point contact" (cat-whisker) rectifiers since the interface remained free of contamination and could be made uniformly over large areas of copper [81]. Cu_2O also has a large theoretical solar cell efficiency (18%) and was heavily studied for photovoltaic properties since the 1970's; however practical application of Cu_2O solar cells is limited due to difficulties with improving the semiconductor's electrical properties [82, 83]

Cu_2O is one of the few binary p-type semiconducting oxides. It has a direct band-gap of ~2.0 eV. The structure is cubic with $a = 4.27$Å(Figure 4-1). Oxygen atoms sit on a bcc lattice and are encaged by a tetrahedron of Cu atoms. Each Cu atom is two-fold coordinated resulting in the rare occurrence of O-Cu-O linear bonding. Each Cu-O bond length is about 1.84Å. The states at the top of the Cu_2O valence band are predominantly of Cu 3d character with O 2p states lying lower in the band [84]. The dominant method for p-type conduction is typically attributed to the formation of Cu vacancies in the lattice: $Cu^{1+} \rightarrow Cu^0 + h^+$

Using both DFT and DFT+U calculations, Nolan and Elliott have calculated the formation energy of the Cu vacancy to be on the order of 0.4-1.7eV [84]. They find the vacancy creates an acceptor state around 0.2eV above the Fermi level, and that the holes are delocalized around the vacancy. Experimentally, the acceptor states have been determined to be 0.26eV [85], 0.5eV [86], 0.4eV [87] above the valence band. The states at the top of the Cu_2O valence band are predominantly of Cu 3d character with O 2p states lying lower in the band [84]. Oxides typically have small hole mobilities since the O 2p valence bands are localized; however, the fully-occupied $3d^{10}$ states in Cu_2O are mobile when converted to holes [84]. Reasonable hole mobilities on the order of 100 $cm^2v^{-1}s^{-1}$ have been found experimentally [82, 88].

The number of reports exploring the magnetic properties of transition-metal doped Cu_2O are rather limited. There is also variation in the observed ferromagnetism between groups, similar to the contemporary state of research into other DMS materials, like TM-doped ZnO. Wei and coworkers found bulk pellets of Cu_2O doped with a nominal concentration of 1.7 at%Mn to be ferromagnetic up to 300K [89]. They report a magnetic saturation of $0.4\mu_B$/Mn at 10K which dropped to ~$0.05\mu_B$/Mn at room temperature. These results were calculated using the 1.7 at% nominal concentration, but their EDS results indicated a Mn concentration of ~0.3-0.5 at% which would result in a higher saturation (up to $2.5\mu_B$/Mn at 10K). The same group also found room temperature

ferromagnetism with a saturation moment of $0.6\mu_B$/Mn in Cu_2O:Mn films deposited by near-room temperature electrodeposition [90]. In both cases, the Cu_2O films doped with Mn showed lower resistivity than undoped films by a factor of 2. Mn-doped C_2O films were depostied by Pan et al. using rf magnetron sputtering [91]. The films were paramagnetic above 5K and showed some weak ferromagnetism near 5K with a moment of $5.3\mu_B$/Mn. Kale et al. used PLD to study 5 at% cobalt-doped Cu_2O films that were codoped with 0.5 at% Al, V, and Zn [92]. Ferromagetism was only observed in films codoped with Al, but persisted up to room temperatture with a moment of $0.44\mu_B$/Co. Doping Zn or V did not show ferromagnetism but caused the resistivity to decrease and increase, respictively. Since there was no correlation between the ferromagnetism and resistivity, they suggested the ferromagnetism may be realted to orbital defects introduced by the Al (which has s and p valence orbitals). In contrast, Antony et al. did observe ferromagnetism at 400K in 5%Co-doped Cu_2O nanoclusters [93]. DFT caluculations, employed by Sieberer and coworkers, show that the ferromagnetic properties of Cu_2O doped with Co or Mn is dependant upon the presence of defects (copper or oxygen vacancies) [94]. The found defect-free Mn-doped Cu_2O to be anitferromagnetic, while long-range ferromagnetism could occur when defects are present. For the case of Cu_2O doped with Co, the exchange constants are mostly ferromagnetic in defect free material (only nearest-neighbor sites were found to have antiferromagnetic coupling when the Hubbard U is increased). Cu vacancies were found to increase the Tc, while oxygen deficiency introduced strong oscillations in the magnetic exchange.

4.3 Experimental

Pulsed-laser deposition was used for film growth. Manganese-doped CuO targets were fabricated using high-purity CuO (99.995%), with MnO_2 (99.999%) serving as the doping agent. The targets were pressed and sintered at 860°C for 12hr, followed by 950°C for 2hr in air. Targets were fabricated with a composition of $Cu_{1.9}Mn_{0.1}O$. A KrF excimer laser was used as the ablation source. A laser repetition rate of 5 Hz was used, with a

target to substrate distance of 4 cm and a laser pulse energy density of 1-3 J/cm^2. The growth chamber exhibits a base pressure of $\sim 10^{-6}$ Torr. Film thickness was approximately 300 nm. Single crystal (0 0 1) $MgAl_2O_4$ and MgO were used as the substrate material in this study. Four-circle X-ray diffraction was used to determine crystallinity and dopant solubility. SQUID magnetometry was used to characterize the magnetic properties of the deposited films. In particular, it was used to determine the presence of ferromagnetism and measure the Curie temperature. Photoluminescence was used to characterize the optical properties of the material.

4.4 Results and Discussion

The epitaxial growth of Cu_2O thin films is dependent upon achieving oxidation conditions in which the Cu ion assumes a 1+ valence. Figure 4-2 shows the thermodynamic stability curves for Cu-Cu_2O-CuO as a function of oxygen partial pressure and temperature [95]. Using this, we find that epitaxial Cu_2O films can be grown from high-purity CuO or Cu targets using pulsed-laser deposition in an oxygen ambient. Figure 4-3 shows the X-ray diffraction data for a (0 0 1) Cu_2O film grown on (0 0 1) MgO with $P(O_2)$=4x10^{-4} Torr, T = 750°C, using a Cu target. Similar results were obtained on perovskite substrates, yielding p-type films with a carrier density of $\sim 10^{15}$ cm^3 and a room temperature mobility of 26 cm^2 v^{-1} s^{-1}. The primary focus of this work was to investigate the synthesis and properties of epitaxial Cu_2O doped with Mn. The selection of Mn as the transition metal dopant is based on the best available evidence in determining which magnetic impurities are likely to yield ferromagnetism. Manganese doping has resulted in interesting magnetic phenomenon in II-VI and III-V semiconductors, including spin glass or antiferromagnetic behavior for a number of systems, and is predicted to yield a high Curie temperature in ZnO as previously discussed. In the Cu_2O structure, the Cu^{1+} cation is twofold coordinated with an ionic radius of 0.46 Å. Mn^{2+} does not normally exhibit a twofold coordination in bulk materials. However, the radius for fourfold coordinated Mn^{2+} is 0.66 Å, which is close to that for the fourfold coordinated Cu^{1+} (0.60 Å). As a 2+ cation on

a 1+ site, Mn would be expected to compensate for the p-type conductivity observed in Cu_2O. The resistivity of Mn-doped Cu_2O films was significantly higher that that for undoped films.

The phase stability and solid solubility of Mn in Cu_2O was investigated as a function of deposition temperature and oxygen pressure. X-ray diffraction was used to determine conditions that limit segregation of secondary phases. Film growth was carried out over a temperature range of 300-700°C and an oxygen pressure of 10^{-3}, 10^{-4} Torr, or in vacuum. The base pressure of 10^{-5} Torr consists mostly of water vapor. Figures 4-4 to 4-6 show the X-ray diffraction data for Mn-doped films grown under these conditions. Several items should be noted. First, the Cu_2O phase is dominant over most of this range. This is surprising as the thermodynamic stability behavior suggests that CuO should be the stable phase for T $<$ 600 °C, P(O_2)=10^{-3} Torr, and T $<$ 550 °C, P(O_2)=10^{-4} Torr. Two possibilities exist in explaining this discrepancy. First, the doping of Cu_2O with Mn may shift the phase stability line. Second, epitaxy at low temperature may be sufficient to stabilize the Cu_2O phase. A segregation of Mn oxides in the Mn-doped films was also examined for the various film-growth conditions. The X-ray diffraction results indicate the presence of antiferromagnetic Mn_2O_3 as an impurity Cu_2O phase for T $\geq$ 500 °C. For films grown in vacuum, a weak peak that could be associated with either Mn_2O_3 or ferromagnetic Mn_3O_4 is observed. Phase-pure Cu_2O films were obtained at T $\leq$400 °C, indicating the metastable incorporation of Mn in the Cu_2O matrix. Figure 4-7 shows the phase assemblage as a function of growth conditions.

The magnetic properties of Mn-doped samples were measured using a Quantum Design SQUID magnetometer. Measurements were made on films grown at low temperatures, in which no Mn_3O_4 impurity phase peaks were evident in the X-ray diffraction patterns, as well as films grown at elevated temperatures. In order to characterize the magnetic properties of the Mn-doped samples, field-cooled and zero field-cooled magnetization measurements were performed from 4.2 to 300 K. By taking the difference (ΔM) between

these two quantities, the para- and diamagnetic contributions to the magnetization can be subtracted, leaving only a measure of ferromagnetic behavior. Figure 4-8 shows the ΔM difference as a function of temperature for a Mn-doped sample grown at 300 °C in 1 mTorr of O_2. At low temperature, a small, but finite field-cooled minus zero field-cooled magnetic signal persists up to ∼250 K as seen in figure 4-8. However, the magnetization signal is small, and can be attributed to a background magnetic signal from the $MgAl_2O_4$ substrate. Figure 4-9 shows the temperature dependent ΔM and M vs. H behavior for the substrate material without a Cu_2O film. For this and other phase-pure samples, no ferromagnetism could be detected above that attributed to the substrate.

We also investigated the magnetic properties of Mn-doped Cu_2O grown at 700 °C. These epitaxial Mn-doped Cu_2O films are clearly ferromagnetic with a Tc of ∼48 K as seen in figure 4-10. A key requirement in understanding ferromagnetism in transition metal doped semiconductors is to delineate whether the magnetism originates from substitutional dopants on cation sites, or from the formation of a secondary phase that is ferromagnetic. The importance of this issue cannot be understated. The concept of spintronics based on ferromagnetic semiconductors assumes that the spin polarization exists in the distribution of semiconductor carriers. Localized magnetic precipitates might be of interest in nanomagnetics, but is of little utility for semiconductor-based spintronics. The question of precipitates vs. carrier-mediated ferromagnetism is complex, and is a central topic of discussion for other semiconducting oxides that exhibit ferromagnetism, in particular the Co-doped TiO_2 system [96, 97]. Several issues must be addressed in order to gain insight into the possible role of secondary phase precipitates in the magnetic properties of transition metal doped semiconductors, specifically for Cu_2O films. First, one should identify all candidate magnetic phases possible from the assemblage of elements. The coincidence of Tc with a known candidate secondary ferromagnetic phase indicates a likely source of at least part of the magnetic signature. For the present material, metallic Mn is antiferromagnetic, with a Néel temperature of 100 K. In addition, nearly all of

the possible Mn-based binary and ternary oxide candidates are antiferromagnetic. The exception to this is Mn_3O_4, which is ferromagnetic with a Curie temperature of 46 K [98, 99]. X-ray diffraction measurements on the sample considered in figure 4-10 show evidence for the Mn_3O_4 phase. Obviously, the simplest explanation for ferromagnetic behavior in this material is Mn_3O_4 precipitates.

In addition to magnetization, the optical properties were also examined. The photoluminescence properties of the films were measured at room temperature using a He-Cd laser (325 nm) and taken over a wavelength range of 350-800 nm. The power density was 1 W/cm^2. A 0.3 nm scanning grating monochromator with a Peltier-cooled GaAs photomultiplier was utilized. The plot in figure 4-11 shows photoluminescence spectra for Mn-doped Cu_2O films deposited at 400 and 700 °C. The peak at 610 nm corresponds to the 1 s exciton [100–102]. This peak is rather weak and broad, but is most evident in the film grown at 700 °C. Note also the peak at ∼735 nm, which has previously been associated with extrinsic defects in the Cu_2O material [103]. Most of the additional broad peaks could be attributed to the background photoluminescence from the substrate. The emergence of intrinsic photoluminescence in the film grown at 700°C is consistent with the segregation of Mn from the Cu_2O matrix. It is also possible that luminescence from either Mn^{2+} or Mn^{4+} also contributes to the spectra observed.

With the advent of new equipment available in the lab for measurements, resistivity and Hall data were collected on films that were aged ∼3–4 years. There was no visual decomposition of the films, but a detailed study of the microstructure was not conducted. Measurements were performed in Van der Pauw configuration using a varying magnetic field with a maximum strength of 1T. Soldered indium contacts were placed on the corners of the sample. Figure 4-12 shows the collection of measurements on various samples. The films appear to become slightly more resistant with higher growth temperature, but the trend is small and may be insignificant. The Hall mobility increases with higher growth temperature, but there does not seem to be a significant relationship with growth pressure.

This may be an indication of better crystalline quality with higher growth temperatures, which leads to enhanced mobility of the carriers. While the mobility increases, the carrier concentration drops off with higher temperature. It is also important to remember that different secondary phases are evolving in the microstructure as the growth conditions are varied which presumably have an impact on the observed electrical properties.

Temperature dependent Hall effect data was studied on a newly deposited film grown at 400C in 1mTorr O_2 on a $MgAl_2O_4$ substrate. Hall data was taken in a Van der Pauw configuration with four 80nm thick platinum contacts sputtered on the corners of the sample. Pt was chosen for it's high barrier height (∼5.6eV) to make an ohmic contact to the p-type film. The sample was measured in a temperature range from 200K to 400K. The room temperature resistivity was 885 ohm-cm, but quickly became too resistive ($>10^6$ ohm-cm) to measure accurately below 200K. The acceptor state activation energy can be calculated assuming an Arrhenius-type activation of the form: $\log \rho = \log A + \frac{-Ea}{2.303 \times kT}$, where ρ is the resistivity in ohm-cm, A is a constant, Ea is the activation energy, k is Boltzmann's constant, and T is temperature in degrees Kelvin. The slope was calculated by a linear least-squares fit through the data (inset of figure 4-13). Ea was determined to be 0.25eV. This value is similar to the value (0.2eV) calculated for acceptor states arising from Cu vacancies using first-principles DFT and DFT+U theories [84]. It is also consistent with the 0.22-0.25eV values found for Cu_2O films doped with Ni cations [104]. The temperature dependent resistivity, mobility, and carrier concentration is given in figure 4-13 with the $\log \rho$ vs. 1/T activation fit. The value of the resistivity and hall resistivity at 300K as a function of field is given in figure 4-14. The positive slope of the hall resistivity clearly indicates p-type behavior and is linear throughout the field sweep. No indication of anomalous Hall effect is observed. The resistivity has a slight negative MR (-0.4%) at 7 Tesla. The film became too resistive to measure at lower temperature.

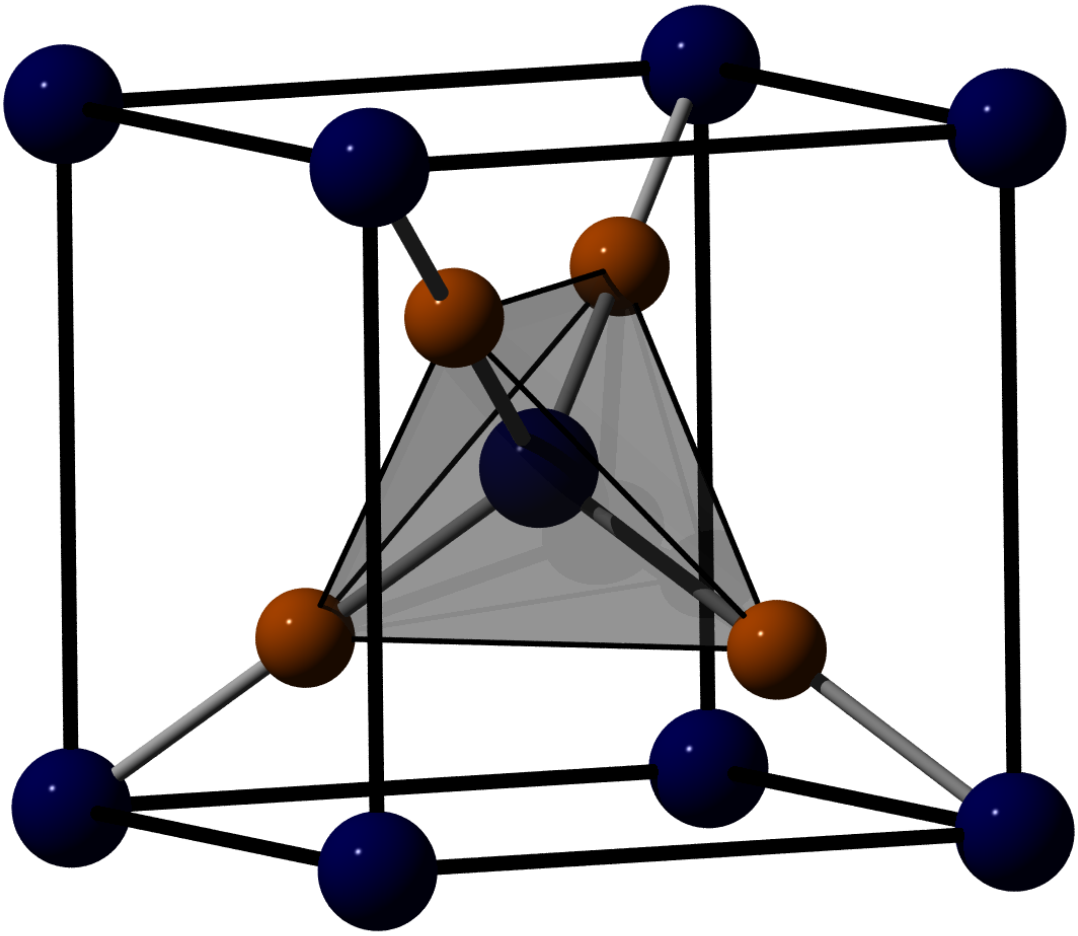

Figure 4-1. Cubic unit cell of Cu_2O. Oxygen atoms occupy bcc lattice positions that are surrounded by a tetrahedron of Cu atoms. Cu atom are therefore linearly coordinated to two oxygen atoms. This forms a rare occurrence of lineal O-Cu-O bonding.

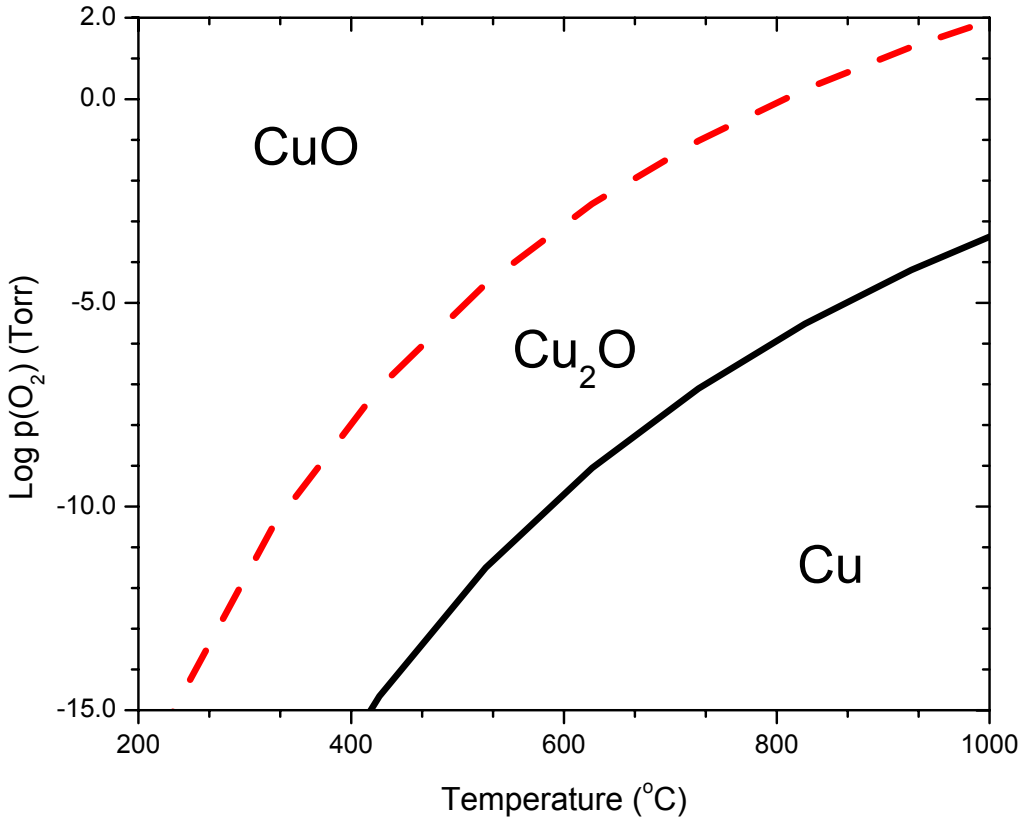

Figure 4-2. Phase Stability curves for the Cu-Cu_2O-CuO system.

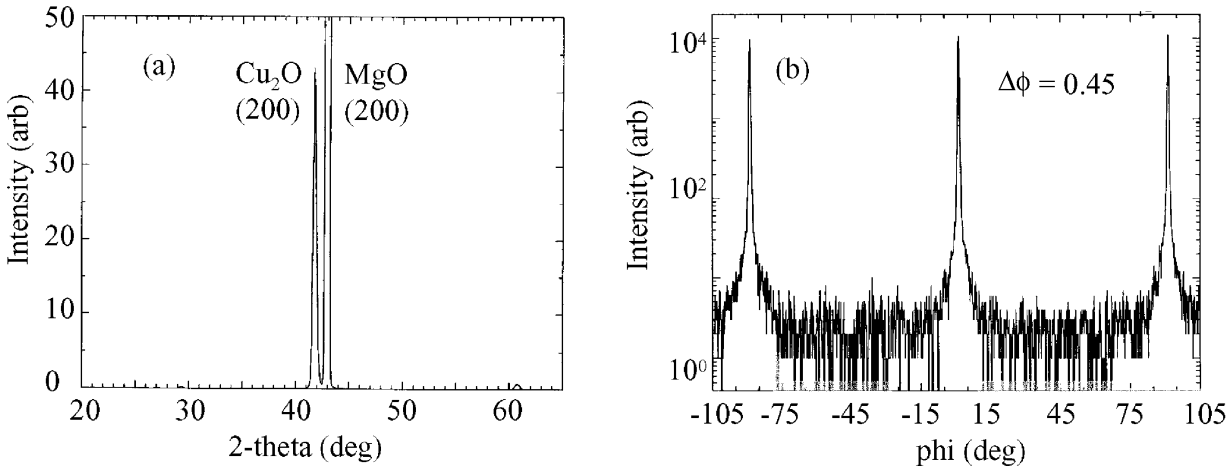

Figure 4-3. X-ray diffraction data for epitaxial Cu_2O on (001) MgO, showing both (a) out-of-plane and (b) in-plane orientation.

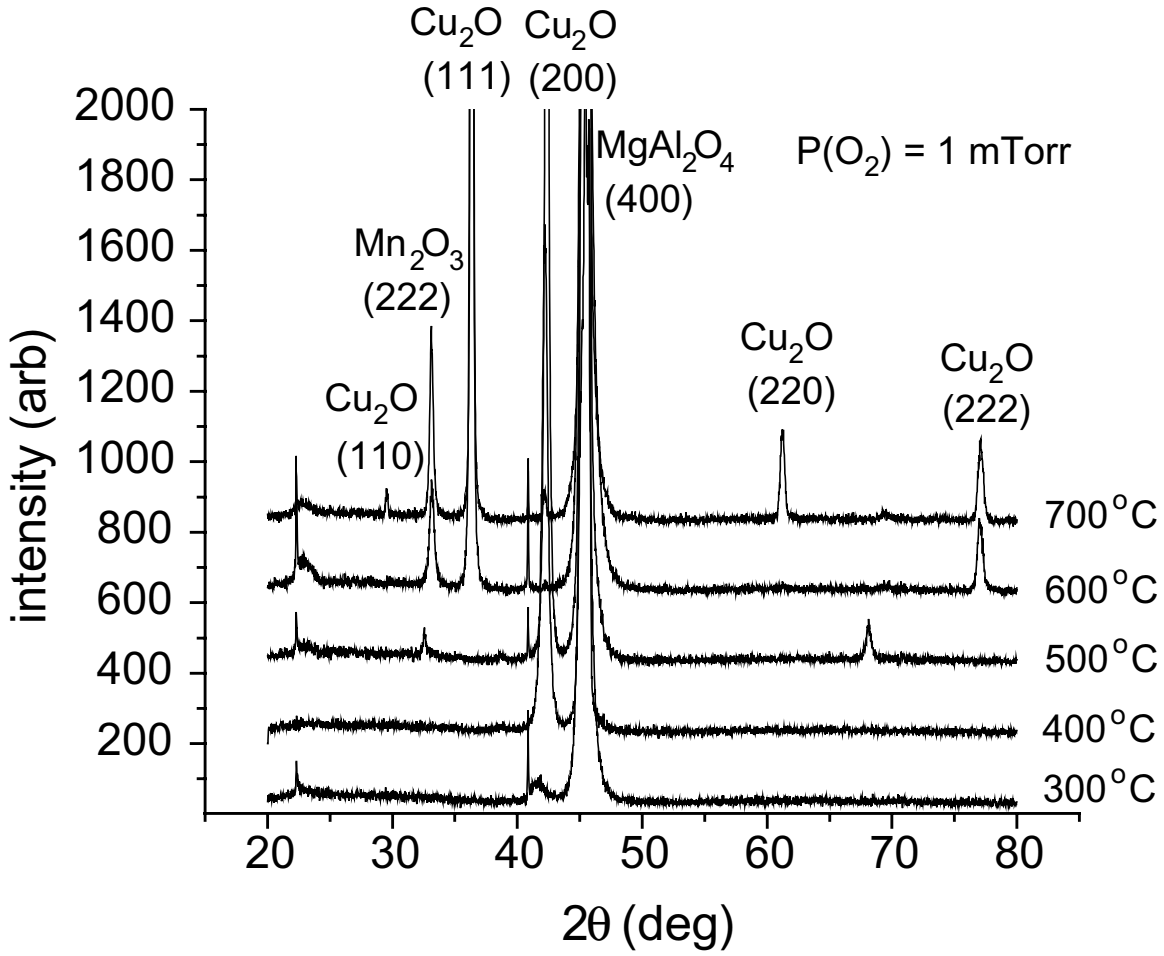

Figure 4-4. X-ray diffraction data for Mn-doped Cu_2O films grown on (001) $MgAl_2O_4$ in an oxygen pressure of 1mTorr.

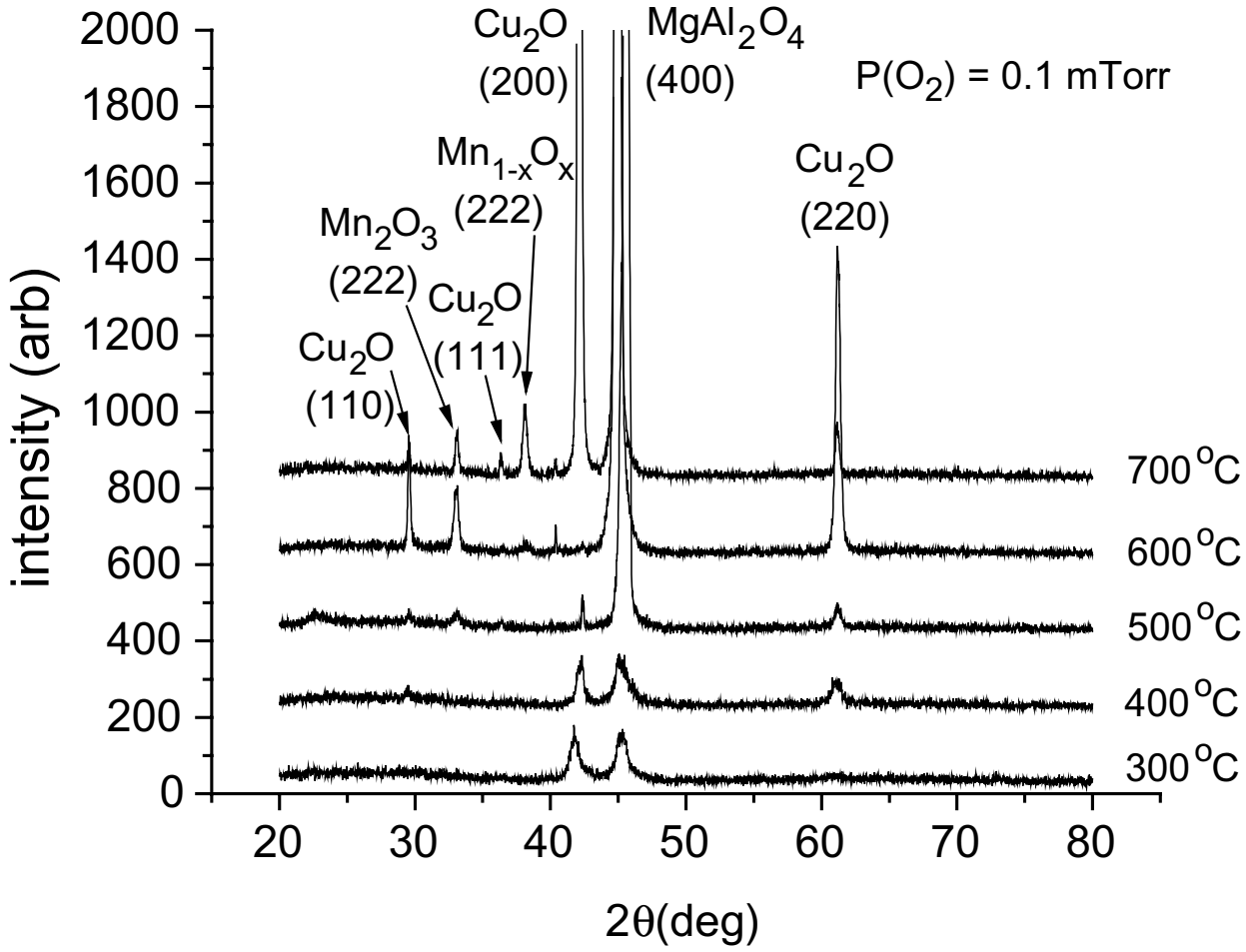

Figure 4-5. X-ray diffraction data for Mn-doped Cu_2O films grown on (001) $MgAl_2O_4$ in an oxygen pressure of 0.1mTorr.

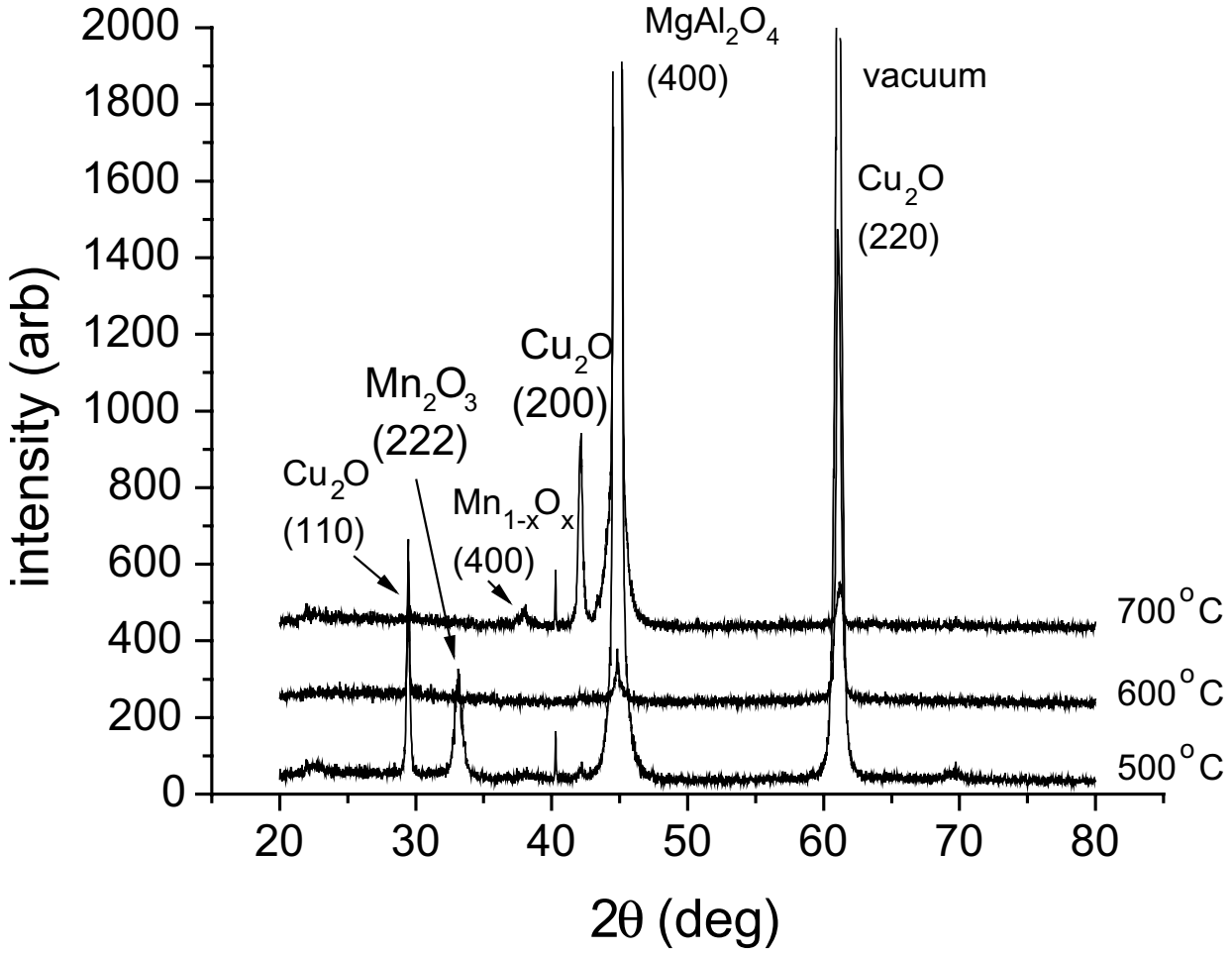

Figure 4-6. X-ray diffraction data for Mn-doped Cu_2O films grown on (001) $MgAl_2O_4$ in vacuum.

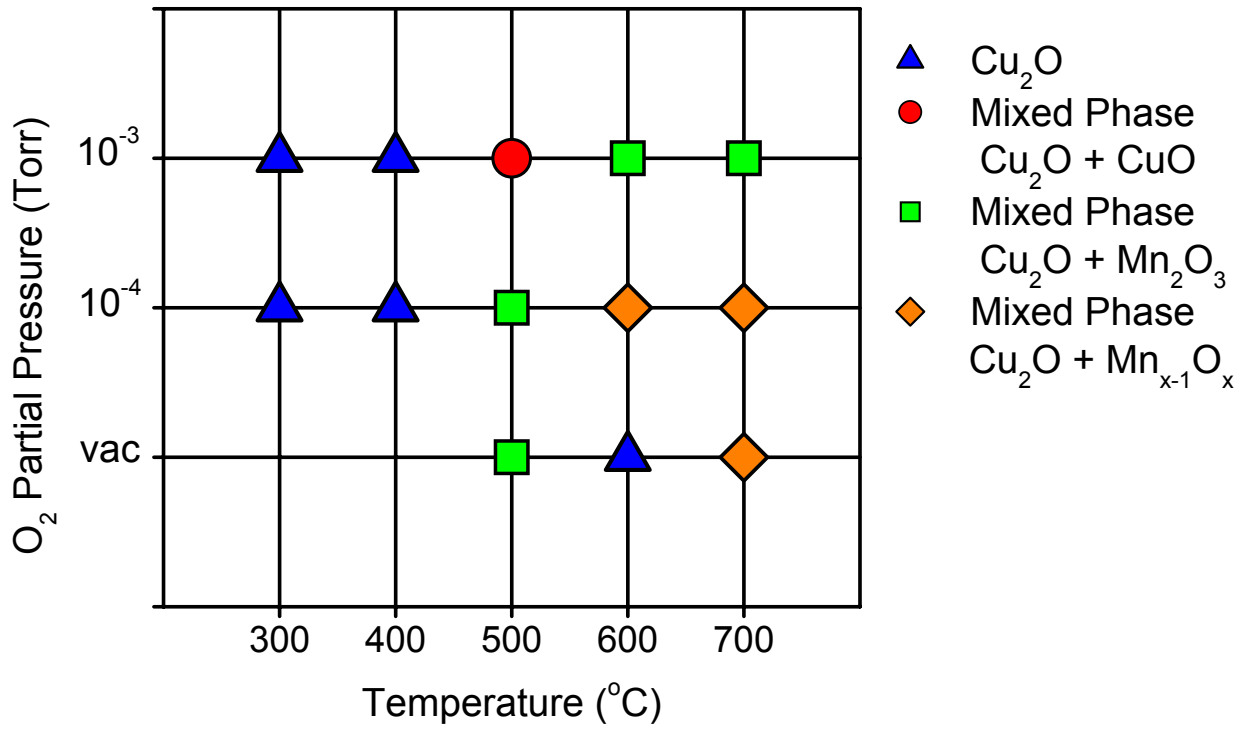

Figure 4-7. Phase assemblage for films grown under different conditions.

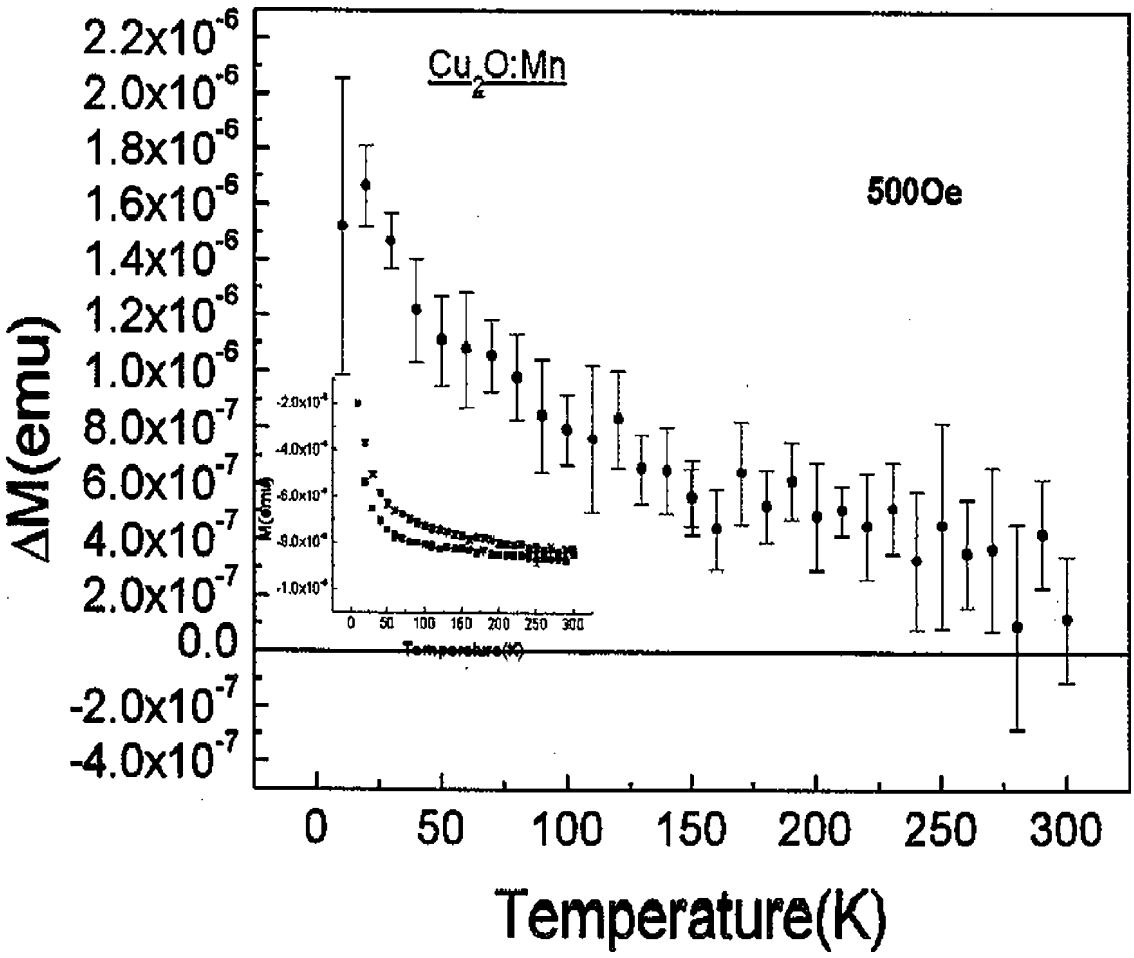

Figure 4-8. Magnetic behavior for an epitaxial Mn-doped Cu_2O film grown at 300°C and 1mTorr of oxygen.

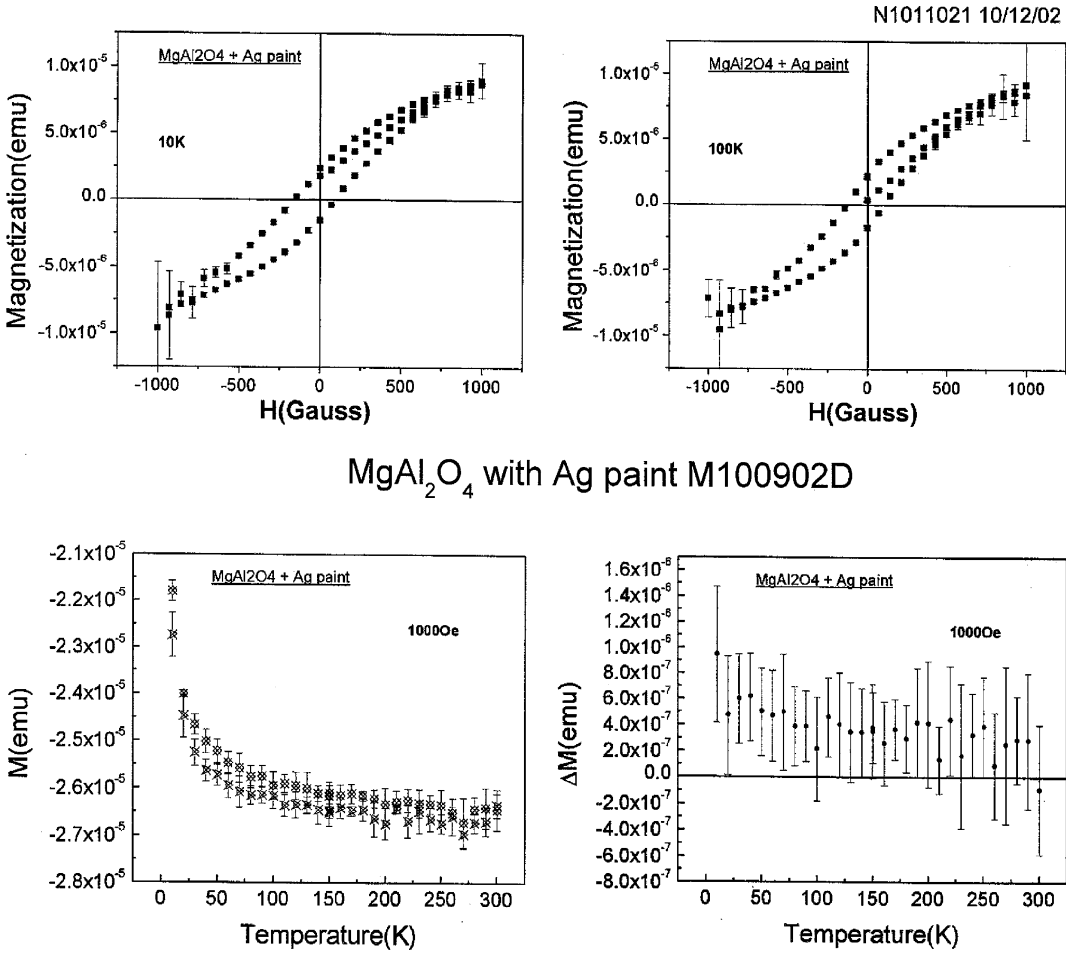

Figure 4-9. Magnetic behavior for $MgAl_2O_4$ substrate.

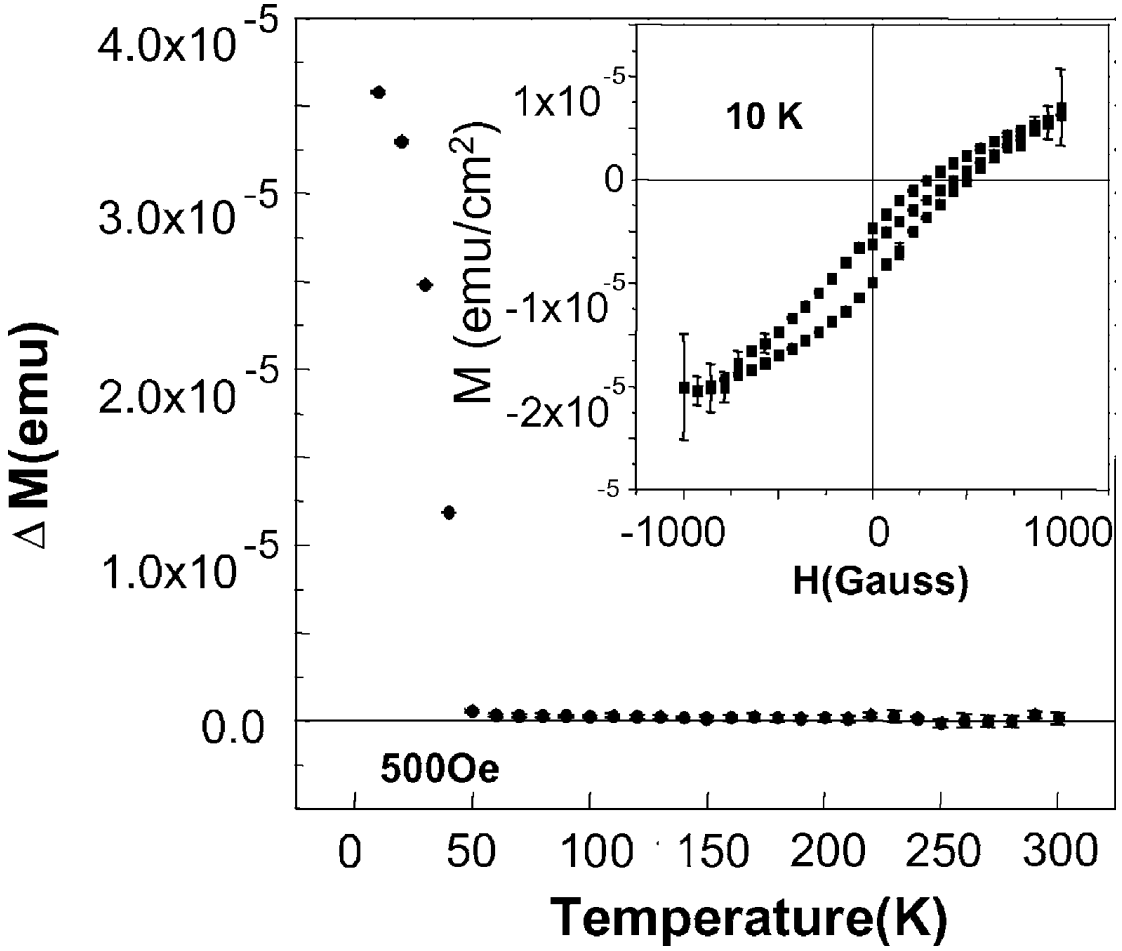

Figure 4-10. Magnetic behavior for an epitaxial Mn-doped Cu_2O film grown at 700°C in vacuum.

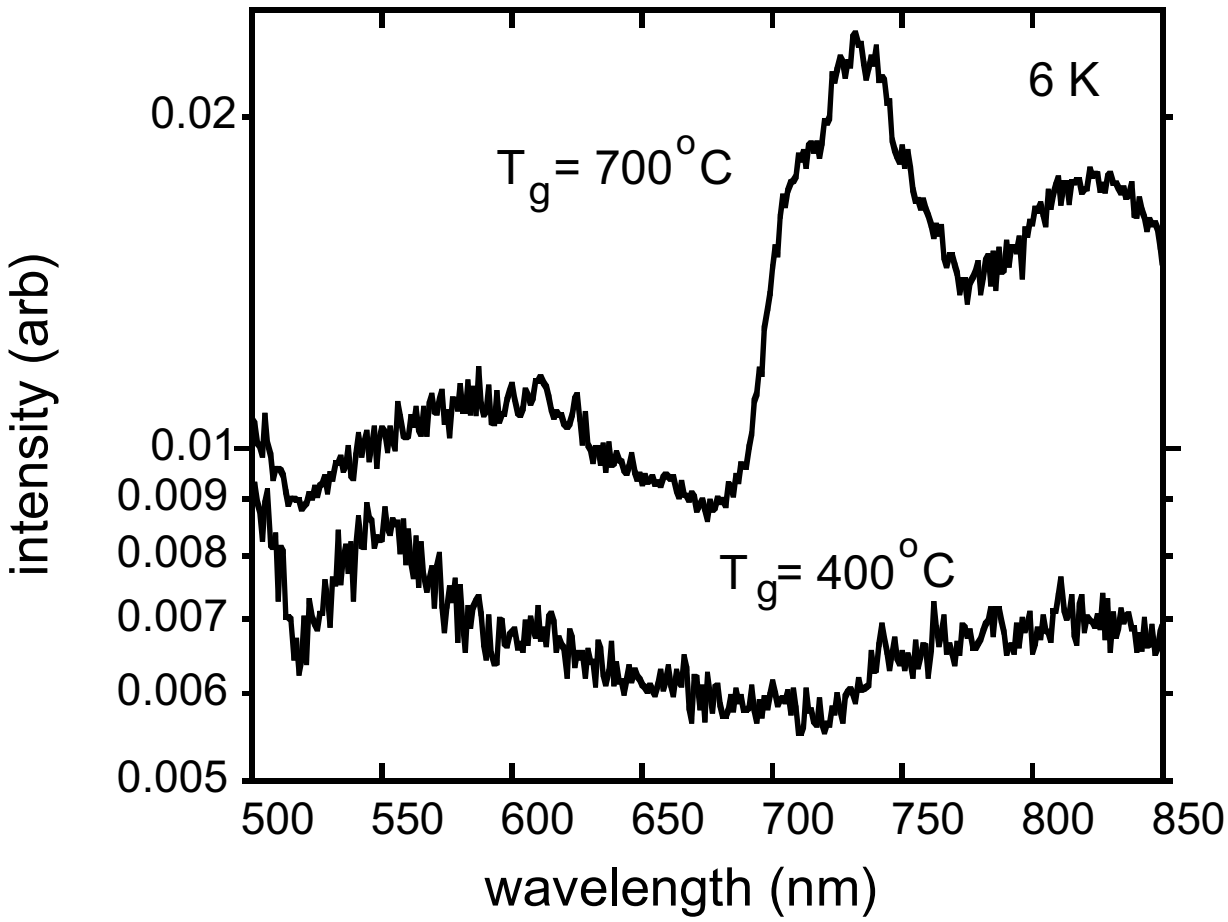

Figure 4-11. Low temperature photoluminescence spectra for Mn-doped Cu_2O films.

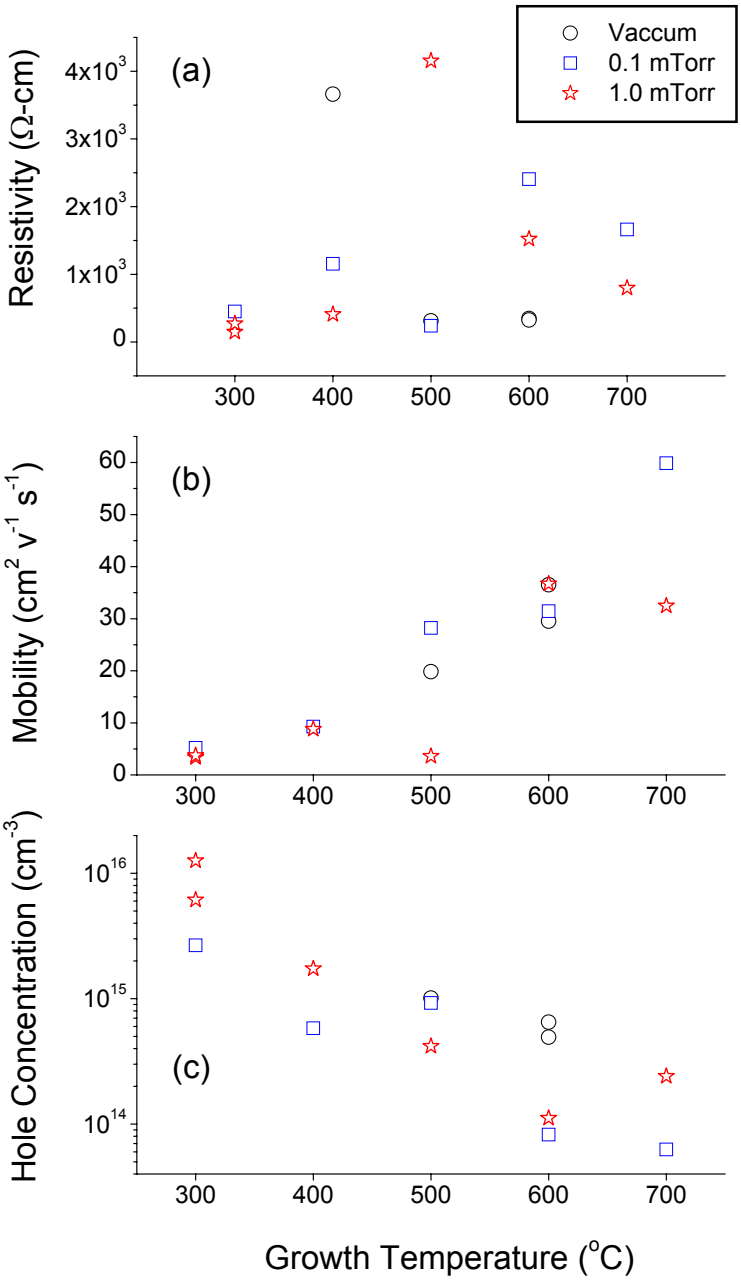

Figure 4-12. Transport data for 1% Mn-doped Cu_2O films. The resistiviy (a), mobility (b), and hole concentration (c) are plotted as a function of growth temperature for different oxygen pressures.

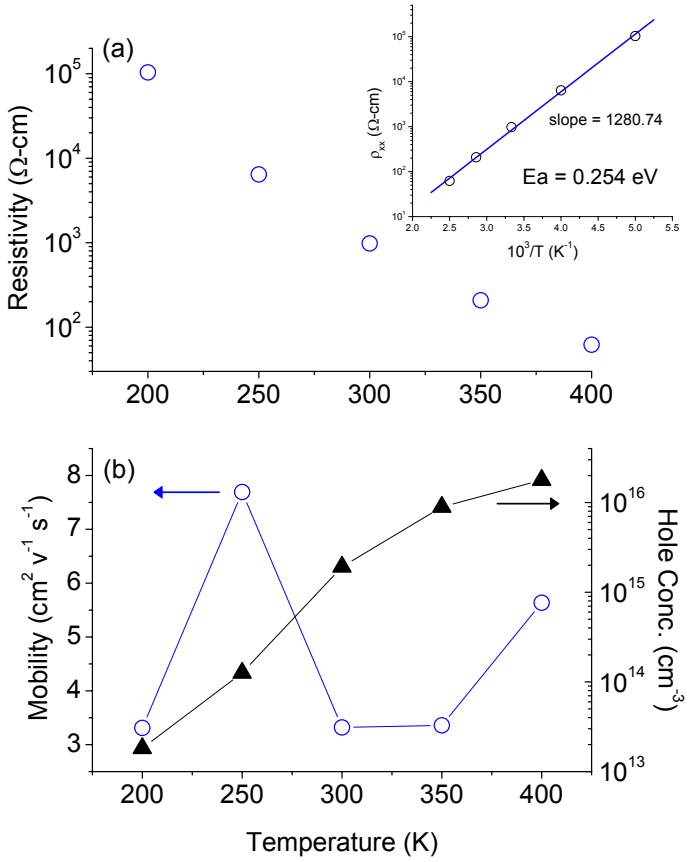

Figure 4-13. Temperature-dependent transport data for 1% Mn-doped Cu_2O film. (a) The resistiviy vs. temperature. The inset shows resistivity vs. 1/T with a linear fit to calculate the activation energy of acceptor states above the valence band. (b) The mobility [hollow circles] and the hole concentration [filled triangles].

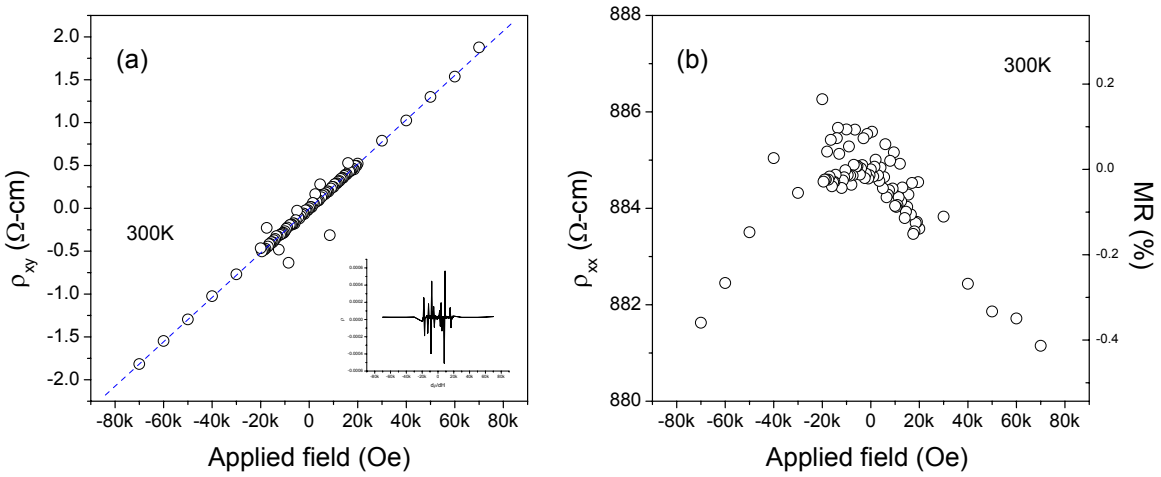

Figure 4-14. Field-varying transport measurements for a 1% Mn-doped Cu_2O film. (a) Hall resistivity. Dotted line is a linear fit used to calculate the Hall coefficient. The inset shows the derivative of the data to emphasize there is no curvature from the anomalous hall effect. (b) Magnetoresistance.

CHAPTER 5
PROPERTIES OF ZnO CODOPED WITH Mn AND Sn

5.1 Introduction

As discussed in Chapter 2, several recent theories regarding the origin of ferromagnetism in ZnO DMS emphasize the importance of holes in mediating the exchange interaction between doped Mn atoms. Dietl's mean-field calculations predict that room temperature ferromagnetism is possible in Mn-doped ZnO that is heavily doped with holes, while carrier-mediated ferromagnetism in n-type material should be limited to lower temperatures. The recent work by Kittilstved and coworkers demonstrate that the Mn^{+3} charge transfer energy lies close to the valence band, similar in energy to ZnO acceptor states. It is thought this can lead to large hybridization necessary to support ferromagnetic ordering. The advancement of spintronics as a technology depends upon the development and understanding of semiconductors that can support spin-polarized carrier operation at or above room temperature.

In this chapter, the synthesis and magnetic properties of Mn-doped ZnO epitaxial films codoped with Sn are examined. Codoping allows independent control over the magnetic and electronic properties of the material by doping for each separately. In II-VI materials, Mn^{+2} is isovalent and does not introduce carriers. By codoping II-VI semiconductors, Mn provides the localized spins while an additional dopant can be used to control the carrier concentration. This provides a convenient platform to study the effects of carrier concentration on the observed magnetic properties in ZnO DMS. As a group IV cation, Sn can exist in either the 4+ or 2+ valence, although the 4+ valence is most common. As such, it can serve either as a doubly ionized donor or isoelectronic impurity. For the ZnO films deposited in this work, Sn behaves as a donor. The magnetization dependence on the carrier density is investigated.

Superconducting quantum interference device magnetometry measurements indicate that the films are ferromagnetic with an inverse correlation between magnetization and

electron density as controlled by Sn doping. Magnetism in low free-electron density material is consistent with the bound magnetic polaron model, in which bound acceptors mediate the ferromagnetic ordering. Increasing the electron density decreases the acceptor concentration, thus quenching the ferromagnetic exchange. This result is important in understanding ferromagnetism in transition-metal-doped semiconductors for spintronic devices.

5.2 Experimental

Epitaxial Mn, Sn-doped ZnO films were grown by conventional pulsed-laser deposition. Laser ablation targets were prepared from high-purity powders of ZnO (99.999%), with MnO_2 (99.999%) and SnO_2 (99.95%) serving as the doping agents. The pressed targets were sintered at 1000°C for 12 h in air. The targets were fabricated with a nominal composition of 3 at.% Mn and 0, 0.1, 0.01, and 0.001 at. % Sn. A Lambda Physik KrF excimer laser was used as the ablation source. The laser energy density was 1-3 J /cm^2 with a laser repetition rate of 1 Hz and target-to-substrate distance of 6 cm. The growth chamber exhibits a base pressure of 10^{-5} Torr. Films were deposited onto single-crystal, c-plane oriented sapphire substrates. Film growth was conducted over a temperature range of 400-600°C. An oxygen pressure of 20 mTorr was used for all film growth experiments. Film thicknesses were approximately 300-400 nm. X-ray diffraction was used to determine the crystallinity and secondary phase formation. Superconducting quantum interference device (SQUID) magnetometry was used to characterize the ferromagnetic behavior of the doped films, focusing on the films grown at 400°C.

5.3 Results and Discussion

The phase stability and solid solubility of Mn in the ZnO films were investigated as a function of growth temperature for films with varying Sn concentrations. Figure 5-1 shows the x-ray diffraction scans for films deposited under the given growth conditions. In all cases, the dominant film peaks correspond to c-axis perpendicular ZnO. Note that,

for some of the films, a peak located around 64.55° appears. At first glance, this peak was assigned to the (400) reflection of Mn_3O_4. The (400) diffraction peak of Mn_3O_4 has a 2θ value of 64.65° which closely matches the observed peak. However, the formation of Mn_3O_4 at 400°C and not at higher temperatures in 0.1%Sn doped samples is peculiar and should be questioned. Note that previous reports from Fukumura indicated that epitaxial ZnO films with a Mn concentration as high as 35% could be achieved while maintaining the wurtzite structure using pulsed-laser deposition [37]. The observed peaks are small (a few hundred counts above background) and rather sharp. A similar peak is observed in undoped ZnO films, which is included in Figure 5-1. Therefore, it is believed this peak is associated with the ZnO and represents the K_β artifact from the ZnO (004) peak. The XRD used in these experiments has a Ni filter for attenuating Cu K_β radiation, but the K_β line is clearly penetrating because the K_β peak from the ZnO (002) peak is present at 31°. The K_β peaks can be checked by taking the d-spacing of the ZnO (002) planes and calculating the respective 2θ value for K_β radiation (λ=1.3922 Å) using the Bragg equation $n\lambda = 2d \sin\theta$. The 2θ value for the ZnO(004) K_β peak is determined to be around 64.6°, which is commensurate with the observed peak. Note that even if the peak does represent the formation of Mn_3O_4 in the film, the phase would not contribute to a high temperature ferromagnetic signal since the Curie temperature is only 50K as mentioned previously. Also notice that the precipitation of Sn-containing phases is not observed in the diffraction scan, nor is it expected even if present as the nominal concentration of Sn in the films is $\leq$0.1%.

The epitaxial nature of the ZnO films was determined using four-circle high-resolution x-ray diffraction. Figure 5-2(a) shows an ω rocking curve about the ZnO (002) peak for the film grown on c-plane sapphire substrate at a growth temperature of 500°C and Sn concentration of 0.1%. A $\frac{1}{2}$° divergence slit was placed over the x-ray source and a 1mm receiving slit was placed in front of the detector. The ZnO (002) rocking curve displays a full width at half maximum (FWHM) of 0.47°. The in-plane alignment is evident in

the phi scan and pole figure of the ZnO (101) plane shown in figure 5-2(b). The 60° peak intervals are consistent with the hexagonal symmetry of the epitaxial ZnO wurtzite structure.

The Mn valence state in the ZnO lattice was investigated using x-ray photoemission spectroscopy (XPS). Figure 5-3 shows the core level XPS spectra for a ZnO film doped with 3%Mn and 0.01%Sn. The data was charge corrected by shifting the O 1s peak to 530.1 eV. The film was sputtered with Ar^+ for 4 min. to remove surface contamination. The Mn $2p_{3/2}$ binding energy is 640.7 eV. This is consistent with values assigned to Mn^{+2} in ZnO [105, 106]. There is a ~6eV energy difference between the Mn $2p_{3/2}$ and its higher binding energy satellite peak. The binding energy and satellite peak are consistent to the reported for single crystal MnO by Langell et al. [107]. They found the satellite structure to be particularly sensitive to the oxide stoichiometry. In the case of Mn_2O_3 (the Mn^{+3} valence) the binding energy was higher at 641.1 eV and the satellite structure tended to decrease for the higher oxide phases [107]. The binding energies for metallic Mn and Mn^{+4} sit close to the Mn^{+2} value, but the energy for Mn has been seen at 637.7 eV and that for Mn^{+4} at 642.4 eV in ZnO [105]. The binding energy and satellite structure for the measured film suggests that most of the Mn doped into the ZnO is in the +2 valence state.

The room-temperature resistivity for the Mn-doped ZnO films with varying concentrations of Sn was determined using a four-point van der Pauw geometry. Defect chemistry calculations for Mn-doped ZnO indicate that Mn^{+2} forms a donor level ~2.0 eV below the conduction-band edge [108]. This deep donor state with Mn substitution on the Zn site in ZnO has no direct effect on the electron concentration at room temperature. However, defect chemistry calculations also indicate a reduction in Zn interstitials with Mn doping. Zn interstitials are generally accepted as the primary shallow donor defects in nominally undoped ZnO. This will yield an increase in resistivity for Mn-doped films as compared to undoped material [108–110]. The Mn-doped ZnO films with no Sn exhibit a

resistivity on the order of 10^2 Ω-cm with a carrier density of mid-10^{16}/cm^3. This carrier density is substantially lower than that seen for undoped epitaxial films and is consistent with the reduction of shallow donors. Limited results on the doping behavior of Sn in ZnO indicate that it introduces a donor state [111–115], although in some II-VI compound semiconductors, Sn is an amphoteric dopant, substituting on either the II or VI site [116, 117]. For ZnO, the expectation is that Sn will substitute on the Zn site due to a close match in ionic radii between Zn^{+2} (0.074 nm) and Sn^{+4} (0.069 nm). For the epitaxial films considered in this work, Sn behaves as a donor. The resistivity of ZnO:Mn films with various Sn content is shown in Table 5-1. The resistivity of the films drops rapidly with Sn doping with a minimum of 0.185 Ω cm for a Sn concentration of 0.1%. The most common valence state of Sn is +4, yielding a doubly ionized donor if doped substitutionally on the Zn site. Hall measurements indicate that the films are increasingly n-type with Sn doping up to 0.1 at. %. It should also be noted that other work has shown that the addition of Sn to ZnO ceramics also yields an enhancement in crystallinity [111, 112].

The magnetic properties of the films were measured using a Quantum Design SQUID magnetometer. The diamagnetic responses of the substrate and host semiconductor were subtracted from the magnetization plots. The primary focus of the measurements was to determine how the magnetic properties of the films changed as a function of electron density as controlled by Sn concentration. Samples that showed minimal amounts of possible Mn_3O_4 precipitation via x-ray diffraction were used for the SQUID measurements. All the M vs. H loops show hysteretic behavior with a finite coercivity and loop closure. From the hysteresis curves, an increase in loop width is observed with increasing Sn concentration. Figure 5-4 shows the coercive field as a function of Sn concentration, suggesting domain pinning as the Sn doping is increased. It is unclear why the addition of Sn enhances the hysteretic magnetization response in the Mn-doped films. It might indicate enhanced pinning of domains due to the Sn dopants.

Most interesting is the saturation magnetization behavior as Sn content is increased. As noted earlier, increasing Sn concentration increases electron density and conductivity. Figure 5-5 shows the room-temperature magnetization versus field behavior for the ZnO samples containing 3% Mn and Sn contents of 0, 0.1, 0.01, and 0.001%. Magnetization is given as the magnetic moment per Mn dopant ion. Initially, there is an increase in magnetization with minimal Sn doping. However, with increasing Sn doping, there is an inverse correlation between the Sn content and saturation magnetization. As the electron density increases with Sn doping, the magnetization decreases. The maximum magnetization corresponds to a magnetic moment per Mn ion of $\sim$0.5 μ_B/Mn. This is consistent with the bound magnetic polaron model in which only a fraction of the Mn ions are expected to order ferromagnetically due to competing superexchange antiferromagnetic interactions between neighboring Mn ions [118]. The inverse correlation of saturation magnetization with electron density is interesting and provides some insight into the mechanism for ferromagnetism in Mn-doped ZnO. Overlap of the Mn d-states with the valence band suggests that holes are necessary in order to induce ferromagnetic order. For semi-insulating films to exhibit ferromagnetism, the bound magnetic polaron model provides a mechanism whereby holes that are localized at or near the Mn ions are responsible for mediating ferromagnetism. The addition of electrons to the system will move the Fermi energy level up in the band gap, resulting in a decrease in hole density and a reduction in magnetization. This is consistent with Kittilstved and coworker's observation where ferromagnetism was induced when the holes from the acceptor states hybridize with the charge transfer state Mn. Ferromagnetism was observed when the ZnO was locally doped p-type, but no ferromagnetism was observed when doped n-type. This appears consistent with early work on trivalent-doped (Zn,Mn)O where no ferromagnetism was observed for heavily n-type films. It may also explain the discrepancy from other studies of Mn-doped ZnO films in which the intrinsic defect-mediated donor states are high in density. It is important to note the need to maintain a Mn concentration low

enough to avoid MnMn antiferromagnetic interactions, which are likely to dominate high Mn-doped ZnO films.

In conclusion, the magnetic and transport properties of Mn-doped ZnO thin films codoped with Sn were examined. Results indicate that the films are ferromagnetic with an inverse correlation between magnetization and electron density as controlled by Sn doping. The results are most consistent with the bound magnetic polaron model in which bound acceptors mediate the ferromagnetic ordering. Increasing the electron density decreases the acceptor concentration, thus quenching the ferromagnetic exchange. This result is relevant to understanding ferromagnetism in transition-metal doped semiconductors.

Table 5-1: Resistivity as a function of Sn content in codoped ZnO:3%Mn films.

	Sn concentration			
	0.0%	0.001%	0.01%	0.1%
Resistivity (Ω-cm)	195	320	17	0.185

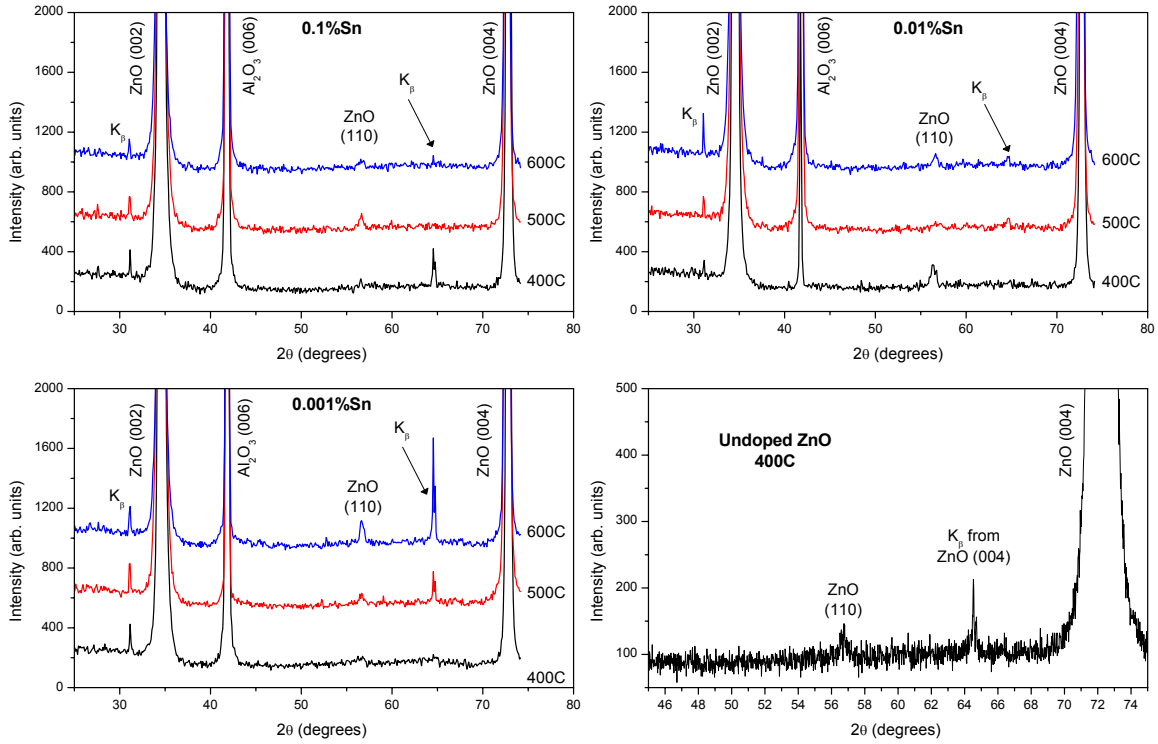

Figure 5-1. X-ray diffraction of ZnO films codoped with Mn and Sn grown at oxygen partial pressure of 20mTorr and growth temperature of 400, 500, and 600°C. The diffraction pattern for an undoped ZnO film grown at 400°C in vacuum is also shown. The peak at 2θ=64.55° is clearly evident in the undoped film and attributed to the K_β artifact from the ZnO (004) reflection.

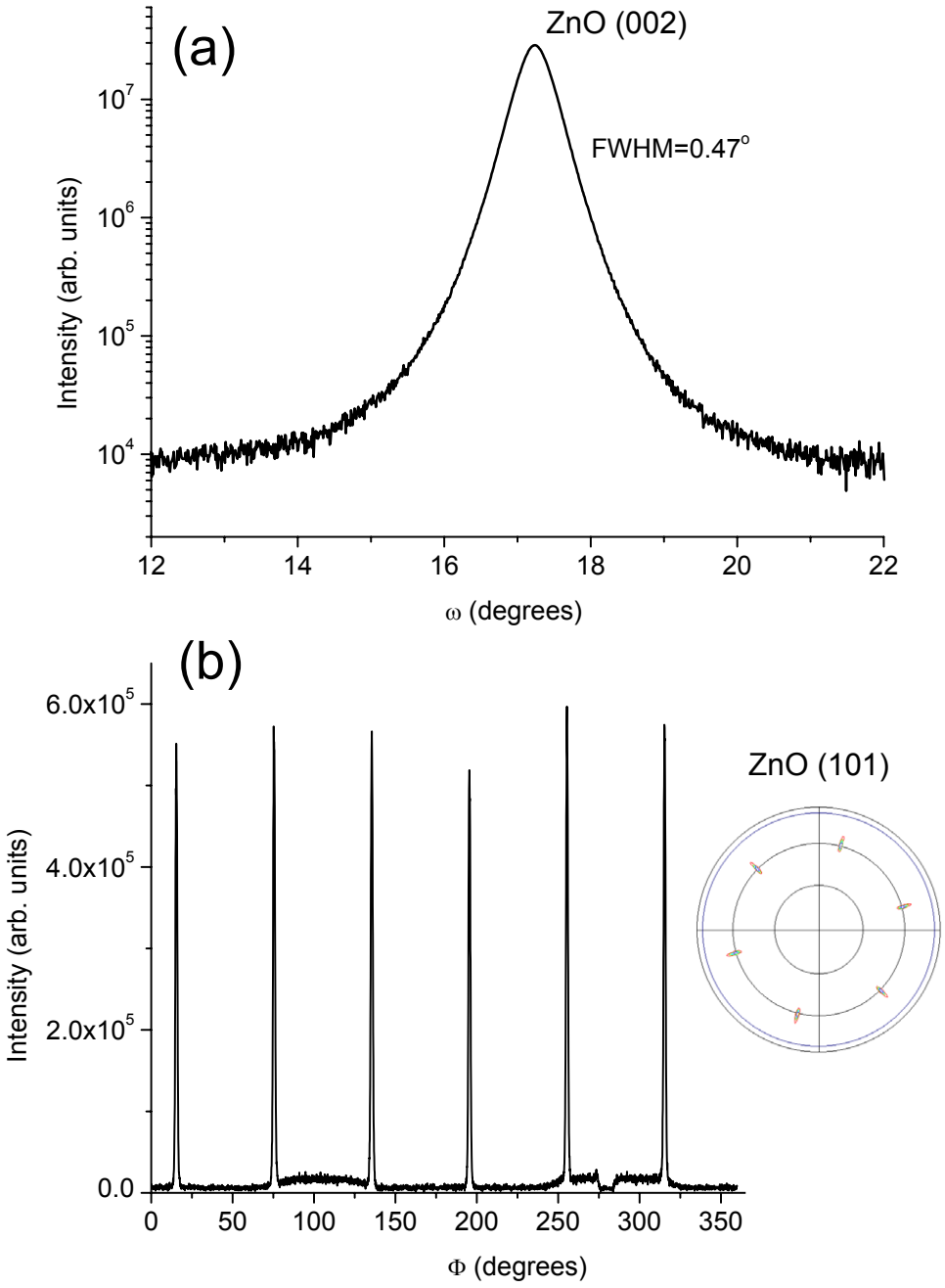

Figure 5-2. X-ray diffraction of an epitaxial ZnO film doped with 3%Mn and 0.1%Sn that was deposited at 500°C and p(O_2)=20mTorr. (a) an ω-rocking curve of the ZnO (002) peak with a FWHM of 0.47°. (b) in-plane Φ-scan and pole figure of the ZnO (101) planes.

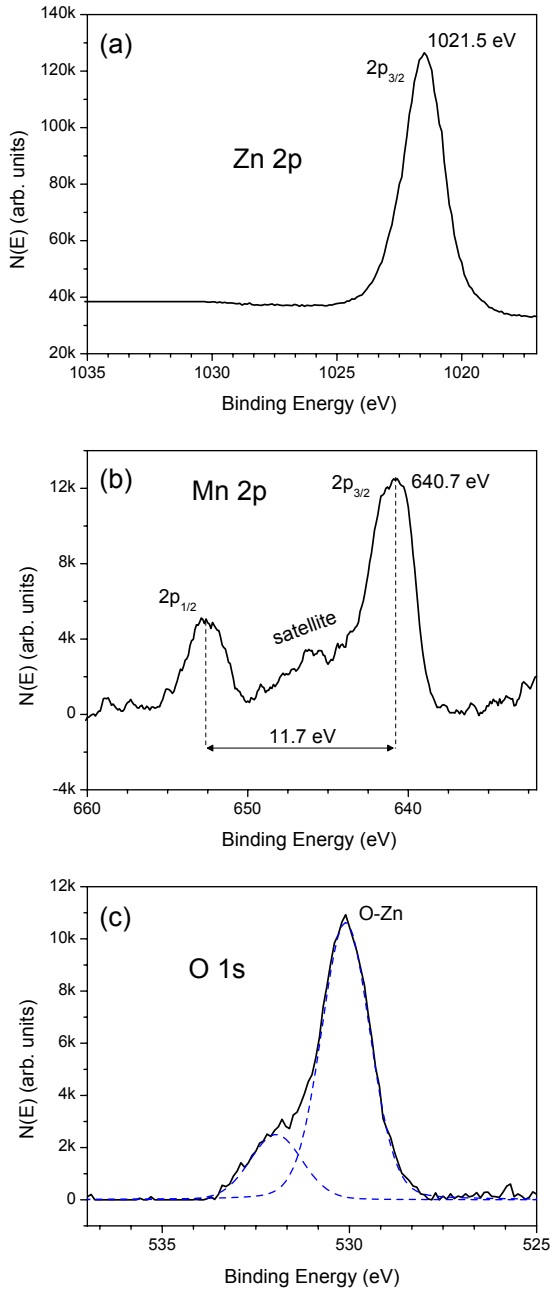

Figure 5-3. XPS spectra for ZnO:3%Mn film codoped with 0.01%Sn. (a) Zn 2p3/2 spectrum, (b) Mn 2p spectrum, and (c) O 1s spectrum. The film was sputtered in Ar for 4 min. and charge corrected to the O 1s peak.

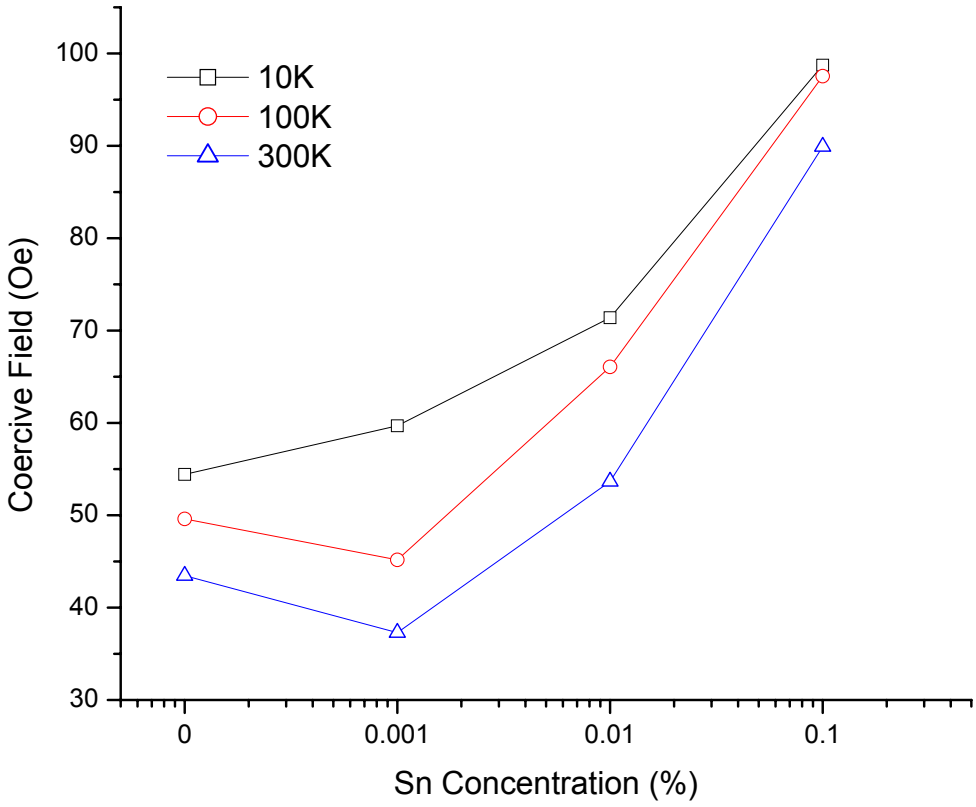

Figure 5-4. Plot showing the dependence of the coercive field on Sn concentration at different SQUID measurement temperatures.

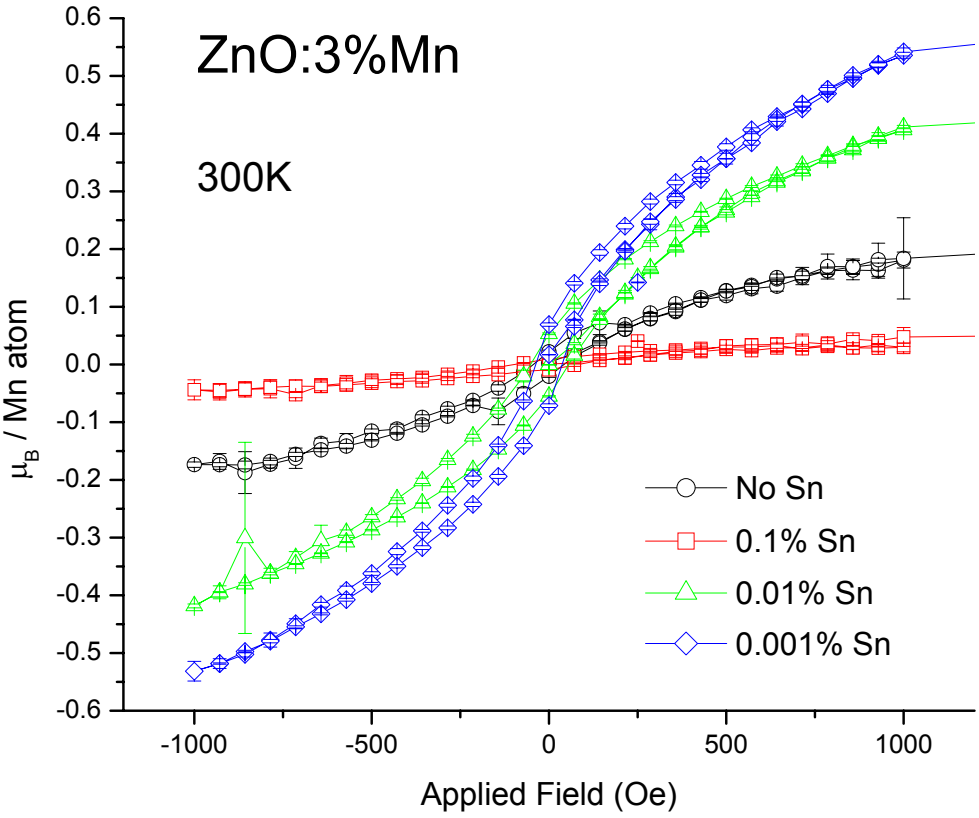

Figure 5-5. Magnetization measured at 300K for epitaxial ZnO:3%Mn films that are codoped with 0.001% Sn, 0.01%Sn, 0.1% Sn, and no Sn. There appears to be an inverse correlation of the Sn content with the saturation magnetization.

CHAPTER 6
PROPERTIES OF ZnO CODOPED WITH Mn AND P

6.1 Introduction

In the previous chapter, the magnetization dependence on carrier concentration was investigated using Sn as a donor dopant. The magnetization had an inverse correlation with electron density, suggesting that higher magnetization was favored as the Fermi level moved down in the bandgap. If the magnetization decreases with electron concentration, it might be expected that doping with holes will increase the magnetization. This chapter investigates the magnetic properties of Mn-doped ZnO codoped with P, a known p-type dopant in ZnO.

Superconducting Quantum Interference Device (SQUID) magnetometry measurements indicate that the films are ferromagnetic with an inverse correlation between magnetization and electron density as controlled by P doping. In particular, under conditions where the acceptor dopants are activated, leading to a decrease in free electron density, magnetization is enhanced. The result is consistent with hole-mediated ferromagnetism in Mn-doped ZnO, in which bound acceptors mediate the ferromagnetic ordering. Increasing the electron density decreases the acceptor concentration, thus quenching the ferromagnetic exchange. This result is important in understanding ferromagnetism in transition metal doped semiconductors for spintronic devices.

6.2 Experimental

Epitaxial Mn, P doped ZnO films were grown by conventional pulsed-laser deposition. Laser ablation targets were prepared from high purity powders of ZnO (99.999%), with MnO_2(99.999%) and P_2O_5 (99.95%) serving as the doping agents. The pressed targets were sintered at 1000C for 12 hr in air. The targets were fabricated with a nominal composition of 3 at.% Mn and 2 at.% P. A Lambda Physik KrF excimer laser was used as the ablation source. The laser energy density was 1-3 J/cm^2 with a laser repetition rate of 1Hz and target-to-substrate distance of 6 cm. The growth chamber exhibits a base

pressure of 10^{-5} Torr. Films were deposited onto single crystal, c-plane oriented sapphire substrates. The growth temperature was 400°C. An oxygen pressure of 20 mTorr was used for all film growth experiments. Film thicknesses were approximately 300 to 400 nm. X-ray diffraction was used to determine the crystallinity and secondary phase formation. SQUID magnetometry was used to characterize the ferromagnetic behavior of the doped films. The impurity concentrations were measured by EDS and determined to be within 10% of the nominal concentrations.

6.3 Results and Discussion

The phase stability and solid solubility of Mn in the ZnO films were investigated before and after annealing for films with P codoping. Figure 6-1 shows the x-ray diffraction scans for films deposited under the given growth conditions. In all cases, the dominant film peaks correspond to c-axis perpendicular ZnO. Note that, for these films, segregation of the Mn_3O_4 phase is not observed in the diffraction data. As mentioned earlier, the Mn_3O_4 phase is ferromagnetic with a Curie temperature less than 50 K. Previous reports from Fukumura et al. indicated that epitaxial ZnO films with a Mn concentration as high as 35% could be achieved while maintaining the wurtzite structure using pulsed laser deposition [37]. Upon annealing, a shift in the d-spacing for the ZnO is observed. This may indicate a segregation of either P or Mn in the films with thermal processing.

Figure 6-2 shows high-resolution ω-rocking curves taken around the ZnO (002) on a separate but similarly grown film. The similar shift in d-spacing appears after annealing. The scans were taken using a $\frac{1}{2}^\circ$ divergence slit over the x-ray source and a 1mm brass slit over the detector optics. The FWHM before and after annealing barely changes, suggesting the crystallinity does not change sufficiently with the anneal. Furthermore, in-plane alignment is measured with Φ-scans that show the six-fold symmetry of the ZnO wurtzite structure and confirm epitaxial registry with the substrate. The surface roughness of the film slightly decreases as measured by tapping-mode Atomic force microscopy

(AFM) (Figure 6-3). The grain structure has also notably coalesced and coarsened into larger grains.

Defect chemistry calculations for Mn-doped ZnO indicate that Mn^{+2} forms a donor level 2.0 eV below the conduction band edge [108]. This deep donor state with Mn substitution on the Zn site in ZnO has no direct effect on the electron concentration at room temperature. However, defect chemistry calculations also indicate a reduction in Zn interstitials with Mn doping. Zn interstitials are generally accepted as the primary shallow donor defects in nominally undoped ZnO. This will yield an increase in resistivity for Mn-doped films as compared to undoped material [108–110]. The Mn-doped ZnO films with no P exhibit a resistivity on the order of 10^2 Ω-cm with a carrier density of mid-$10^{16}/cm^3$. This carrier density is substantially lower than that seen for undoped epitaxial films, and is consistent with the reduction of shallow donors. Limited results on the doping behavior of P in ZnO indicate that it introduces a donor state for as-deposited films, an acceptor state when annealed.

The behavior of phosphorus in ZnO epitaxial films both as-deposited and upon annealing has been reported in detail elsewhere [119]. For the as-deposited films, the inclusion of phosphorus yields a significant increase in electron density, resulting in ZnO that is highly conductive and n-type. The shallow donor behavior in the as-deposited films is inconsistent with P substitution on the O site, and presumably originates from either substitution on the Zn site or the formation of a phosphorus-bearing complex. Previous work has shown that the defect-related carrier density in nominally undoped ZnO can be reduced via high temperature annealing in oxygen or air. In the case of undoped material, the reduction in donor density is presumed due to either a reduction in oxygen vacancies, Zn interstitials, or perhaps out-diffusion of hydrogen that is incorporated in the ZnO lattice during synthesis. In order to reduce electron density annealing in oxygen can be performed. Figure 6-4 shows the resistivity of films annealed at various temperatures. Note that the resistivity of the as-deposited phosphorus doped films is significantly lower

than that for the nominally undoped film. For as-deposited films, a shallow donor state dominates transport. As the films are annealed at increasing temperatures, the resistivity of the phosphorus-doped films increases rapidly. This is particularly evident for films subjected to annealing temperatures of 600°C or higher. When annealed at 700°C, the phosphorus doped ZnO films become semi-insulating with a resistivity approaching 10^4 Ω-cm. The conversion of transport behavior from highly conducting to semi-insulting with annealing should be attributed to at least two factors. First, the defect associated with the shallow donor state in as-deposited films appears to be relatively unstable. This would explain the increase in resistivity, but would alone predict a saturation of resistivity at the value given by the undoped material. The dependence of post-annealed resistivity on phosphorus content suggests that a deep level associated with phosphorus dopant is present. This is, in fact, consistent with the expected results that P substitution on the oxygen site yields a deep acceptor. Figure 6-4 also shows the carrier concentration for P-doped films. For all of the data shown in Fig. 6-4, the Hall sign was negative, indicating n-type material. Both carrier density and Hall mobility data for some annealed samples are absent in the plots. From the measurements yielding unambiguous Hall voltage, both the carrier density and mobility in phosphorus-doped films are observed to decrease with annealing. This is consistent with a reduction in the shallow donor state density and activation of a deep (acceptor) level in the gap.

Figure 6-5 shows the longitudinal (ρ_{xx}) and transverse Hall (ρ_{xy}) resistivity measured for a ZnO film doped with 3%Mn and 2%P at room temperature. The film was measured inside a Quantum Design Physical Property Measurement System (PPMS) modified with an external high-impedance Hall effect set-up from Keithley electronics. The film was measured in the Van der Pauw configuration with four indium contacts soldered to the corners of a square sample. The as deposited film is n-type with a carrier concentration of 2.8x10^{15} cm^{-3} and mobility of 0.56 $cm^2v^{-1}s^{-1}$. The ρ_{xx} in zero-field is 3,975 Ω-cm. There is a small negative magneto-resistance (MR) that reaches a value of about -0.35% at 7

Tesla. This small negative MR is also seen in undoped ZnO films at room temperature. The resistivity is a strong function of temperature and quickly becomes too resistive, $>10^5$ Ω-cm, to measure at lower temperatures. After annealing the sample for 60min in a tube furnace at 600° in 1atm O_2, the sample resistance was measured to be $>10^9\Omega$, which was too high to measure accurately with practical settling times.

Phosphorus is believed to create acceptor states after being thermally activated by annealing [119]. This requires the substitution of P^{-3} onto an O^{-2} lattice site to form the acceptor state. However, phosphorus exists in a variety of valence states, including +3, +5, and -3. To investigate the P incorporation into the film, XPS was used to investigate the charge state of the P ion. Figure 6-6 shows the XPS spectra for a ZnO:3%Mn, 2%P film before and after annealing. There is a broad structure between 128 and 132 eV, and then another peak centered around 133.6 eV. The P^{+5} valence state in P_2O_5 has a binding energy of 135.6 eV [120]. The the P^{-3} ion of Zn_3P_2 has a lower binding energy of 128.7 eV [121]. Note that pure phosphorus has a binding energy of 130.5eV [121]. Therefore, the higher binding energy peak of Figure 6-6 is likely related to the +5 valence. The broad structure at lower energy could be the existence of P^{-3} bonded to Zn cations. Therefore, the data suggests a coexistence of phosphorus charge states. There does not appear to be a significant shift in the binding energies after annealing.

Before annealing, the binding energy of the Mn $2p_{3/2}$ peak is 641 eV and there is a definite satellite structure at higher energy. The spectrum is consistent with Mn in the +2 valence state. After annealing, there is a slight peak shift to higher energy and the satellite structure significantly decreases. Langell et al. have reported similar behavior for single crystal MnO after annealing in oxygen, which was attributed to the formation of higher oxidized Mn phases [107]. It's probable that there is a mixture of Mn valence after annealing.

Optical absorption was measured using a Perkin-Elmer Lambda 800 UV/Vis dual-beam spectrometer. The absorbance of each sample was measured using unpolarized

light with wavelengths ranging between 200nm to 900nm. Figure 6-7 displays the optical transmission for the ZnO:3%Mn, 2%P film before and after annealing, along with an undoped ZnO reference sample. The undoped sample shows a sharp exciton absorption. This absorption is smeared out in the doped films and a broad absorption is seen around 3 eV in the doped films. There are two absorption peaks assigned to Mn^{2+} in ZnO at 2.95 and 3.26 eV from the $^6A_1(S) \rightarrow {}^4T_2(G)$ and $^6A_1(S) \rightarrow {}^4A_1, {}^4E(G)$ transitions, respectively [122]. These are spin-forbidden d-d transitions and should be weak. Therefore, the in-gap absorption around 3 eV is most likely attributed the Mn^{2+} $^6A_1(S) \rightarrow {}^4T_2(G)$ transition. Direct interband transitions follow the Tauc relation $\alpha h\nu = A_o(h\nu\text{-}Eg)^{\frac{1}{2}}$, where α is the absorption coefficient, $h\nu$ the photon energy, and A_o is a parameter associated with the transition probablility and refractive index. $(\alpha h\nu)^2$ vs. $h\nu$ is plotted in the inset of figure 6-7. Straight lines are fit through the linear regions of the plots to extract the band gap of each sample. The band gap widens with Mn-doping. Both the in-gap absorption and blue-shift have been reported previously in $Zn_{1-x}Mn_xO$ films [37]. After annealing, the band gap decreases slightly. This could be caused by Mn segregating out of the lattice at high temperature, which would be consistent with the peak shift in the XRD data and the disappearance of the satellite peak in XPS.

The magnetic properties of the films were measured using a Quantum Design SQUID magnetometer. The diamagnetic responses of the substrate and host semiconductor were subtracted from the magnetization plots. The primary focus of the measurements was to determine how the magnetic properties of the films changed as a function of electron density as controlled by P doping. Samples that showed minimal amounts of Mn_3O_4 precipitation via x-ray diffraction were used for the SQUID measurements. Figure 6-8 shows the room temperature magnetization as a function of applied magnetic field for epitaxial ZnO:3%Mn films both without and with P co-doping. For the Mn-doped film with no P, saturation in the magnetization is observed, but with little evidence for hysteresis in the M vs. H curves. The as-deposited ZnO film doped with both Mn and P

showed a reduction in magnetization/Mn ion. This is consistent with the proposed models for Mn-doped ZnO, where ferromagnetic ordering is not favored by electron doping. Most interesting is the saturation magnetization behavior as the P doped samples are annealed. As noted earlier, increasing P concentration in as deposited films initially increases electron density and conductivity. Figure 6-8 shows the room temperature magnetization versus field behavior for the ZnO samples containing 3%Mn and 2 %P annealed in oxygen. Magnetization is given as the magnetic moment/Mn dopant ion. Initially, there is a decrease in magnetization with P doping. However, with annealing, there is an inverse correlation between the electron carrier concentration and saturation magnetization. Similar results are seen at 10 K as shown in Figure 6-9. Initially, as the electron density increases with P doping, the magnetization decreases. The inverse correlation of saturation magnetization with electron density is interesting and provides some insight into the mechanism for ferromagnetism in Mn-doped ZnO. Overlap of the Mn d-states with the valence band suggests that holes are necessary in order to induce ferromagnetic order. For semi-insulating films to exhibit ferromagnetism, the bound magnetic polaron model provides a mechanism whereby holes that are localized at or near the Mn ions are responsible for mediating ferromagnetism. However, the most important observation is that the activation of acceptor states for hole formation is necessary in order to achieve ferromagnetism. The holes may be delocalized, but with low mobility, thus yielding low conductivity. In this case, the carrier mediated mechanism may suffice without the need of invoking bound polarons as inherent to the ferromagnetic ordering. In either case, the addition of electrons to the system will move the Fermi energy level up in the band gap, resulting in a decrease in hole density and a reduction in magnetization. This appears consistent with early work on trivalent doped (Zn,Mn)O where no ferromagnetism was observed for heavily n-type films. It may also explain the discrepancy from other studies of Mn-doped ZnO films in which the intrinsic defect-mediated donor states are high in density. It should be noted that the amount of magnetization in the material remains

relatively low at all temperatures as seen in the temperature dependent magnetization data in figure 6-10. It is important to note the need to maintain a Mn concentration low enough to avoid Mn-Mn antiferromagnetic interactions, which are likely to dominate high Mn doped ZnO films.

The results of this study are consistent with previous studies on the carrier type dependence in Co- and Mn-doped ZnO nanocrystalline films [32, 49]. In that case, ferromagnetism was observed in Mn-doped ZnO nanocrystals only when nitrogen, a group V acceptor dopant, was introduced during the synthesis process. In contrast, no ferromagnetism was observed in Co-doped ZnO nanocrystals when processed with nitrogen. Based on this and other properties, the authors conclude that ferromagnetism in ZnO is closely tied to the charge transfer electronic structure of the transition metal dopant. For Mn, ferromagnetism is induced when the holes from the acceptor ion delocalize onto Mn^{2+}. Again, our results are consistent with this conclusion.

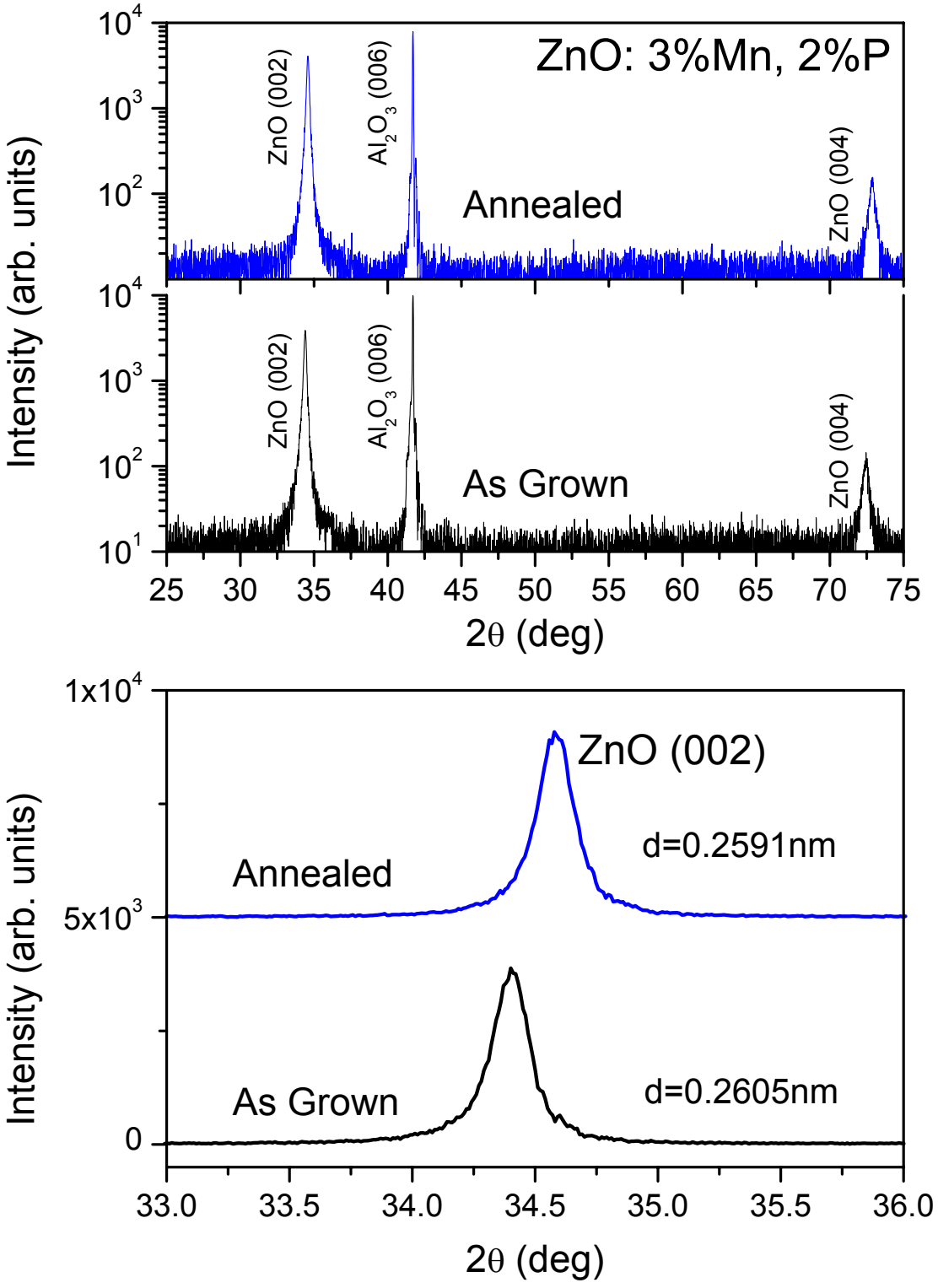

Figure 6-1. X-ray diffraction of ZnO films codoped with Mn and P both before and after annealing. The target was ZnO doped with 3% Mn and 2%P

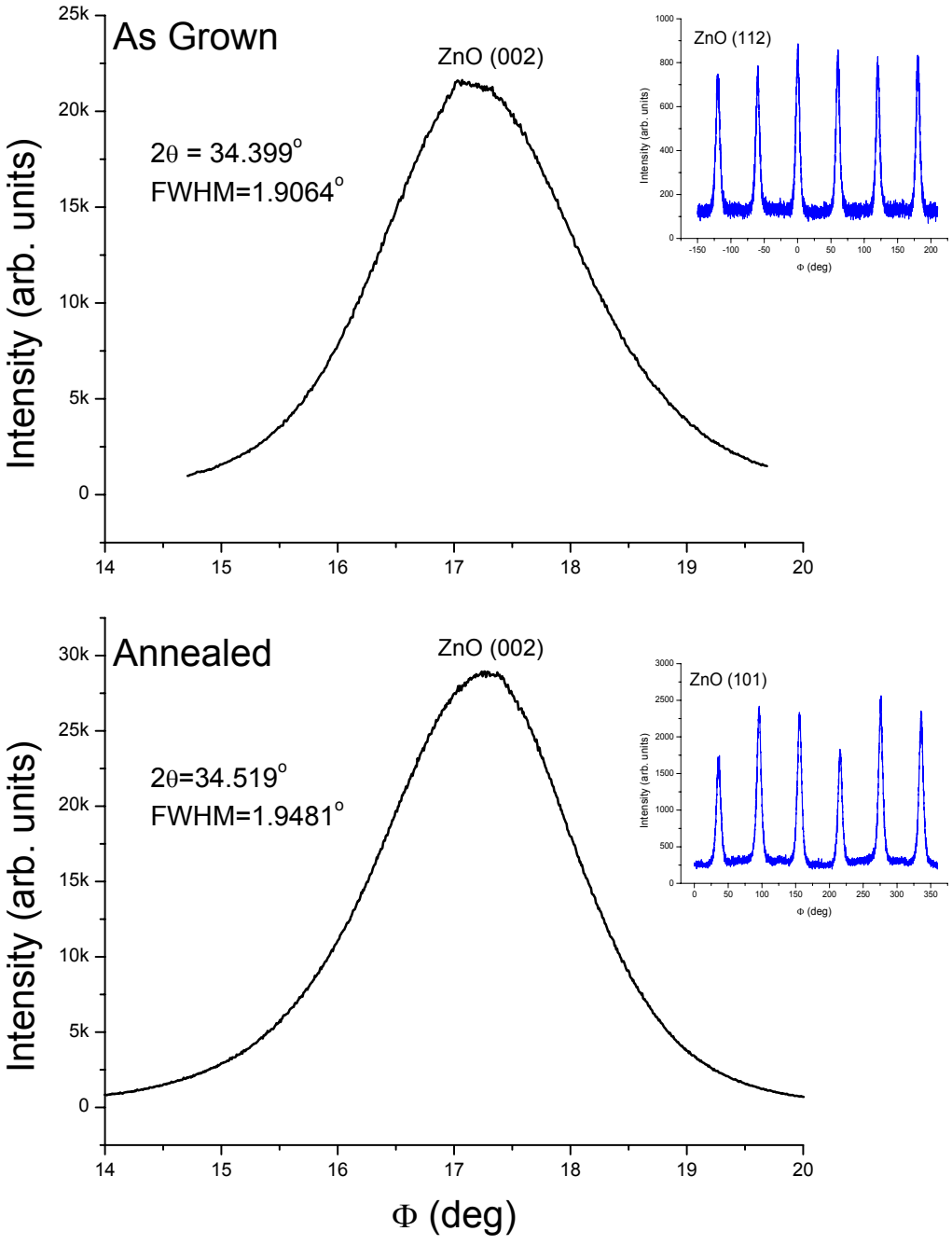

Figure 6-2. High-resolution ω-rocking curves on ZnO films codoped with Mn and P before and after annealing. The scans are taken around the ZnO(002) reflection. The insets show Φ-scans around the indicated peaks, showing the film's in-plane alignment with the substrate.

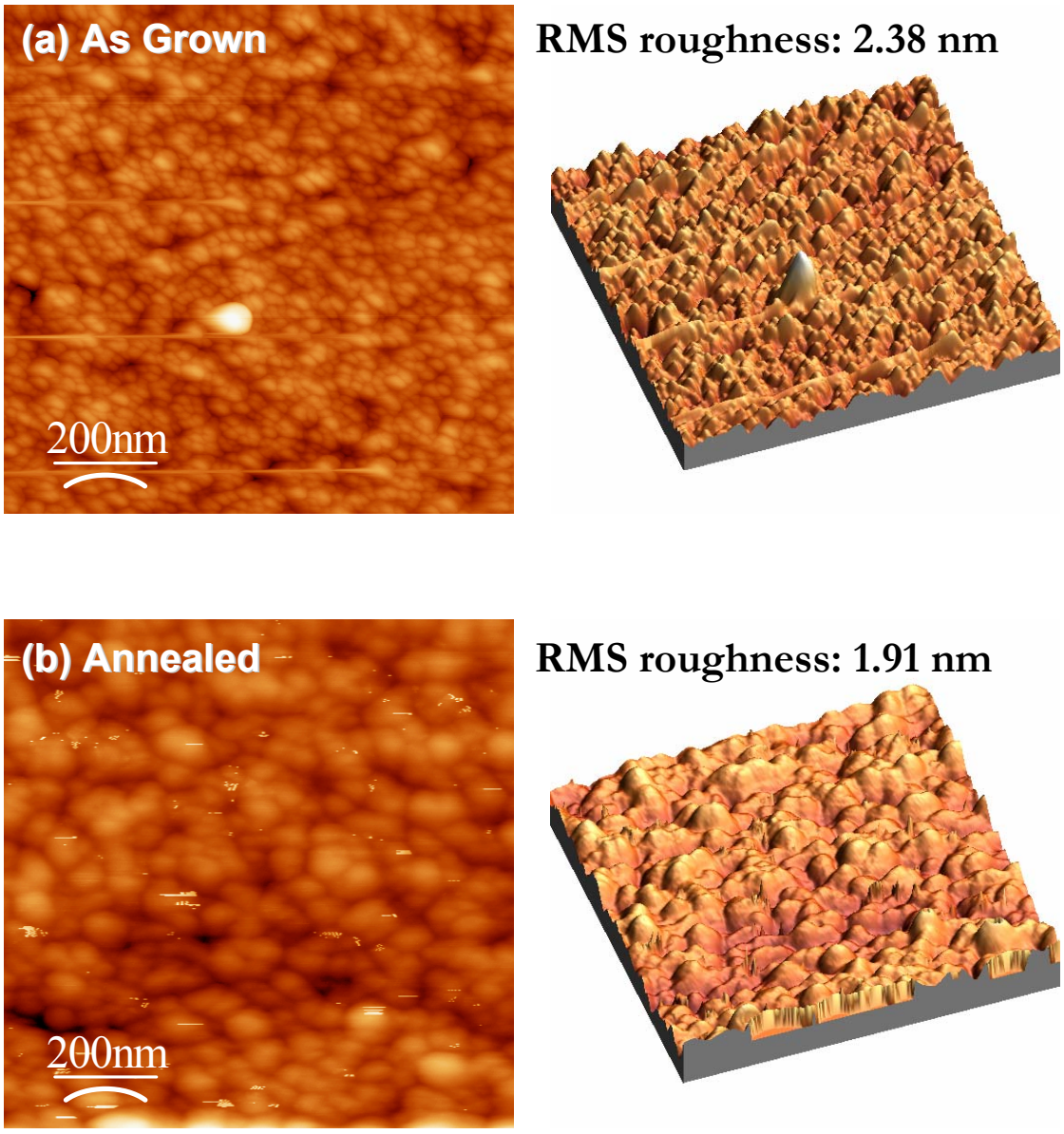

Figure 6-3. AFM scans on epitaxial ZnO:3%Mn, 2%P films before and after annealing. Scans were taken in tapping-mode. The surface roughness decreased and the grains have coalesced into larger grains with annealing. (AFM imaging software provided by [123]).

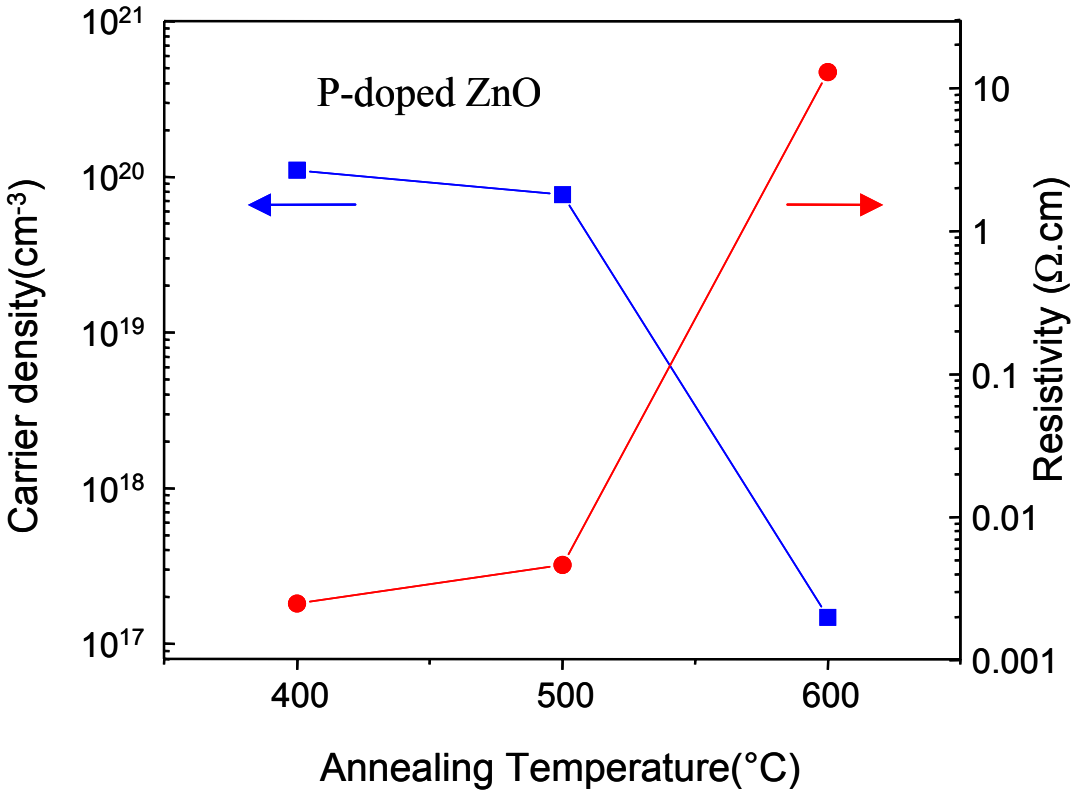

Figure 6-4. Resistivity and carrier concentration behavior of P-doped ZnO films both as-deposited and annealed in oxygen. The data shown is for 1 at.%P doped ZnO

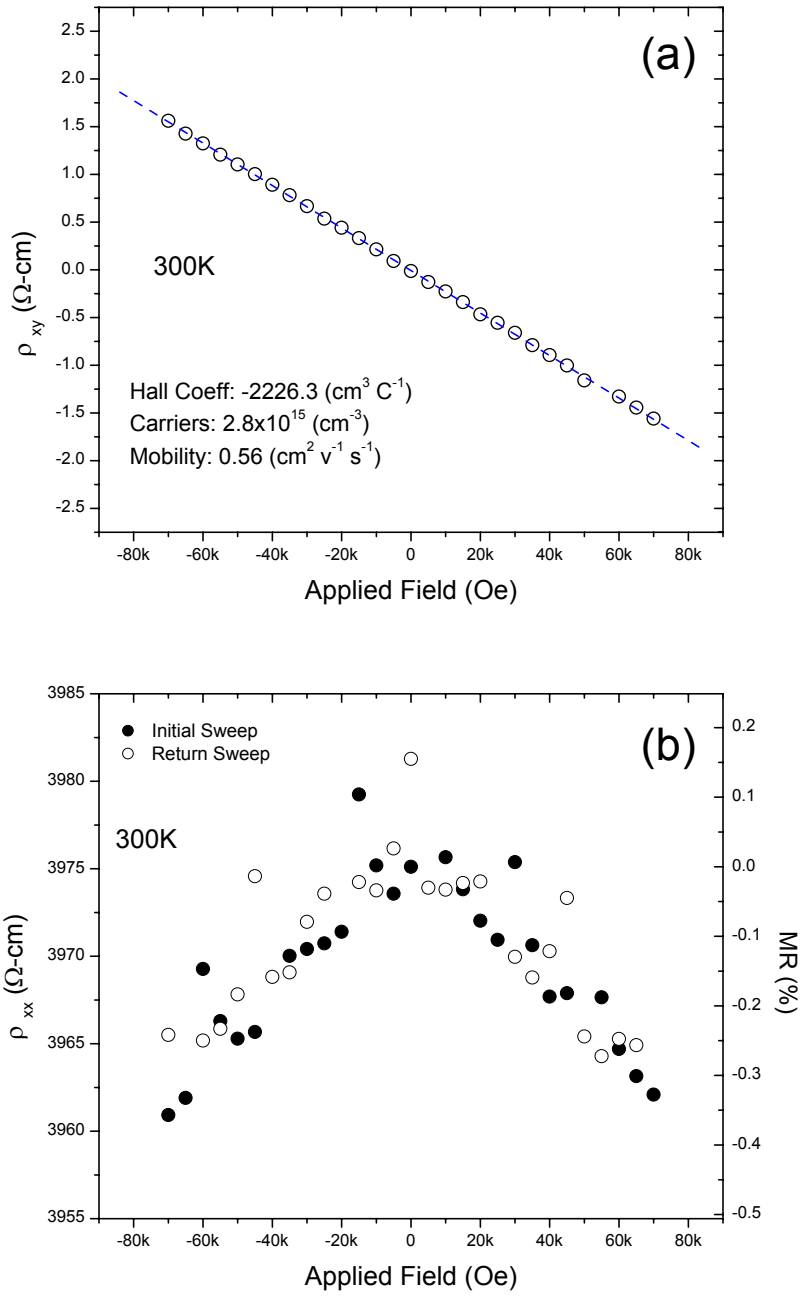

Figure 6-5. Transport data for the as-deposited ZnO:3%Mn, 2%P film at 300K. (a) Transverse Hall (ρ_{xy}) and (b) longitudinal (ρ_{xx}) resistivity.

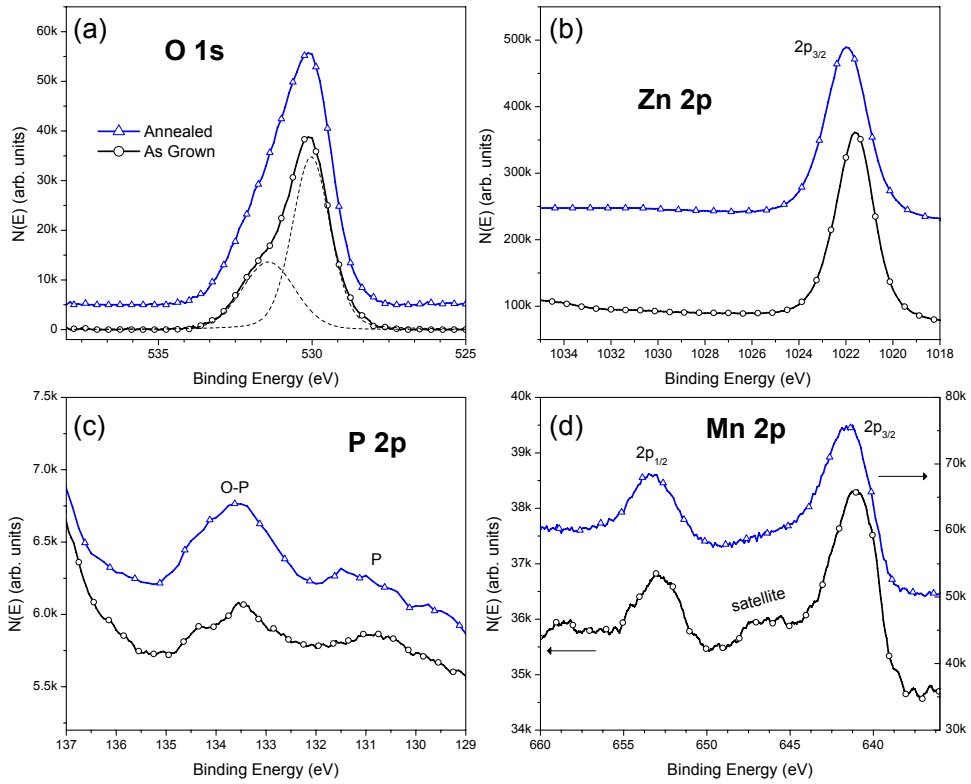

Figure 6-6. XPS spectra for ZnO:3%Mn film codoped with 2% P. (a) O 1s spectrum, (b) Zn $2p_{\frac{3}{2}}$ spectrum, (c) P 2p spectrum, (d) Mn 2p spectrum. The data was charge corrected to the O 1s peak at 530.1 eV.

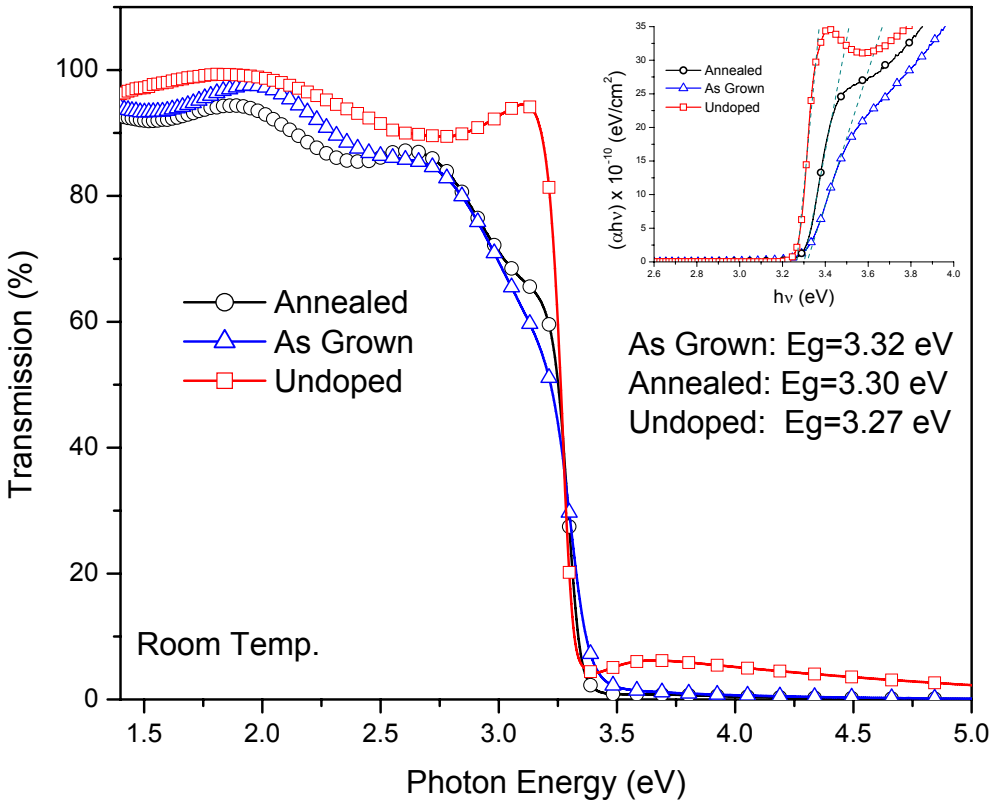

Figure 6-7. Room temperature optical transmission for ZnO:3%Mn, 2%P films both as-deposited and after annealing at 600°C in oxygen. Data for an undoped ZnO film is also included. Inset: Tauc plots with linear fits to determine the optical band-gap for each film.

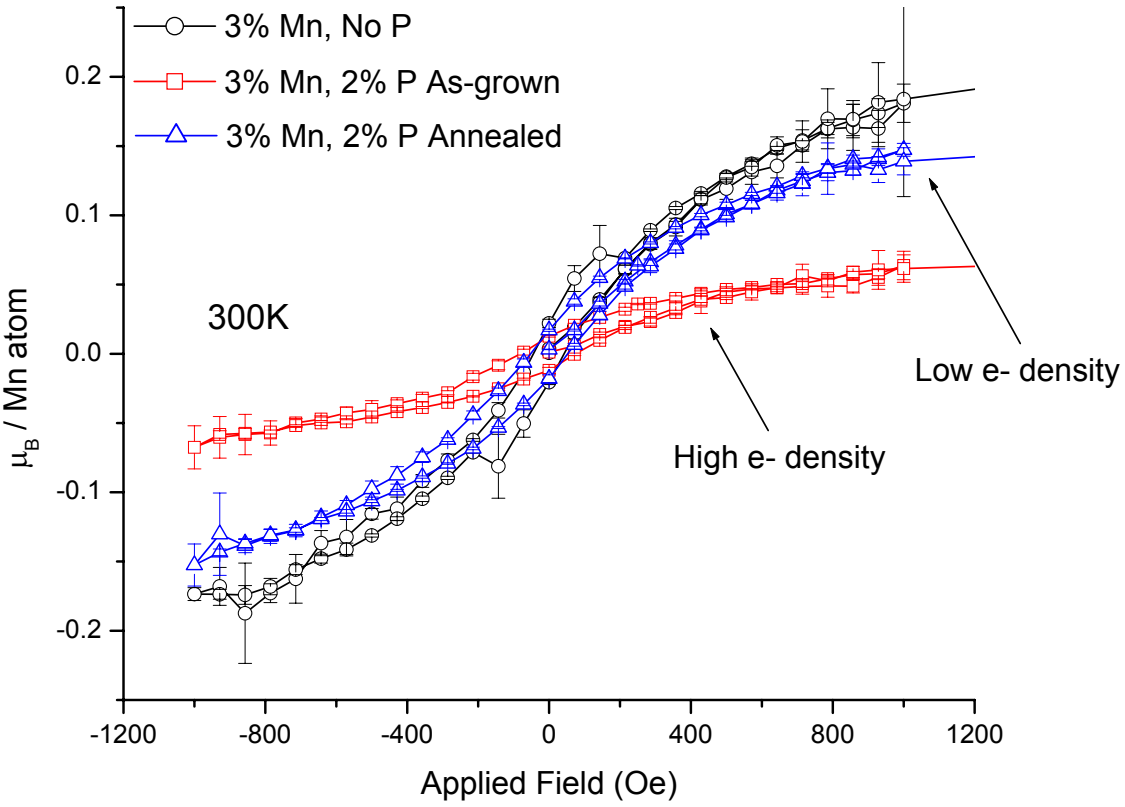

Figure 6-8. Room temperature SQUID measurements for epitaxial ZnO:3%Mn,2%P films before and after anneal. Also shown is a ZnO:3%Mn film with no P.

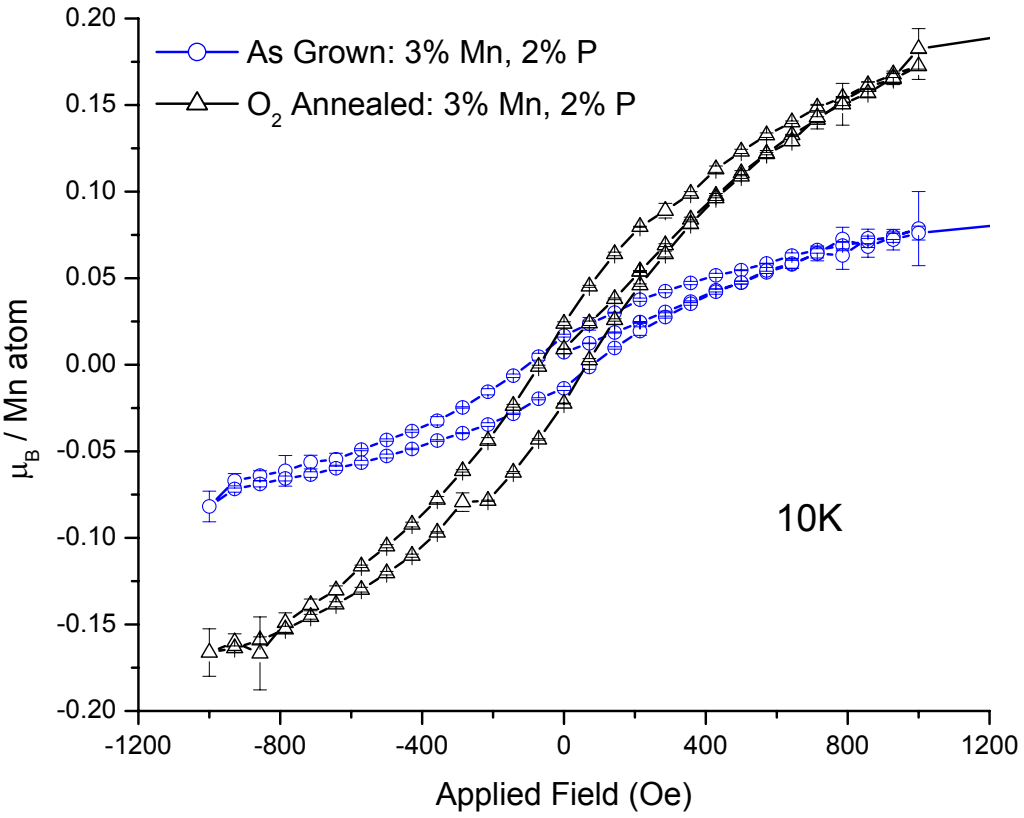

Figure 6-9. SQUID measurement at 10K for epitaxial ZnO:3%Mn, 2%P films before and after annealing.

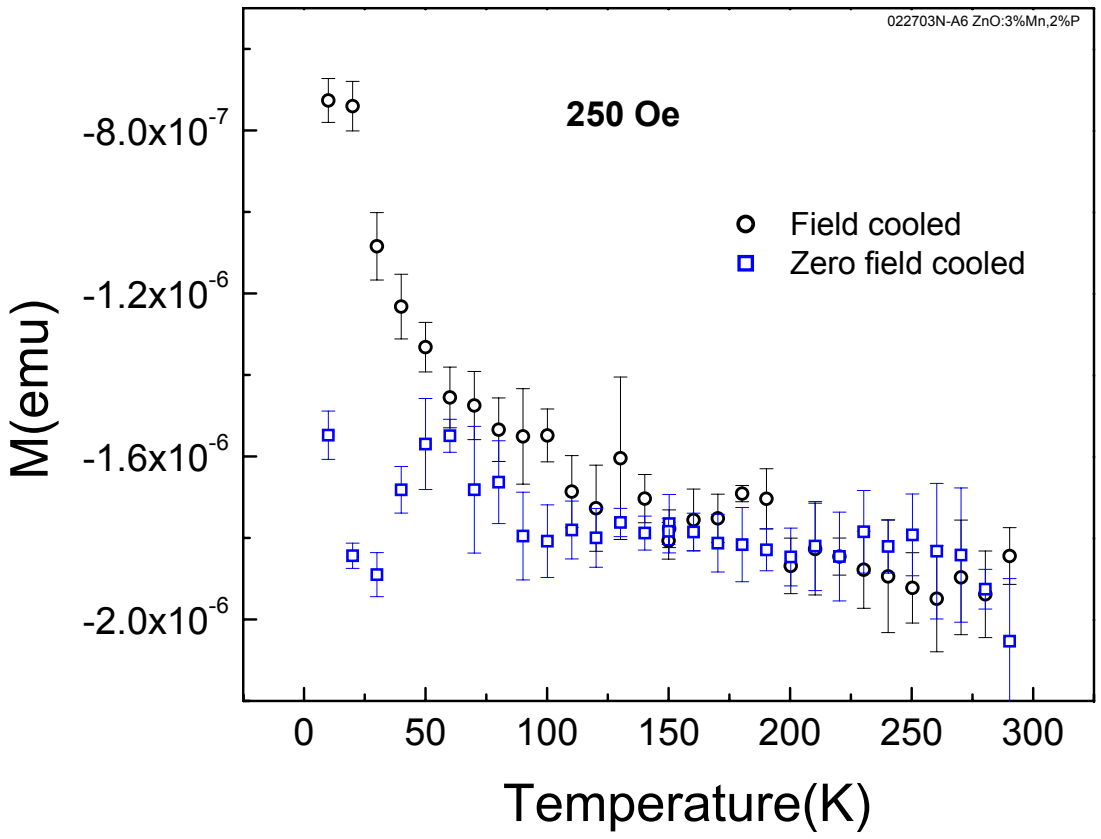

Figure 6-10. Field-cooled and zero field-cooled magnetization measurements for a ZnO:3%Mn, 2%P film annealed at 600C in O_2.

CHAPTER 7
PROPERTIES OF COBALT-DOPED ZnO

7.1 Introduction

The two previous chapters investigated the properties of Mn-doped ZnO as a potential material for spintronic applications. In this chapter, cobalt is investigated as a magnetic dopant in ZnO. The magnetic and magneto-transport behavior of doped films were examined. Cobalt concentration is varied over a wide range, from 0 to 30 at.%Co. A combination of x-ray diffraction, optical absorption, and transmission electron microscopy were used to examine the solubility of cobalt in the ZnO lattice and phase segregation of cobalt metal.

Films deposited at 400°C in vacuum were found to be ferromagnetic, while films deposited in oxygen or at higher temperatures were found to be nonmagnetic. Segregation of cobalt metal occurs in films doped with 15 at.% or greater Co concentrations when deposited in vacuum, and the precipitates are found to be oriented within the lattice. The segregation can be suppressed by depositing in higher base pressures, but the process is not fully reproducible. Peculiar MR is observed in the films and the MR changes as the carrier concentration crosses the metal-to-insulator transition.

7.2 Experimental

Cobalt-doped ZnO films were deposited via pulsed laser deposition (PLD) onto c-plane oriented sapphire substrates. The ablation targets were prepared through the solid-state reaction of mixed oxide powders. Appropriate amounts of ZnO (Alfa Aesar, Puratronic, 99.9995%) and Co_3O_4 (Alfa Aesar, Puratronic, 99.9985%) powders were ground and mixed in methanol, dried in air, pressed into pellets, and sintered at 1000°C for 12 hours in air. The targets were mixed to give proportions of $Zn_{1-x}Co_xO$ with x=0.00, 0.02, 0.05, 0.15, and 0.30. A KrF excimer laser (248nm wavelength) was used for target ablation using a repetition rate of 1Hz and a laser energy density of 1–3 J/cm^2. A temperature range of 400°C-600°C and oxygen pressures up to 2x10^{-5} Torr were used in

the experiments. The vacuum (base pressure) of the chamber was ∼7.0x10^{-6} Torr. Film thicknesses were 200–300nm as measured by mechanical profilometry.

7.3 Results and Discussion

7.3.1 Chemical Composition

Energy Dispersive Spectroscopy (EDS) was used to measure the percentage of cobalt in the films. Figure 7-1 shows the cobalt concentration in the film as a function of target composition for films deposited under different conditions. The cobalt concentration is generally larger in the films than the prepared targets. This likely occurs because Zn has a higher vapor pressure than Co, thus less Zn is incorporated into the film during deposition. The cobalt concentration is also higher with increased substrate temperature.

7.3.2 Structure and Phase Analysis

7.3.2.1 Films with precipitation

Crystal structure and phase analysis were characterized using X-ray diffraction (XRD) in Bragg-Brentano geometry. Figure 7-2 shows the θ-2θ x-ray diffraction patterns for a series of films grown at 400°C in vacuum (base pressure 7x10^{-6} Torr) with varying cobalt concentration. The primary peaks correspond to the wurtzite ZnO (002) indicating good texture with the c-plane of the sapphire substrate. As the cobalt concentration is increased above 10%, the appearance of a new peak begins to develop around a 2θ value of 44.4 degrees. The peak is small (only a few hundred counts above background) and does not correspond to any ZnO or substrate peaks. Both the small intensity and 2θ position make identification of the peak difficult using XRD as there are several cobalt containing phases with similar 2θ values of around 44.4 degrees, including the spinel family of cobalt oxides and cobalt metal. However, exact determination of the peak is critical since the presence of ferromagnetic cobalt metal could contribute to the magnetic signature of the films. The cubic and spinel cobalt oxides are antiferromagnetic, though some papers report that small nanocluster powders of cobalt oxides are ferromagnetic due to uncompensated

surface spins [124, 125]. Table 7-1 is a list of the possible phases with their respective 2θ diffraction values and magnetic character.

High resolution XRD and TEM were used to characterize the secondary phase observed in the powder XRD scans. Cross-sectional TEM was used to more precisely delineate the nature and location of the extra phase as shown in figure 7-3. Most of the precipitation occurs near the film/substrate interface in the form of small (∼5nm) particulates. However, for most of the film, the cobalt dopant appears to reside in the ZnO lattice without precipitation. Convergent beam TEM diffraction patterns of the film and nano-precipitates are shown in figure 7-4. The particles appear to be oriented with the lattice and have d-spacings of d_{002}= 0.20nm and d_{-210}=0.13nm. This is consistent with metallic cobalt and the particles are tentatively assigned as such. The peak intensity was too low to collect information using high-resolution XRD on the as grown film. However, after annealing the samples in hydrogen (4%H_2/Ar balance) at 500°C, the amount of cobalt increases at the expense of ZnO causing partial degradation of the film, and high-resolution XRD could be employed which is discussed in a later section. The change in microstructure at low annealing temperature suggests that the cobalt that is substitutional in the ZnO lattice is not stable at moderately high temperatures.

7.3.2.2 Films without precipitation

By modifying the growth conditions, the secondary phase can be suppressed. Figure 7-5(a) shows XRD scans for samples grown at 400°C at different pressure conditions. The cobalt phase forms at low base pressures. By depositing in higher base pressures ($>10^{-5}$ Torr) or adding a small amount of oxygen, the Co phase disappears from the XRD scans. It should be noted that the process is not fully repeatable. The cobalt phase is still present by XRD for some depositions but seems less probable at the higher base pressures. As a rough estimate, the phase is suppressed in 80–90% of the samples grown in higher base pressures. It is assumed the pressure at vacuum is composed mostly of water vapor.

Figure 7-5 also shows XRD scans for films deposited at 500°C and 600°C in vacuum. At 500°C the CoO phase begins to form along with the cobalt metal. At 600°C the cobalt metal phase disappears and the CoO phase becomes more prominent. Thermodynamically, CoO is the most stable phase at these temperatures and pressure. This can be seen from the thermodynamic predominance diagram for the cobalt oxides given in figure 7-6. Interestingly, one would expect the formation of Co_3O_4 at lower growth temperatures and not the metallic cobalt phase determined from TEM. This suggests the cobalt metal phase is stabilized by the ZnO lattice and not by thermodynamic considerations. This is consistent with the well oriented particles observed in TEM.

7.3.3 Optical Properties

7.3.3.1 Optical absorption

Evidence for Co substitution in the ZnO lattice can be inferred from optical absorption measurements. Figure 7-7 shows transmission data for Co-doped ZnO films that do not show precipitation by XRD. An undoped ZnO film is included as reference. Each film was normalized by dividing by its maximum observed transmission (T/Tmax) to compare the intensity of absorption peaks between films. Three adsorption peaks are apparent in the doped films. These peaks are characteristic d-d transition levels attributed to Co^{+2} occupying tetrahedral lattice positions, and indicate that cobalt is substituting as Co^{+2} on Zn lattice sites in the films [45, 126, 127]. The intensity of these absorptions in the doped films also increases with increased Co concentration suggesting most of the Co is soluble in the lattice. Specifically, the peaks located at energies of 1.9 eV (651nm), 2.0 eV (608nm), and 2.2 eV (564nm) correspond to the $^4A_2 \rightarrow {}^2E(G)$, $^4A_2 \rightarrow {}^4T_1(P)$, and $^4A_2 \rightarrow {}^2A_1(G)$, respectively [128].

The band-gap of the alloys was calculated by plotting $(\alpha h\nu)^2$ vs. $h\nu$ and extrapolating the linear portion of the plot to $(\alpha h\nu)^2 = 0$. The plots are given in figure 7-8. At low cobalt doping—the undoped film and the film doped with 2%Co—the absorption edge is well defined and can be fit reliably. The exciton peak is clearly visible in the undoped

film indicating good quality ZnO. However, as the cobalt doping is increased, a low energy absorption onset appears and the doping smears out the linear region giving it a more rounded shape. Linear fits to both the high and low energy regions are given in figure 7-8 as a function of cobalt concentration. The high energy slopes give a band-gap energy that linearly increases (blue-shifts) with nominal cobalt concentration. The low energy slopes give an energy that roughly remains constant around 2.8–2.9 eV.

Some reports in the literature observe a red-shift in the band gap energy as the cobalt concentration is increased [129–132]. The red-shift is typically attributed to the sp-d exchange between the ZnO band electrons and localized d-electrons associated with the doped Co^{+2} cations. The interaction leads to corrections in the energy bands; the conduction band is lowered and the valence band is raised causing the band gap to shrink [133].

On the other hand, other papers have reported a blue-shift in the band gap of ZnO with cobalt doping. Peng et al. reported a blue-shift in the band-gap of the material and a red-shift of the band tails, which is similar to our observations [134]. Yoo et al. also observed a blue-shift in Al and Co codoped ZnO films which were attributed to the Burnstein-Moss effect from an increase in the carrier concentration [135].

The blue-shift in the gap energy is probably not caused by the Burnstein-Moss effect in these films. In a heavily doped n-type semiconductor the Fermi level resides in the conduction band. The free electrons in the semiconductor fill the lowest states in the conduction band and the valence electrons can no longer be optically excited into these filled states. This results in an apparent increase in the onset of absorption and the gap shifts to higher energy [79]. This shift requires an increase in the electron density. However, there is no systematic increase in the carrier density of the measured films with additional cobalt.

As discussed earlier in Chapter 3, band tails can arise from perturbations in the band structure caused by impurities and disorder. States introduced by impurities overlap at

high concentrations and evolve into an impurity band. As seen in figure 7-8, the tails' intensity rises with increased cobalt. Therefore, the tails are most likely related to the increase of impurity states. Kittilstved and coworkers saw a large MCD peak at ~25,000 cm^{-1} (3.10 eV), which they assigned as a valence band-to-metal charge transfer (CT) transition in ZnCoO [32]. The level was approximately 2,600 cm^{-1} (0.322 eV) below the conduction band. The onset of absorption in figure 7-8 starts around 2.9 eV. This is below the value found by Kittilstved; however, their MCD peak had some breadth with the onset of the peak beginning ~23,000 cm^{-1} (2.85 eV), which is in good agreement with the absorption onset in figure 7-8. Therefore the low energy absorption onset is likely an electron transition from the valence band to the cobalt impurity states.

7.3.3.2 Photoluminescence

Photoluminescence (PL) was performed on the series of films grown at 400°C in vacuum. The PL was used primarily to verify the band-gap shift found in the optical absorption data. Figure 7-9 shows the PL spectra taken at room temperature. For the undoped film, a broad luminescence band is visible across most of the spectrum. Broad green-yellow bands are typically attributed to defects in ZnO, including oxygen vacancies [136]. The films are grown in low oxygen pressures and are non-stoichiometric which could give rise to the broad defect bands. A more detailed study of the low temperature PL properties would have to be done to say more about the bands. The dip in the intensity at ~517 nm is an artifact due to the blaze angle of the diffraction grating and not from the film properties. The band-edge is visible in the undoped and 2%Co doped films, but is quenched with higher cobalt doping. Higher resolution scans around the band-edge emissions of the undoped and 2%Co samples are shown in the inset of figure 7-9. The band-edge is blue-shifted from 3.25 eV to 3.31 eV in the 2%Co sample. This is consistent with the band-gap determined from optical absorption.

7.3.4 Magnetic Characterization

The volume magnetization of the films was measured using a Quantum Design superconducting quantum interference device (SQUID) magnetometer. Before measuring, the backs and sides of the samples were etched in nitric acid (50% nitric/ 50% deionized water) to remove excess silver paint and contaminants that could contribute a spurious magnetic signal as measured by the SQUID. Each film surface was first coated in photoresist and baked for 20min. at 50°C to help protect the film during etching and then floated on top of the nitric acid for 3 min. The photoresist was removed by rinsing in acetone.

The SQUID magnetization data is normalized using two common methods: normalizing by the film volume and normalizing by the number of bohr magnetons (μ_B) per Co atom. To convert the raw magnetization data from emu to μ_B/Co, all the cobalt atoms are assumed to substitute on Zn sites and a cation density of 4.18x10^{22} cm^{-3} is used for the conversion. The data is normalized using the cobalt concentrations from the EDS data given in figure 7-1.

Magnetization data for a series of films grown at 400°C in vacuum with different amounts of cobalt are displayed in figure 7-10. These films do not show cobalt-induced secondary phases by XRD. The films with a nominal concentration of 2% and 5% cobalt are ferromagnetic with hysteresis at 10K; however, the saturation magnetization gradually decreases with increased temperature and the hysteresis disappears. The film with 30%Co shows ferromagnetism up to 300K with a clear hysteretic shape. The sample has a room temperature magnetization approaching 0.08 μ_B/Co.

The magnetization data for films with and without secondary phase formation are compared in figure 7-11. As stated previously, the main difference between the films is the growth pressure used during deposition. The 30%Co film with the secondary phase has a larger magnetization than the film without. This would be expected if the secondary phase is cobalt metal. Notice the film deposited in oxygen shows very little magnetization.

This is also true for films that were grown in higher oxygen pressures (up to 20mTorr pO_2). The film with cobalt precipitation has a room temperature magnetization that saturates ~0.22 μ_B/Co at higher fields (>1 Tesla). The film without precipitation has a room temperature magnetization approaching 0.08 μ_B/Co. Both these values are well below the 3μ_B moment of the (d^7) high-spin configuration of Co^{+2}. They are also below the 1.72 μ_B/Co value of pure metallic cobalt. However, the values are in good agreement with other values reported in the literature for ZnCoO (0.08 to 0.4 uμ_B/Co) [48, 67, 137]. Recent LSDA+U calculations predict that the nearest-neighbor exchange couplings of cobalt in ZnO should be antiferromagnetic, irrespective of the geometrical nearest-neighbor arrangement [138]. Therefore at high cobalt concentrations, where statistically a greater number of nearest-neighbors will develop, one would expect a lower moment per Co than that given by lower Co doping concentrations. However, this is not what is observed in the present case.

7.3.5 Electrical Transport

7.3.5.1 Hall effect

The origins of ferromagnetism in cobalt-doped ZnO are still not fully understood. Whether the ferromagnetism is truly intrinsic as a result from the interaction of carriers with magnetic dopants, or if the ferromagnetism is extrinsic and arises from secondary phases or nanoclusters is an important consideration. The usefulness of a DMS rests on its ability to produce and manipulate spin polarized currents. If the ferromagnetism in these materials is solely localized in secondary phases and does not polarize the free carriers, then the DMS is of limited utility in spintronic device applications.

A DMS that contains an asymmetry in the carrier spin-density (a spin-polarized current) should exhibit an anomalous Hall effect (AHE) in transport measurements. For ferromagnetic materials the Hall equation is given by:

ρ_{xy} = RoB +RsM

where ρ_{xy} is the Hall resistivity, Ro is the ordinary Hall coefficient, Rs the anomalous Hall coefficient, and B and M are the magnetic flux and magnetic field vectors normal to the film surface. Ro is caused by the Lorentz force acting on moving charge carriers. The anomalous term, Rs, is usually ascribed to spin-dependent scattering of carriers at local atomic moments. Carriers of opposite spin are scattered in different directions at each moment. This modifies the charge accumulation at each end of the sample. At higher fields, the magnetization, M, will saturate causing the anomalous Hall component, RsM, to become constant. At this point, changes in the Hall curve are determined by the ordinary component and should be linear in field. The ordinary Hall coefficient can be extracted from the high-field, linear region and the electrical properties of the material determined.

Variable-field Hall effect measurements were performed on Hall bridge patterned films. The films were patterned during growth by depositing through a stainless steel shadow mask. Electrical contacts were soldered to the sample using indium metal. The films were mounted inside a Quantum Design Physical Property Measurement System (PPMS) to control the ambient temperature and applied magnetic field, and the electrical data was collected using a Keithley high-impedance Hall effect system (the components of this set-up are described in the appendix).

Both the transverse (ρ_{xy}) and longitudinal (ρ_{xx}) resistivity were measured by applying a longitudinal current (I_{xx}). Measured values of ρ_{xy} will have a contribution from ρ_{xx} if the voltage leads are slightly misaligned. Therefore the resistance data was geometrically and field averaged to remove any asymmetries and to account for thermally induced voltages. Since ρ_{xy} is antisymmetric with applied magnetic field, the data was averaged by $\rho_{xy,odd}(H) = \frac{1}{2}[\rho_{xy}(+H) - \rho_{xy}(-H)]$ to help remove any parts of the signal from the longitudinal component [139]. Conversely, ρ_{xx} is symmetric with respect to applied magnetic field and can be averaged using $\rho_{xx,even}(H) = \frac{1}{2}[\rho_{xx}(+H) + \rho_{xx}(-H)]$.

For the ZnO films doped with 30% cobalt, an anomalous Hall signature is observed in samples grown at 400°C and in vacuum as given in Figure 7-12. Included in the figure is a

film with and without cobalt precipitation. Both films show AHE at room temperatures, but the effect is much more pronounced in the film with cobalt precipitation. Derivatives are shown in the insets of each graph to show the change of slope created by the AHE. Interestingly, there is no evidence of hysteresis in either Hall curve within the resolution of the instrumentation. A weak AHE is also observed in the film doped with 15%Co. For films doped with less than 15% Co, no AHE is observed at the chosen growth conditions.

Although the AHE is typically attributed to scattering of carriers by local magnetic moments, it has been suggested that nonmagnetic materials with ferromagnetic precipitates can also exhibit an AHE. This has been observed in Co-doped TiO_2 films by Shinde et al. [140]. They report an AHE in superparamagnetic, highly reduced cobalt-doped rutile TiO_2 films that contain cobalt metal clustering close to the film/substrate interface. Superparamagnetic granular metal composites are also known to show anomalous Hall behavior [141, 142]. While the larger AHE is suspect in the films with precipitation, the origin of the AHE in the non-precipitated films is not obvious. The AHE could arise from the cobalt atoms that are substitutional in the ZnO lattice or possibly from small nanoparticles of cobalt metal not observable with XRD. Evidence for a true AHE from substitutional cobalt atoms is inferred from annealing experiments, which is discussed shortly.

It is important to examine the possibility of cobalt particles as the source of ferromagnetism. The films with 30%Co grown at 400°C show hysteresis with a finite coercive field and remanence at 300K from the SQUID magnetometry data. Superparamagnetic particle systems will not show hysteresis above their blocking temperature, where the temperature is high enough for the superparamagnetic moments to fluctuate faster than experimental measuring times. This suggests that if the cobalt precipitates are behaving as superparamagnets, then their blocking temperature should be higher than 300K.

The blocking temperature may be estimated using [140, 143]:

$T_B = \frac{KV}{25k_B}$

where K is the magnetic anisotropy constant (K = 4.1x10^5 J/m^3 for hexagonal cobalt [144], V is the particle volume, and k_B is Boltzmann's constant. Using this equation, the estimated diameter for a spherical cobalt particle with a blocking temperature of 300K is ~7.8nm. This is close to the particle size seen in the 30%Co film from TEM, which is about 5nm. The smaller particle size should show lower blocking temperatures, suggesting the blocking temperature in the films should be less than 300K, which is inconsistent with the magnetization curves at the same temperature. This suggests that if the particles are superparamagnetic, they do not contribute to the ferromagnetic moment seen in the films at room temperature. However, since T_B scales with the cube of the particle radius, a small deviation in the particle size will have a large effect on the blocking temperature and makes such an argument hard to justify based solely on the blocking temperature equation.

7.3.5.2 Magnetoresistance

The magnetoresistance (MR) of the films was measured simultaneously with the Hall data. The MR can provide some useful insights into the transport properties of semiconductors, including the potential landscape of the impurity distribution and lattice disorder. Aluminum was added as a codopant to some of the films to study the effects of electron concentration on the transport properties. Aluminum is a well know n-type dopant in ZnO; Al^{+3} substitutes on a Zn^{+2} site and dopes an electron into the lattice. Changes in the MR behavior at low temperature as a function of the electron concentration are found to be consistent with the notion of a critical carrier concentration at the Metal-to-Insulator Transition (MIT). The cobalt doped films transition from positive to negative MR as the electron concentration crosses the MIT.

In order to understand the MR results, a brief discussion of the metal-to-insulator transition is in order. Doped semiconductors will become metallic when sufficient overlap overcomes the localizing effects of electron-electron correlation and disorder. At a certain

concentration, electrons delocalize and their wavefunctions extend throughout the lattice. This is a well known metal-to-insulator transition in semiconductor materials.

At dilute limits, impurity states are isolated and electrons are confined to a hydrogenic orbital around their associated impurity. The radius of this orbital if given by $r_H = \epsilon(m/m^*)a_H$, where ϵ is the relative dielectric constant of the host material, m^* is the carrier effective mass, and a_H is the hydrogenic Bohr radius (a_H= 53pm) [31, 145]. As the impurity concentration is increased, the impurity orbitals begin to overlap to form an impurity band. The amount of overlap required to overcome the localizing effects of correlation is given by the Mott criterion,

$$(n_c)^{\frac{1}{3}} r_H \sim 0.25$$

where n_c is the critical concentration. The critical concentration for ZnO is about $4x10^{19}$ cm^{-3}. Below the critical concentration carriers remain bound to localized sites, but can move by hopping between occupied and empty states. This is the insulating regime of the MIT. Above the critical concentration, the impurity band states become delocalized and the carriers are itinerant.

As a reference, the MR behavior of an undoped ZnO film deposited in vacuum at 600°C is shown in figure 7-13. The MR is negative over the entire field range and is dependent on temperature. This is consistent with other reports found in the literature [78, 146, 147]. The negative MR in these reports was observed for highly n-type ZnO films with electron concentrations exceeding 10^{20}. Negative MR in highly doped semiconductors is thought to be caused by the weak localization correction to the conductivity [148]. Hall measurements on the film presented in figure 7-13 give carrier concentrations on the order of 10^{18}. This is well below the critical concentration of the MIT and demonstrates that the MR of nonmagnetic ZnO is negative on both sides of the MIT.

Figure 7-14 shows the MR behavior at various temperatures for three films doped with 5%Co. These films were deposited under slightly different conditions to impart different electron concentrations. The growth conditions are indicated in the figure for

each film. The electron concentrations as measured by the Hall effect are also provided in the figure. 2 at% Al was added to the third film to substantially increase the electron concentration. The MR for the three films is negative and qualitatively similar above 100K. The MR at high temperature is rather small being less than -0.5%. However, at low temperature the MR is substantially different between the films. At 10K, a progression from positive to negative MR occurs as the electron concentration is increased. Below the critical concentration of the metal-to-insulator transition, the MR is positive over the entire magnetic field. Near the critical concentration, a small negative MR component appears at low field. The MR value decreases from ∼10% to ∼1.5% as the MIT is approached. At concentrations much larger than the critical concentration (in the metallic conduction regime) the MR is negative over the entire field range, similar to the MR behavior of the undoped ZnO film.

The MR behavior was also studied for films heavily doped with cobalt. Figure 7-15 shows the MR data collected for two films, one doped with 30% Co and the other codoped with 30% Co and 2% Al. Again the Al is added to increase the electron concentration of the doped film. A similar progression from positive to negative MR across the MIT boundary is seen at low temperature. At higher temperature, the film doped only with cobalt, develops a kink in the MR curve near 10,000 Oe. To study the kink formation, the shape of the MR curve was tracked at temperatures between 10K to 100K and is shown in figure 7-16. The relative magnitude of the negative MR peak at zero-field gradually increases with temperature. Between 50K and 75K, this peak increases and the MR component at high-field becomes negative. The MR of the Co- and Al- codoped films is remarkably similar to the 5%Co, 2%Al codoped film, and qualitatively similar to the undoped film. This suggests that electronic transport is not greatly affected by the cobalt concentration above the MIT.

Figure 7-17 shows the temperature dependence of the resistivity for the 5% and 30%Co films. In the insulating regime, the resistivity decreases as the temperature is

increased. This is typical behavior for semiconductor films. Above the MIT, the resistivity increases with increased temperature, typical of metallic behavior. The temperature dependence is consistent with the notion that the Al doped films have crossed over into the metallic conduction regime.

The progression from positive to negative MR in figures 7-14 and 7-15 is commensurate with the metal-to-insulator transition. On the insulating side of the MIT, the MR is positive, and on the metallic side of the MIT, the MR becomes negative. Near the transition point, negative MR is seen at low field and positive MR at high field. However, as the temperature is increased, the positive MR component vanishes and only negative MR is seen. A similar dependence of MR on carrier concentrations around the MIT in cobalt-doped ZnO have been reported by Xu et al. and Kim et al. [51, 149]. Clearly, a model including the interplay of carrier concentration, doped cobalt spins, and temperature dependence is needed to explain the peculiar MR in these samples.

7.3.6 Effects of Annealing

In an effort to better understand the nature of these films and the origin of ferromagnetism, the 30%Co samples were annealed in both oxidizing and reducing atmospheres. The films were deposited in vacuum and it is assumed that most of the electrons are associated with oxygen vacancies in the lattice. Annealing the films in oxidizing conditions should fill the vacancies and reduce the electron concentration. A film was annealed at 500°C for 1 hour in 1 atm of oxygen. Table 7-2 shows the change in electrical properties after annealing. The electron concentration slightly decreased while the resistivity slightly increased. Most notably, the AHE in the oxygen annealed film was significantly smaller than that seen in the as-grown film. The Hall resistivity and magnetoresistance are shown in Figure 7-18. Since the change in electron concentration is small, one may require an alternative explanation to the diminished AHE coefficient. One possibility is that some of the cobalt metal dissolves into the ZnO lattice. This seems unlikely given that the high cobalt concentration is already metastable. It is also possible

that the cobalt metal reacts with oxygen to form cobalt oxide. However, XRD after annealing shows that the peak tentatively assigned to cobalt metal is still present in the film and that no cobalt oxides have formed (Figure 7-18(c)). Annealing may cause some change in microstructure, such as a change in size of the precipitates which can alter the transport behavior.

It is also possible that the oxygen anneal at 500°C is sufficient to drive out any hydrogen that resides in the lattice. Recent theoretical calculations suggest that hydrogen might mediate ferromagnetic interactions between cobalt atoms in a ZnO matrix [150]. To further explore this possibility, we have also annealed 30% Co-doped ZnO films in forming gas (4%H_2/Ar) at 500°C for 1 hour. Unfortunately, this anneal in hydrogen led to a decomposition of the ZnO:Co film, suggesting that the Co is indeed substitutional and metastable in the ZnO matrix. The SEM micrograph in Figure 7-19 shows the film decomposition after annealing in hydrogen. An XRD comparison in Figure 7-20 shows a large (almost 10 fold) increase in the intensity of the (111) Co metal peak as compared to the as grown film, indicating an increase in Co metal clustering. High-resolution four-circle XRD indicates the cobalt phase is aligned with the ZnO lattice. Cobalt metal can exist in either the hexagonal or fcc structure. The fcc phase is stable above 425°C but is often observed as a metastable phase at room temperature. Since the hexagonal and fcc structures differ only in their stacking sequence (hexagonal ABAB and fcc ABCABC) the fcc (111) planes have the same d-spacing as the (0001) hexagonal planes. Since standard θ-2θ XRD measures planes parallel to the sample surface, the hexagonal (0001) and fcc (111) orientations are indistinguishable [151]. However, since the periodicities of the planes are different, off-axis peaks (planes not parallel to the surface) can be used to identify the stacking sequence. To distinguish between the two phases, an off-axis diffraction scan through the Co (1 0 L) reciprocal lattice points was performed as shown in figure 7-21(a). The (1 0 L) scan should show peaks at integral L positions for hexagonal stacking and at particular integer/3 positions for cubic stacking [56]. The L-scan shows that the packing is

mostly cubic ABC stacking. However, a scan through the hexagonal cobalt (101) position, which cuts through the rod at L=1 in the L-scan, shows there is a small intensity at (101) as shown in the inset of the figure. This suggest some stacking faults are present or small regions of hexagonal cobalt. Additionally, a phi-scan through the cubic Co (200) at χ=35° shows in-plane alignment of the cobalt grains as shown in figure 7-21(b). Clustering should lead to an increase in the observed ferromagnetism since a larger volume of cobalt metal will have a larger magnetization, which is verified in Figure 7-22.

While the presence of Co metal precipitates in the films provides a possible explanation to the magnetic behavior, an examination of the magnetic behavior of the Co-doped ZnO films grown at different conditions provides circumstantial evidence that the cobalt precipitates are not the origin of the magnetic behavior. First, varying the growth conditions of the films has a large effect on the observed magnetization. Films grown at higher temperatures (500°C and 600°C) in vacuum show very little, if any, magnetization. Given that these large concentrations of cobalt are highly metastable, one would expect a stronger tendency to form more segregated cobalt metal at the higher temperature, but thermodynamically the antiferromagnetic CoO phase is stable. SQUID measurements show no evidence for ferromagnetism for ZnO:Co films grown at the elevated temperatures. XRD scans for these films were given in figure 7-5. SQUID characterization for these films is shown in figure 7-23. The coexistence of a cobalt metal XRD peak and the absence of ferromagnetism in the film grown at 500°C in vacuum is an interesting result. One would expect, from the sensitivity of the SQUID magnetometer, that the film would show magnetization in the presence of cobalt metal. The presence of CoO could be responsible for reducing the magnetization by removing cobalt from the lattice and precipitates. However the reduction in magnetization is over 100 times smaller as compared to the film grown at 400°C and may suggest that the small particles of cobalt metal do not make a large contribution to the magnetization.

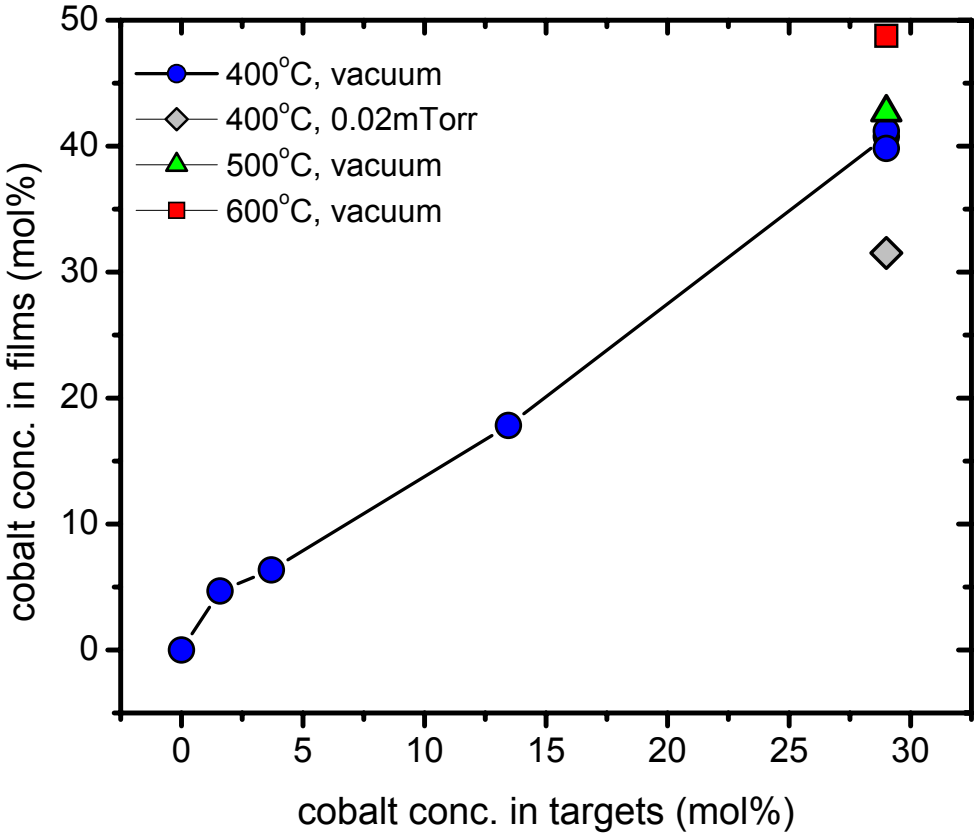

Figure 7-1. EDS results for a select number of films grown under different conditions. The data shows the cobalt concentration in the films as compared to the cobalt concentration in the target.

Table 7-1: Possible cobalt-induced secondary phases.

Phase	Structure	2θ (deg)	Coupling	T*(K)
Co	Cubic (111)	44.216	Ferromagnetic	Tc = 1373
	Hex (0002)	44.762		
CoO	Cubic (200)	42.401	Antiferromagnetic	Tn = 291
Co_3O_4	Spinel (400)	44.808	Antiferromagnetic	Tn = 30
$ZnCo_2O_4$	Spinel (400)	44.738	Antiferromagnetic (n-type)	N/A Ref[152]
			Ferromagnetic (p-type)	
$CoAl_2O_4$	Spinel (400)	44.692	Antiferromagnetic	Tn < 40

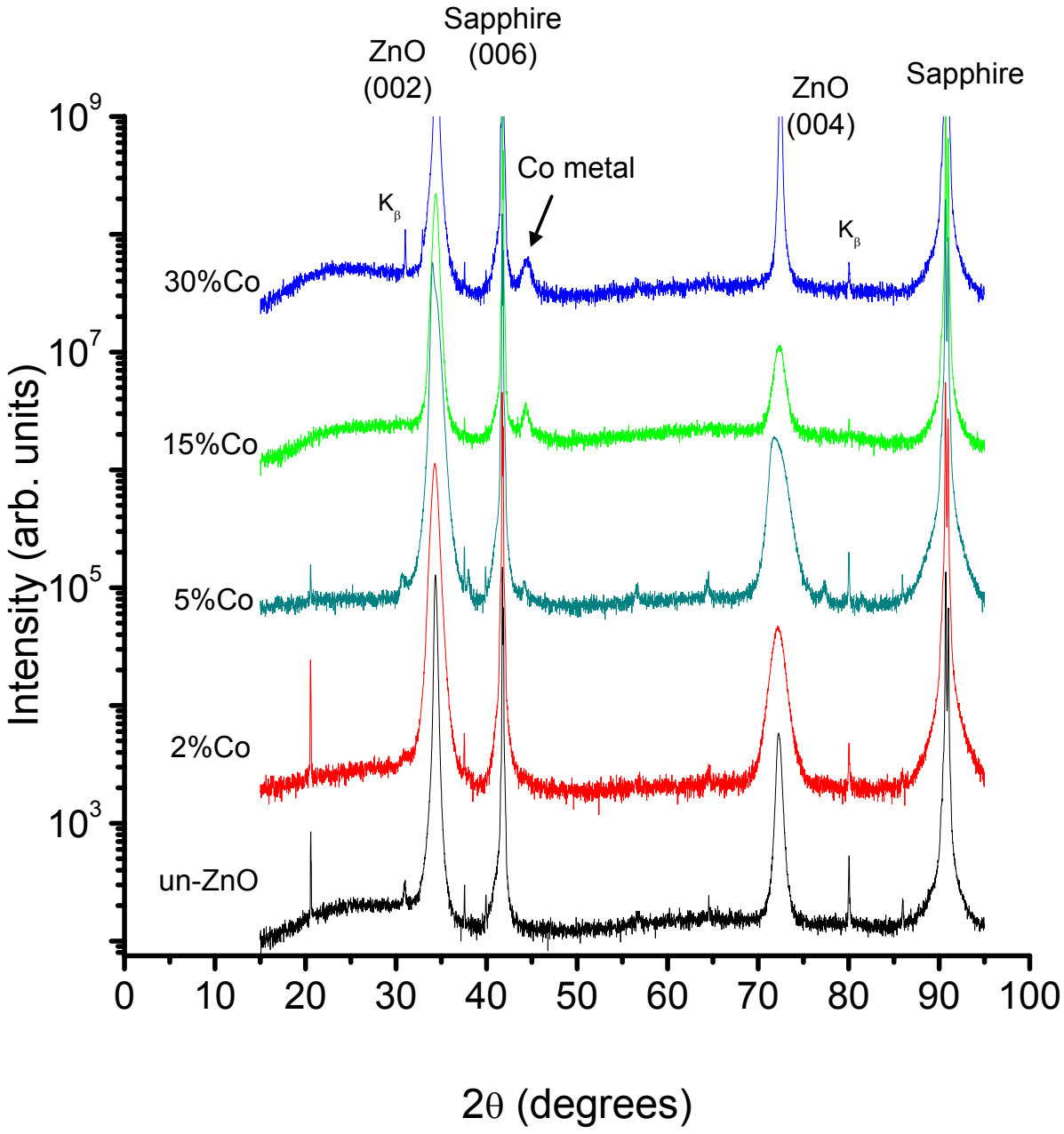

Figure 7-2. XRD scans for a series of films grown in vacuum at 400°C. The films are predominately c-axis oriented ZnO. At high cobalt concentrations, a cobalt induced secondary phase appears near 2θ=44.4°. TEM and High-resolution XRD suggest this phase is a mixture of cubic and hexagonal cobalt with stacking faults.

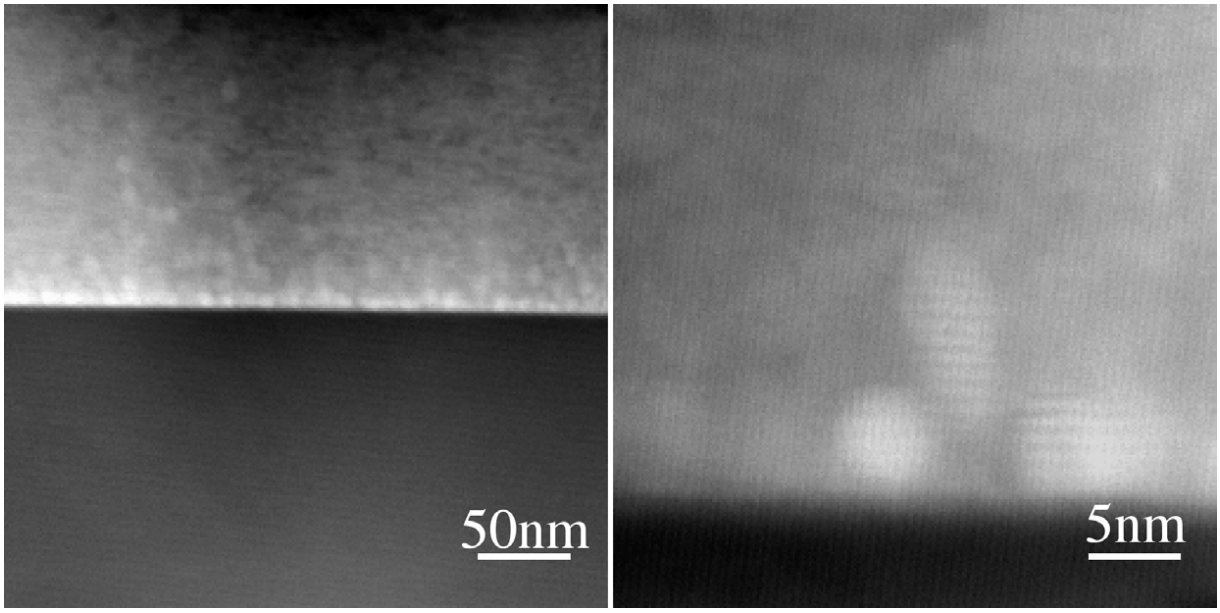

Figure 7-3. TEM micrographs of a sample doped with 30%Co that has cobalt precipitation present in the XRD scan. The precipiation appears mostly at the substrate/film interface.

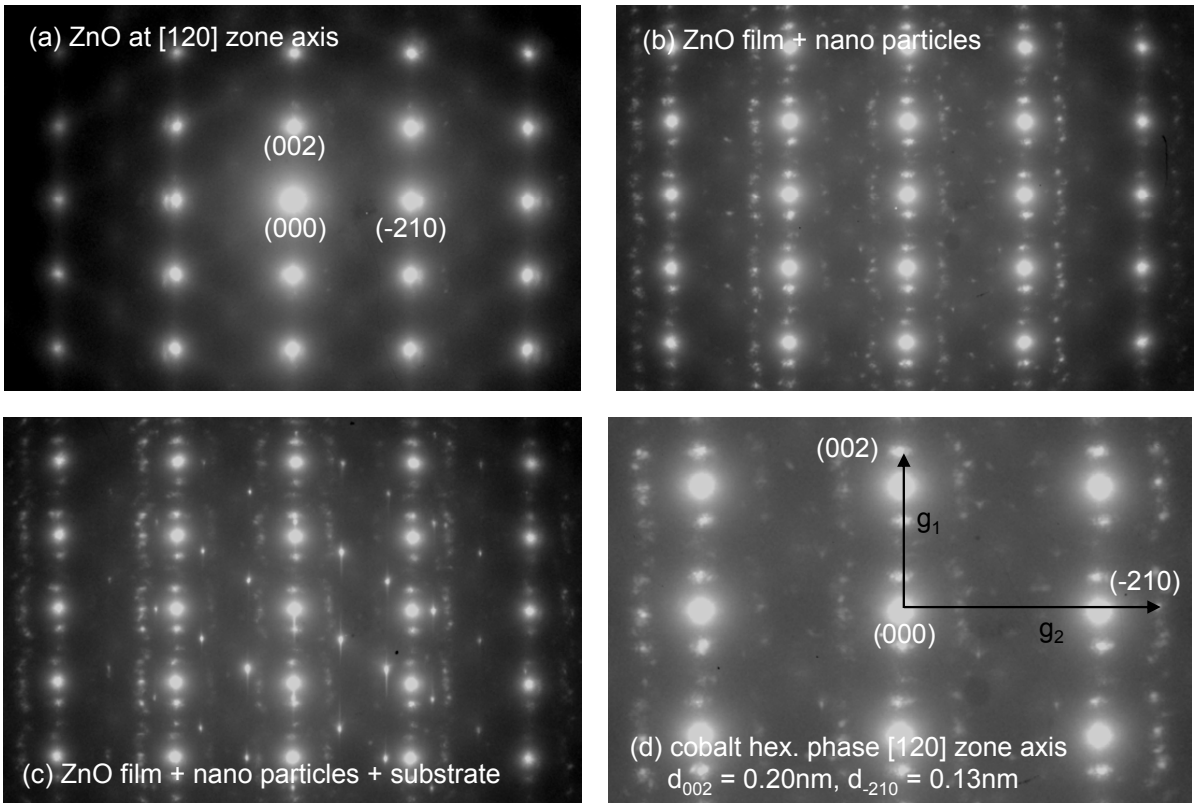

Figure 7-4. Convergent beam TEM diffraction patterns of ZnO film doped with 30%Co grown at 400°C in vacuum. (a) ZnO (hexagonal) film at [120] zone axis, (b) ZnO flim + nano particles, (c) ZnO film + nano particles + sapphire substrate, (d) Nano particle at [120] zone axis with d_{002}=0.20nm and $d_{\bar{2}10}$=0.13nm, which is consistent with metallic cobalt.

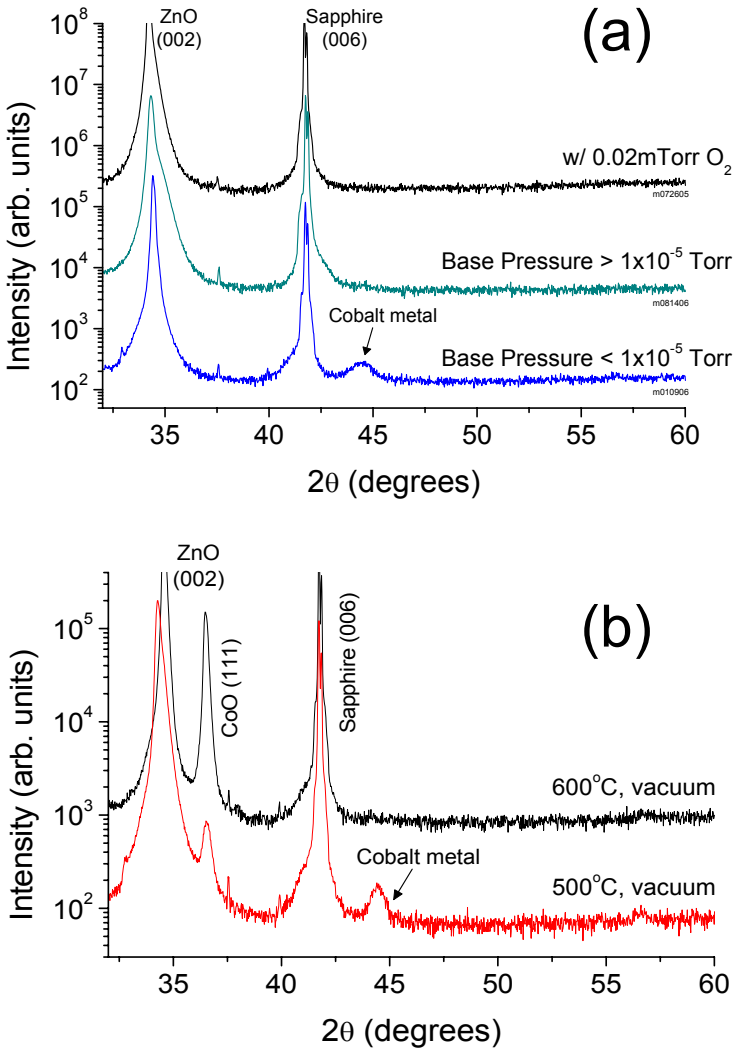

Figure 7-5. XRD scans for ZnO films doped with 30%Co. (a) Films deposited at 400°C with different pressure conditions. (b) Films deposited at 500°C and 600°C in vacuum.

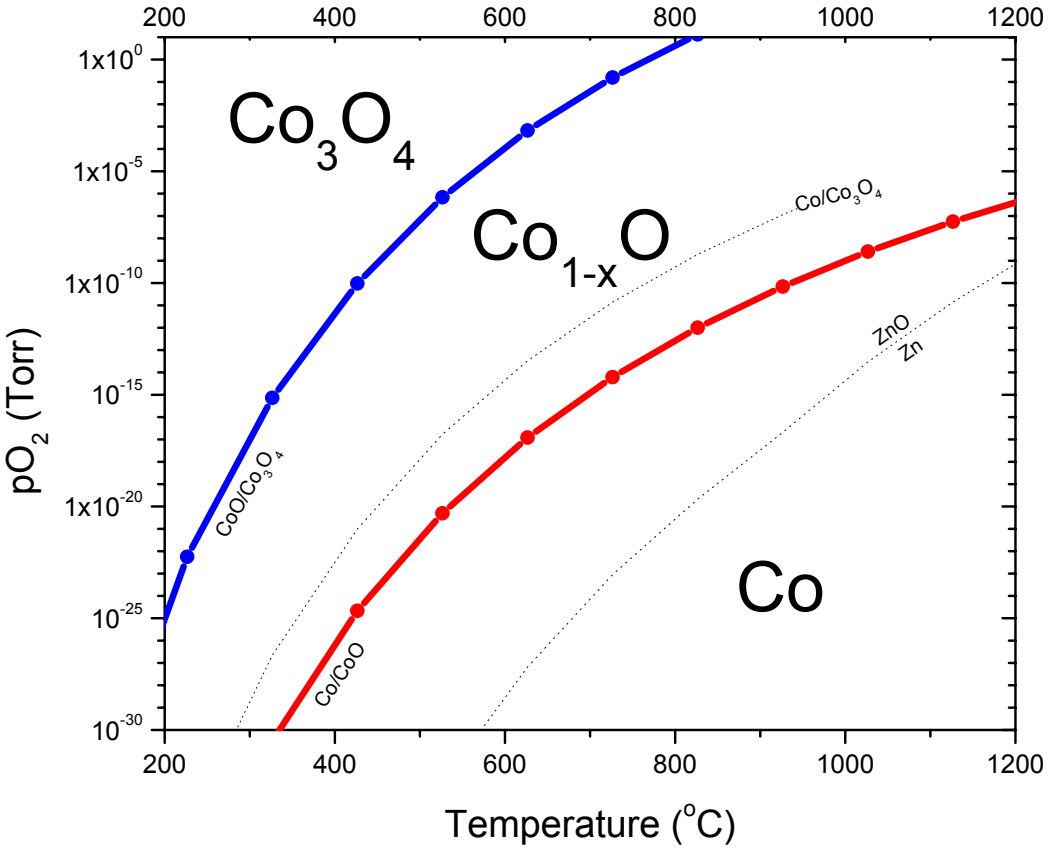

Figure 7-6. Thermodynamic predominance diagram for cobalt oxides.

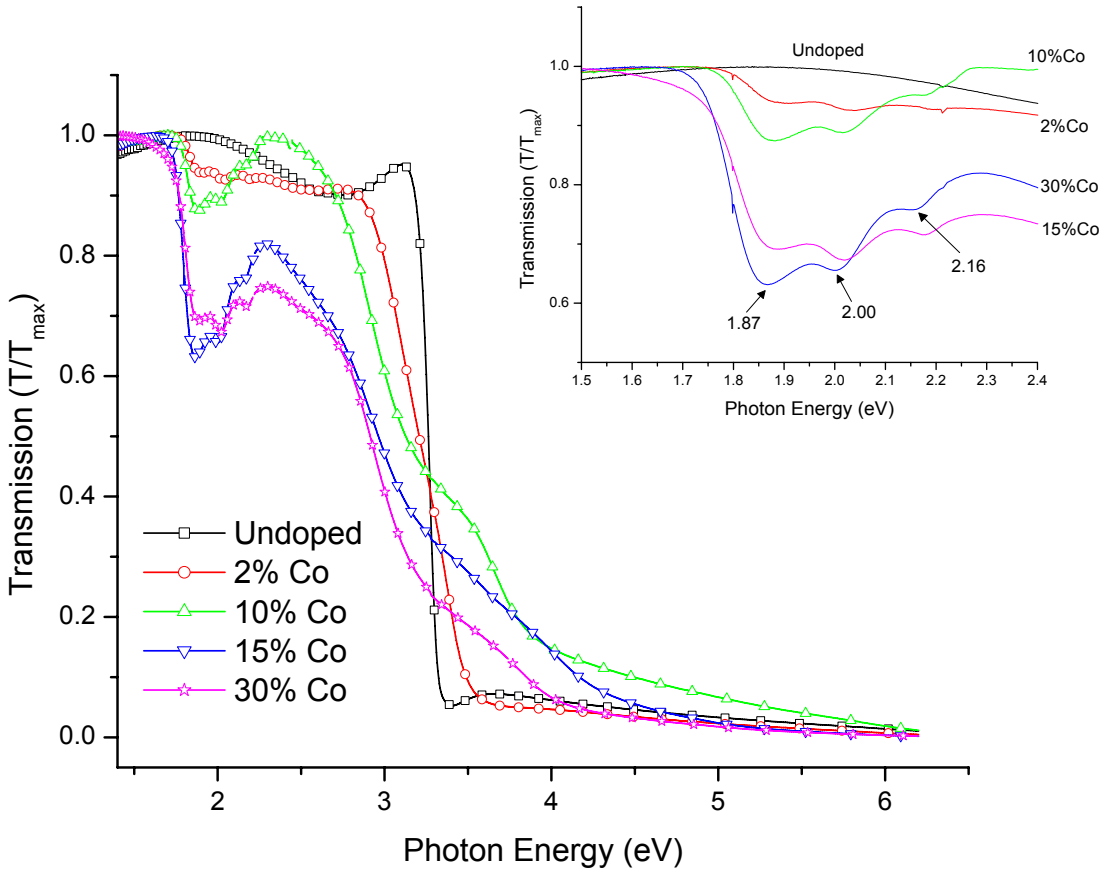

Figure 7-7. UV-Vis transmission of Co-doped ZnO films deposited in vacuum at 400°C. The inset shows a close up view of the absorption levels which correspond to the $^4A_2 \rightarrow^2 E(G)$ (1.9 eV), $^4A_2 \rightarrow^4 T_1(P)$ (2.0 eV), and $^4A_2 \rightarrow^2 A1(G)$ (2.2 eV).

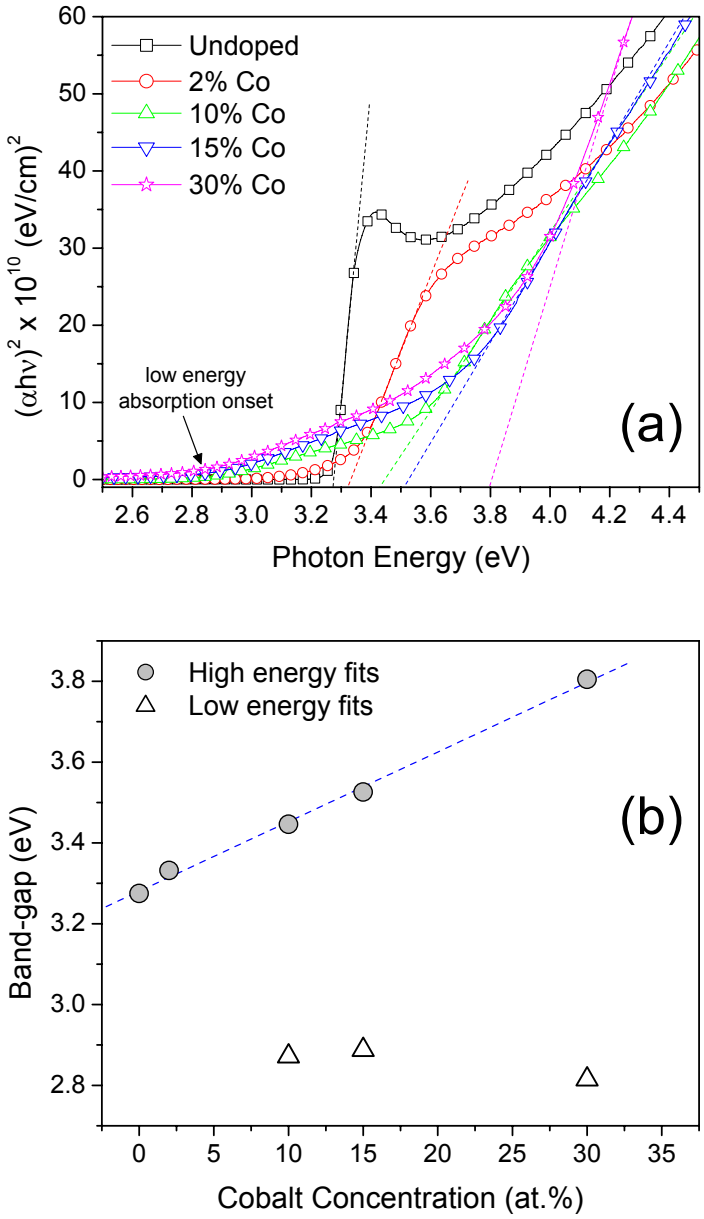

Figure 7-8. Optical band-gaps of Co-doped ZnO films. (a) $(\alpha h\nu)^2$ plots for Co-doped ZnO films deposited in vacuum at 400°C. Straight line fits through the linear regions of the plot are extrapolated to $h\nu = 0$ to find the band-gap. (b) Plot of the band-gap values as a function of nominal cobalt concentration. Filled circles are the band-gap and hollow triangles are the onset of absorption at low energy.

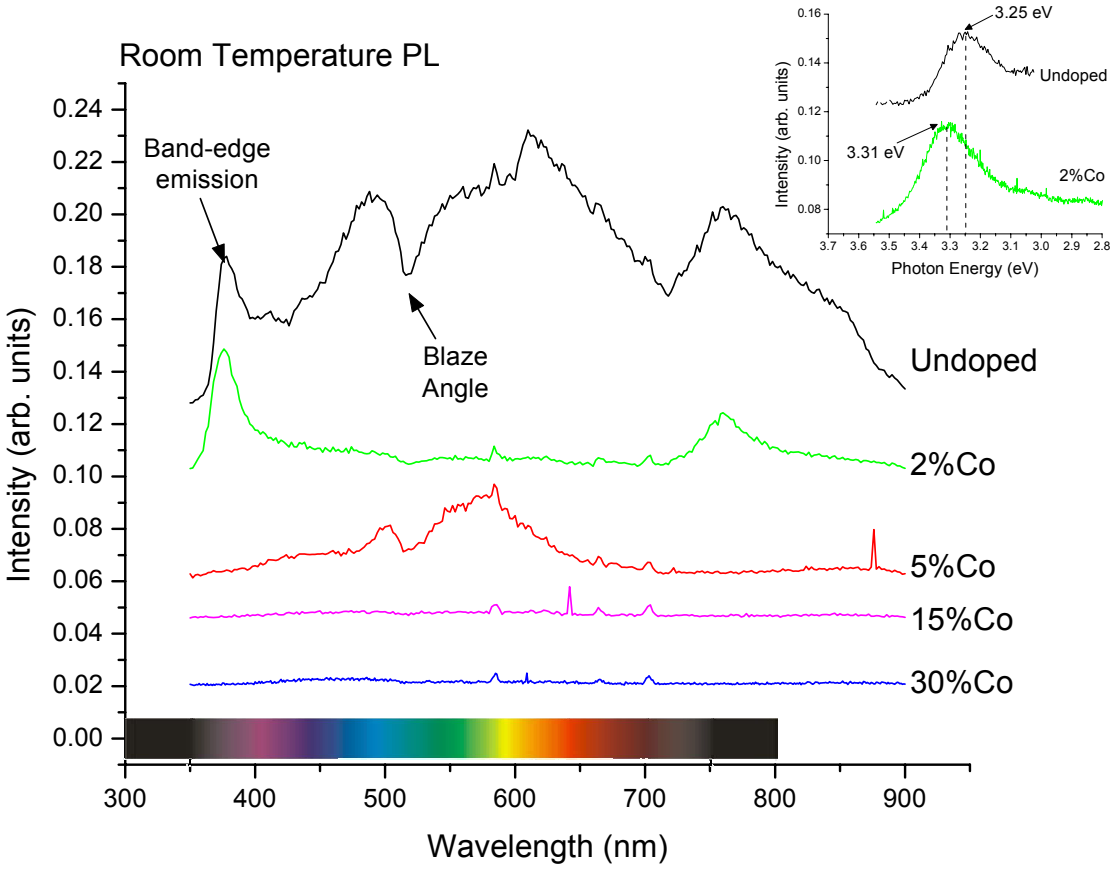

Figure 7-9. PL results for Co-doped ZnO films deposited in vacuum at 400C°C. The dip in the PL spectra at ~517 nm is an artifact from the diffraction grading blaze angle. The PL intensity decreases with higher cobalt doping. The inset shows higher resolution scans around the band-edge peak for the undoped and 2%Co samples. The values correspond well with the absorption data.

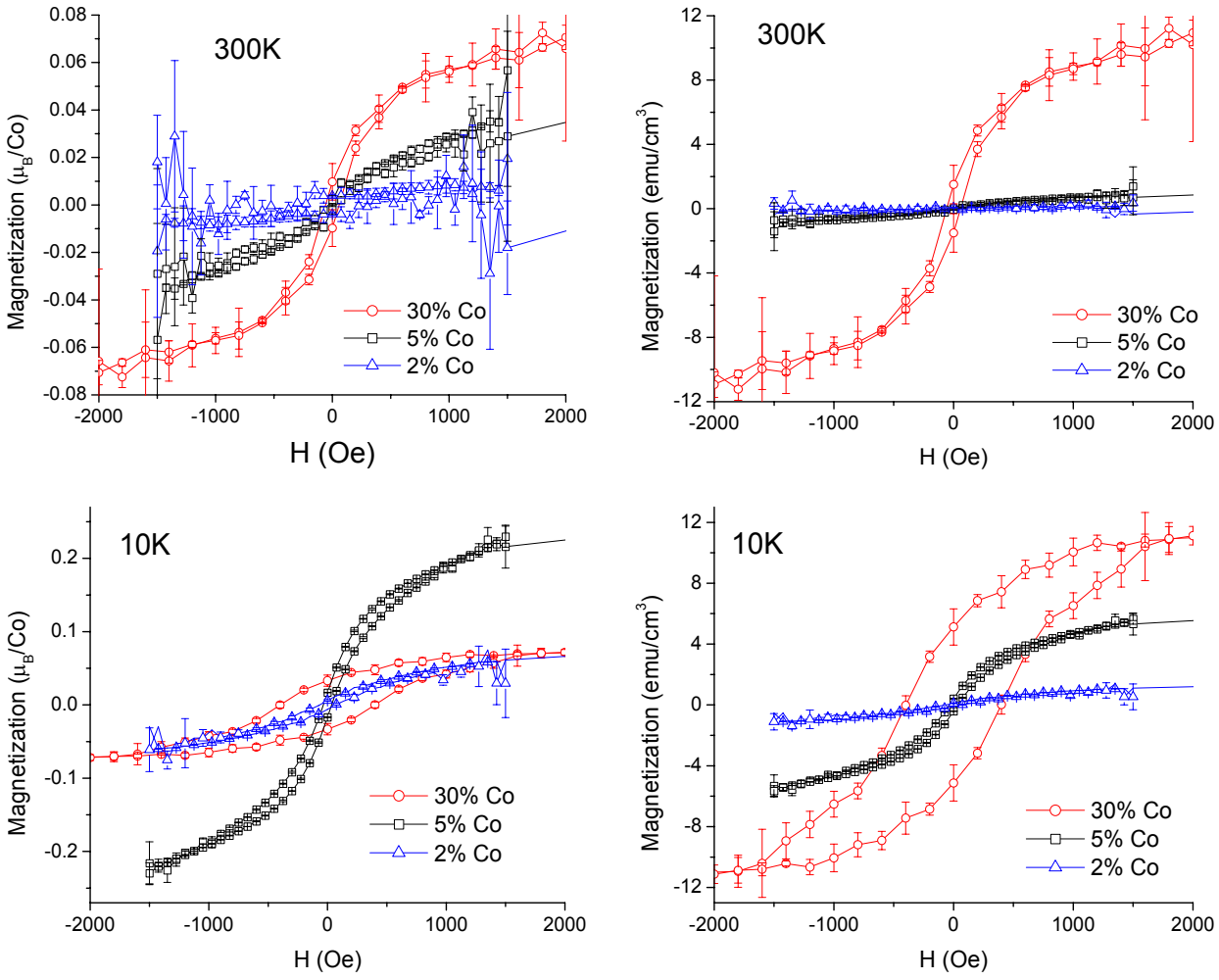

Figure 7-10. SQUID magnetization curves for Co-doped ZnO films deposited at 400°C in vacuum. The films do not show any secondary phases by XRD measurement.

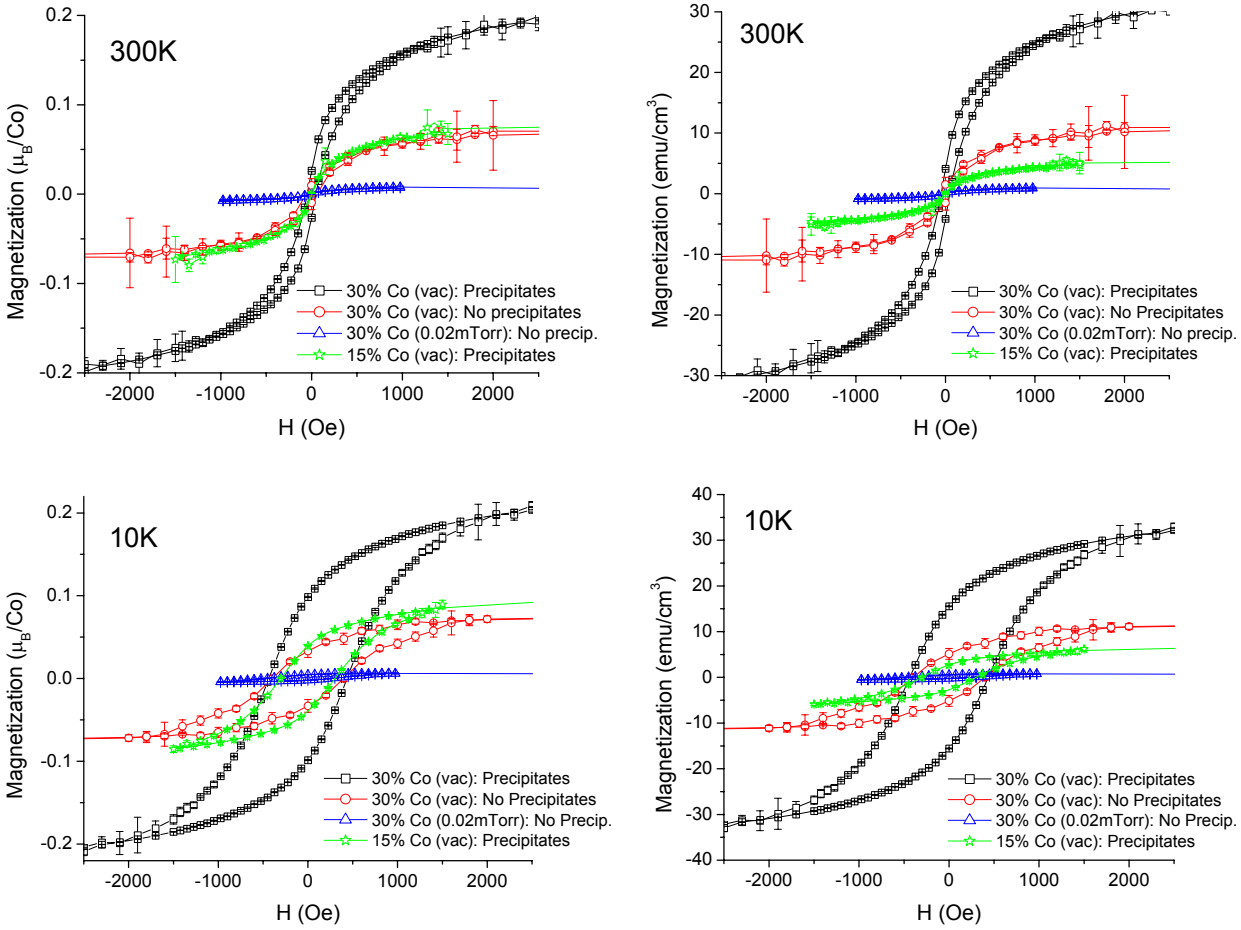

Figure 7-11. SQUID magnetization curves for Co-doped ZnO films deposited at 400°C. The growth pressure and whether the film contains secondary phase precipitation is indicated in the legend.

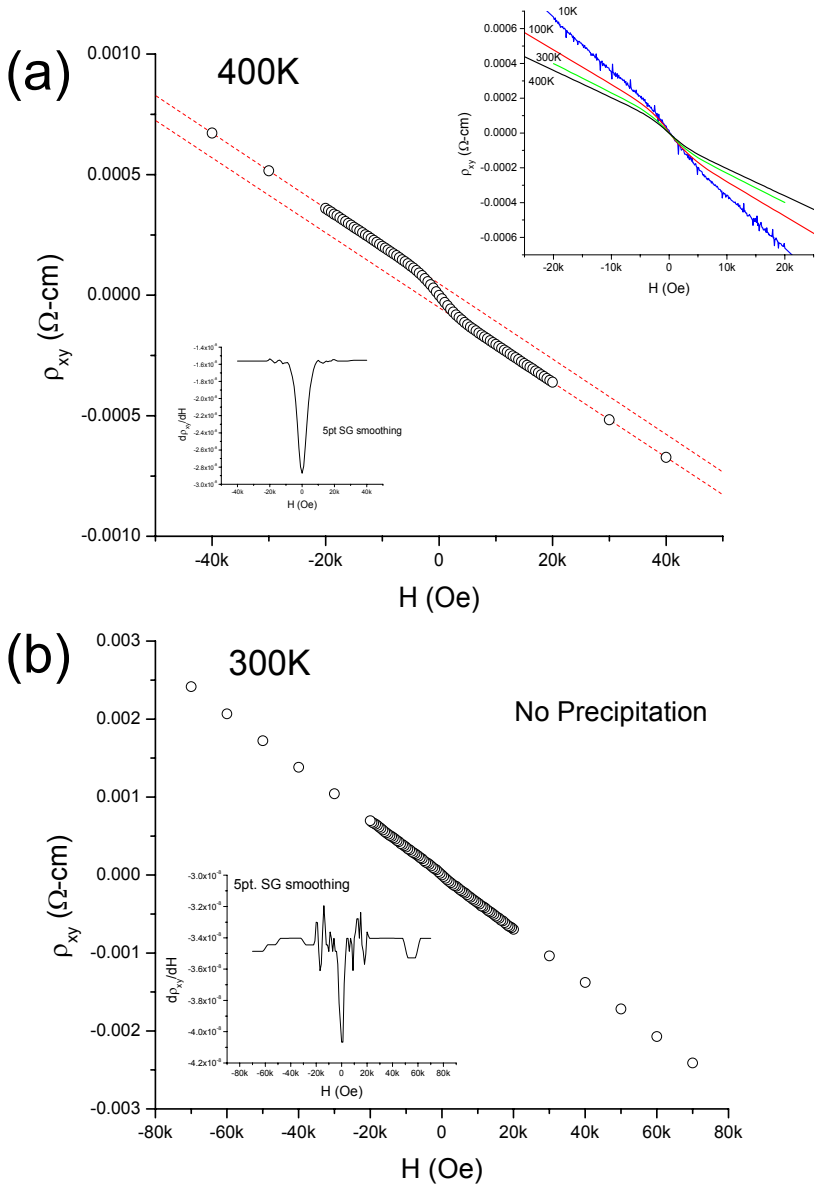

Figure 7-12. Anomalous Hall effect in 30%Co-doped ZnO. Films were grown at 400°C in vacuum. (a) film with cobalt precipitation. The upper inset shows the Hall curves at different temperatures. The lower inset shows the derivative of the Hall curve. (b) film without cobalt precipitation. The inset shows the derivative of the Hall curve.

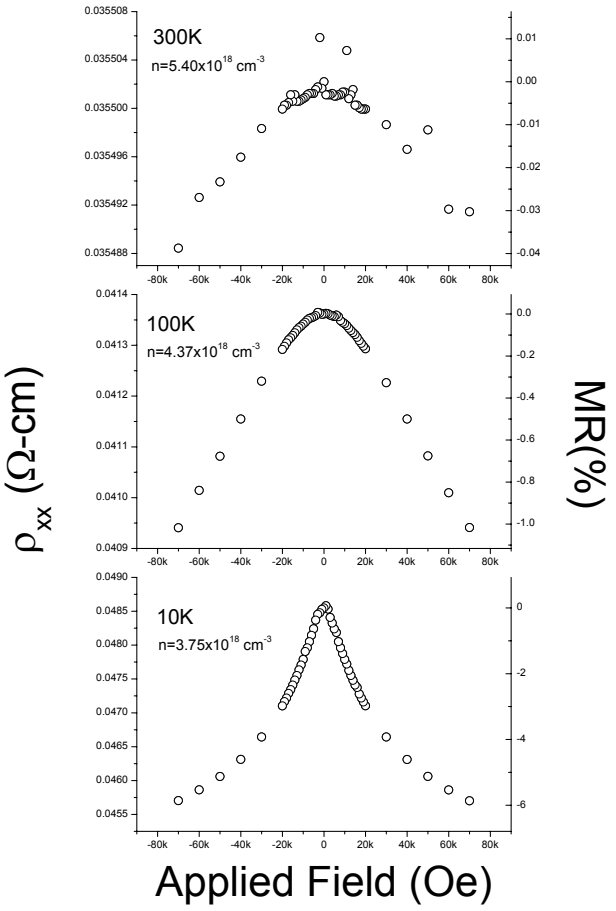

Figure 7-13. The magnetoresistance of an undoped ZnO film. The film was deposited at 600°C in vacuum. The measurement temperature and carrier concentration are indicated in each figure.

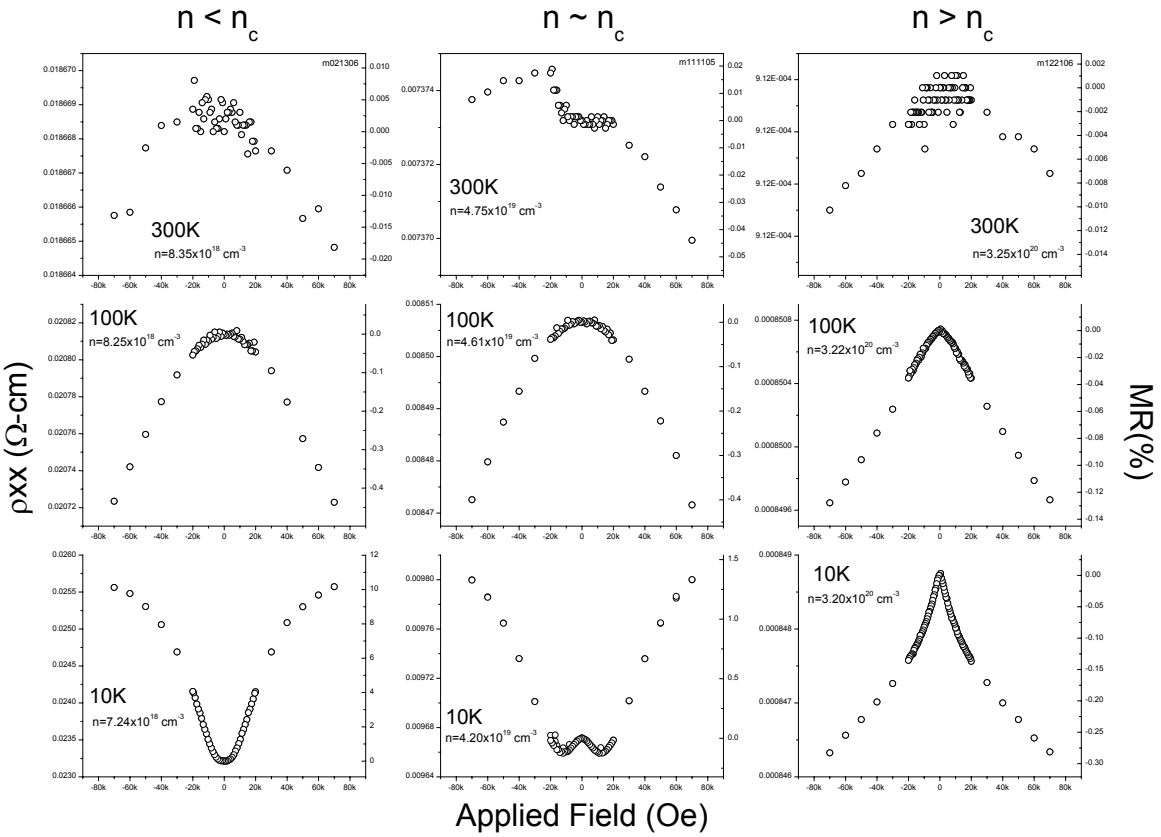

Figure 7-14. The magnetoresistance of 5%Co-doped ZnO films. The film with $n<n_c$ was grown at 600°C in 0.02mTorr oxygen. The film with $n\sim n_c$ was deposited at 400°C in vacuum. The film with $n>n_c$ was deposited at 400°c in vacuum and is codoped with 2%Al to impart a high electron concentration.

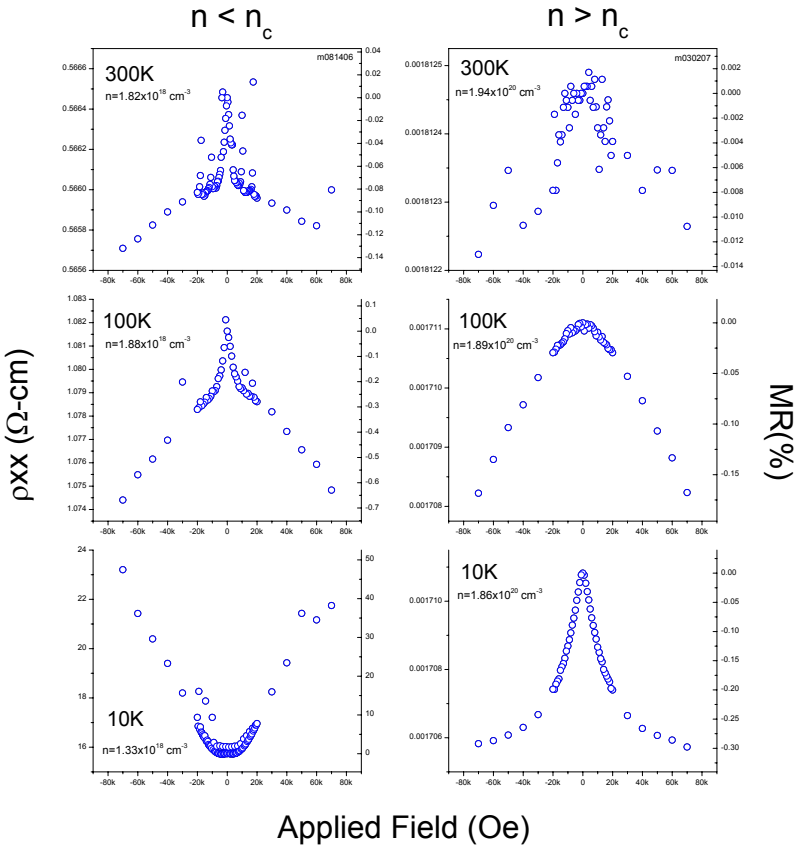

Figure 7-15. Magnetoresistance of 30%Co-doped ZnO films. Both films were deposited at 400°C in vacuum. Neither films show signs of a secondary phase by XRD measurement. The film with $n>n_c$ is codoped with 2%Al to impart a high electron concentration.

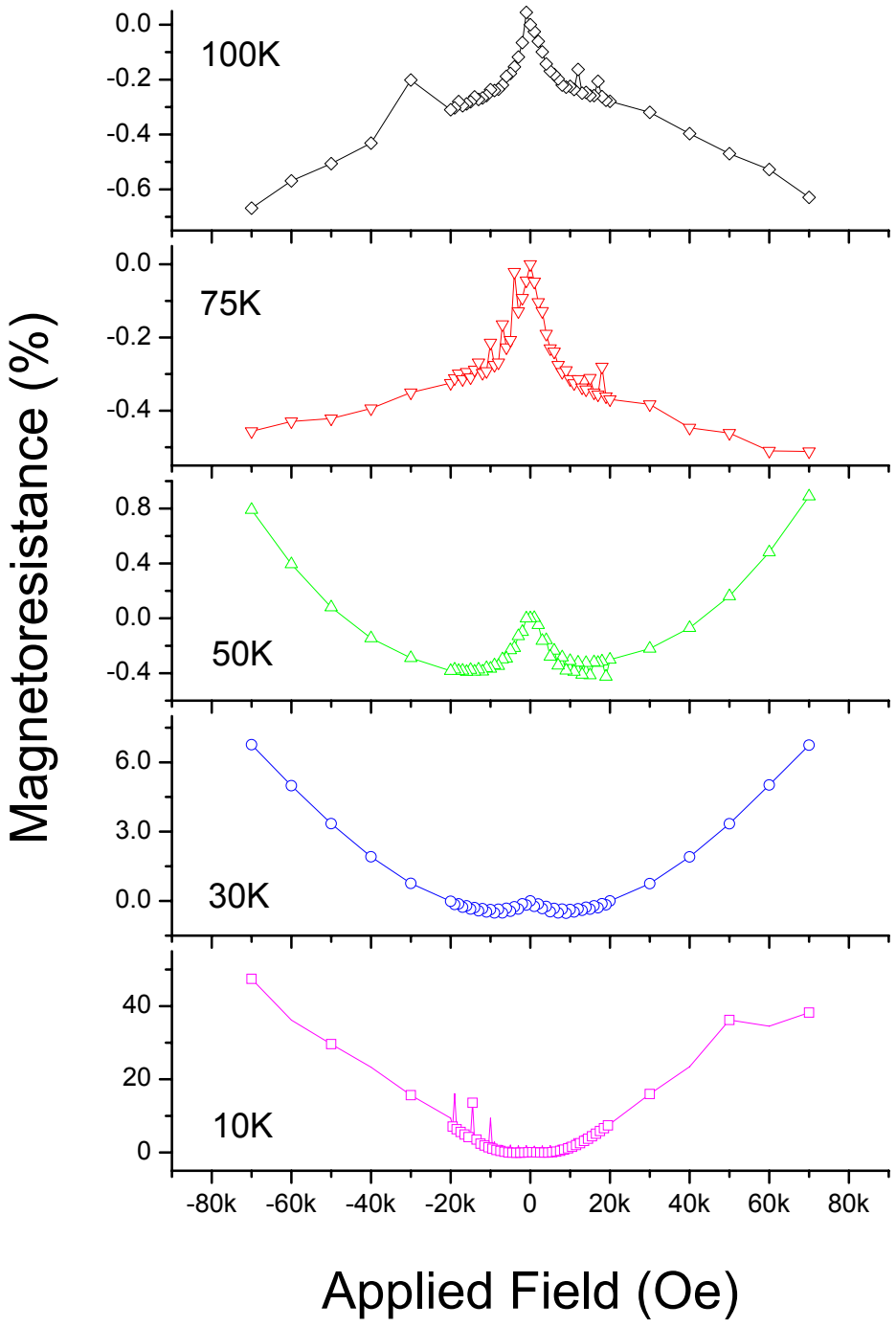

Figure 7-16. Magnetoresistance of 30%Co-doped ZnO film at temperatures between 10K to 100K. The development of the negative MR kink is established at low temperature followed by a transition to negative MR across the entire field range with increased temperature.

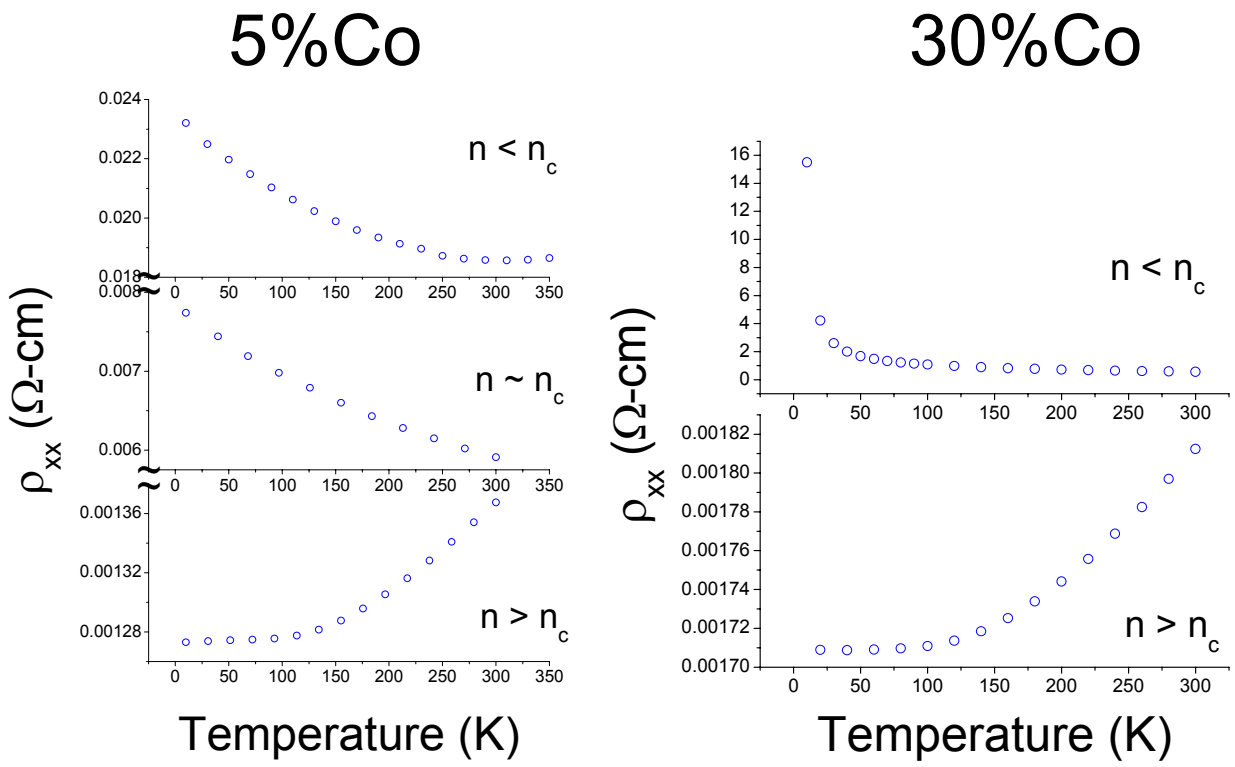

Figure 7-17. Temperature dependent resistivity measurements for 5% and 30% Co-doped ZnO films.

Table 7-2. Transport data for a 30%Co-doped ZnO film with cobalt precipitation. Data is for before and after annealing in O_2 at 500°C.

	Ro (cm^3 C^{-1})	Carriers (cm^{-3})	Mobility (cm^2 v^{-1} s^{-1})	Zero-field ρ_{xx} (Ω-cm)
As deposited	-1.685	$3.70x10^{18}$	7.12	0.2367
O_2 annealed	-2.998	$2.08x10^{18}$	8.97	0.3344

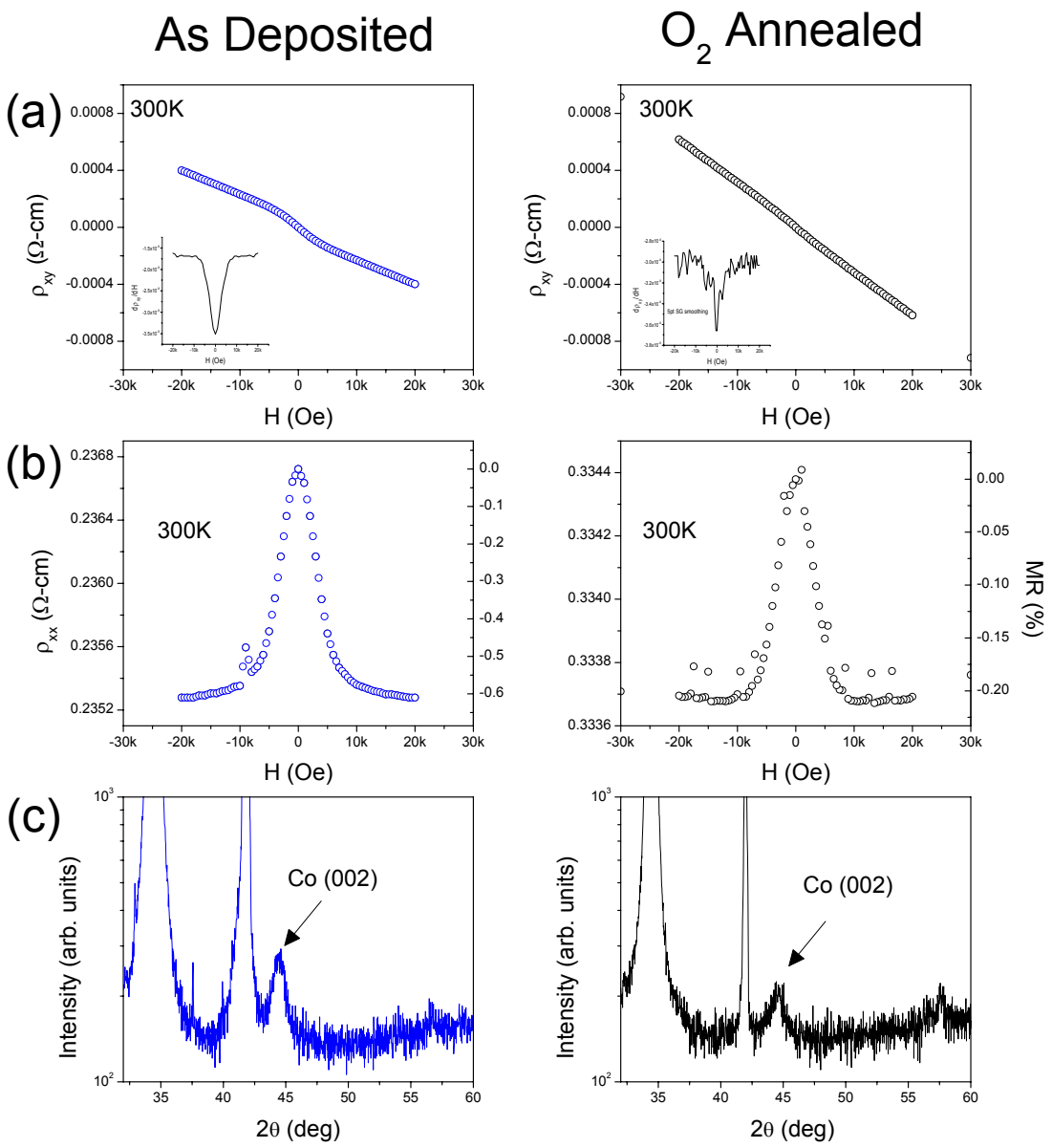

Figure 7-18. Hall resistivity and magnetoresistance for a 30%Co-doped ZnO film with cobalt precipitation. Data is shown before and after annealing in O_2 at 500°. Insets show the derivates of the Hall resistivity to show AHE.

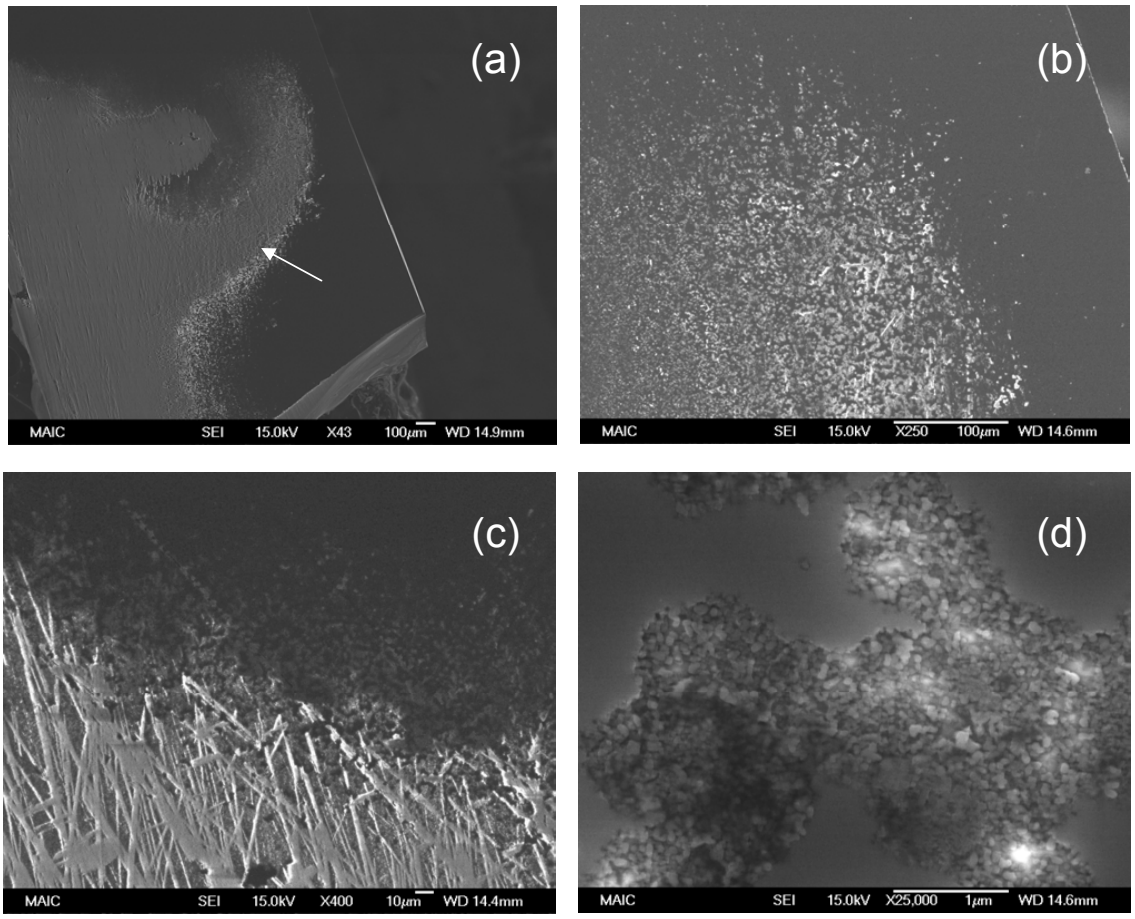

Figure 7-19. SEM micrographs at different magnifications of the surface of a Co-doped ZnO film that has been annealed in H_2/Ar at 500°C for 60min. Magnification and scale bars are given in each micrograph. The arrow in (a) shows the region of film degradation. This area was brown in color compared to the green color of the film.

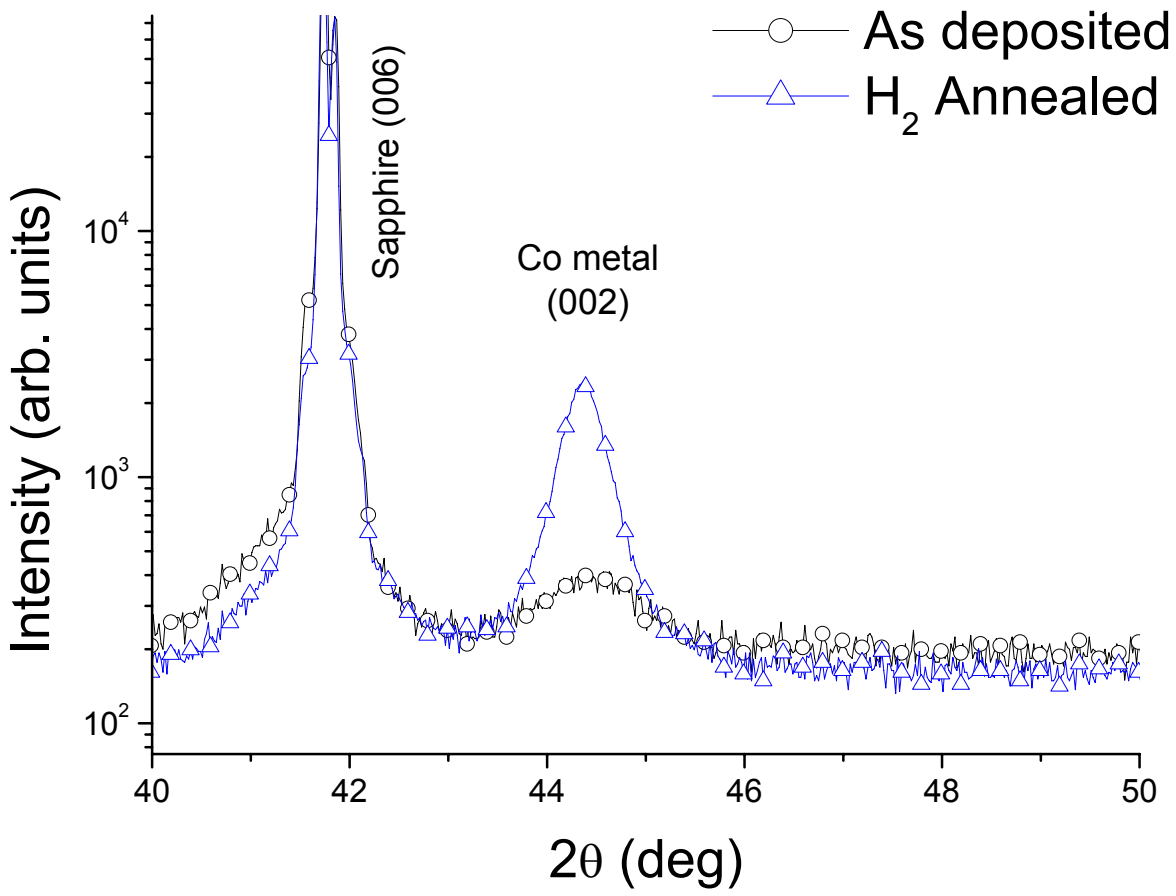

Figure 7-20. θ-2θ XRD for a 30%Co-doped ZnO film before and after annealing in forming gas at 500°C.

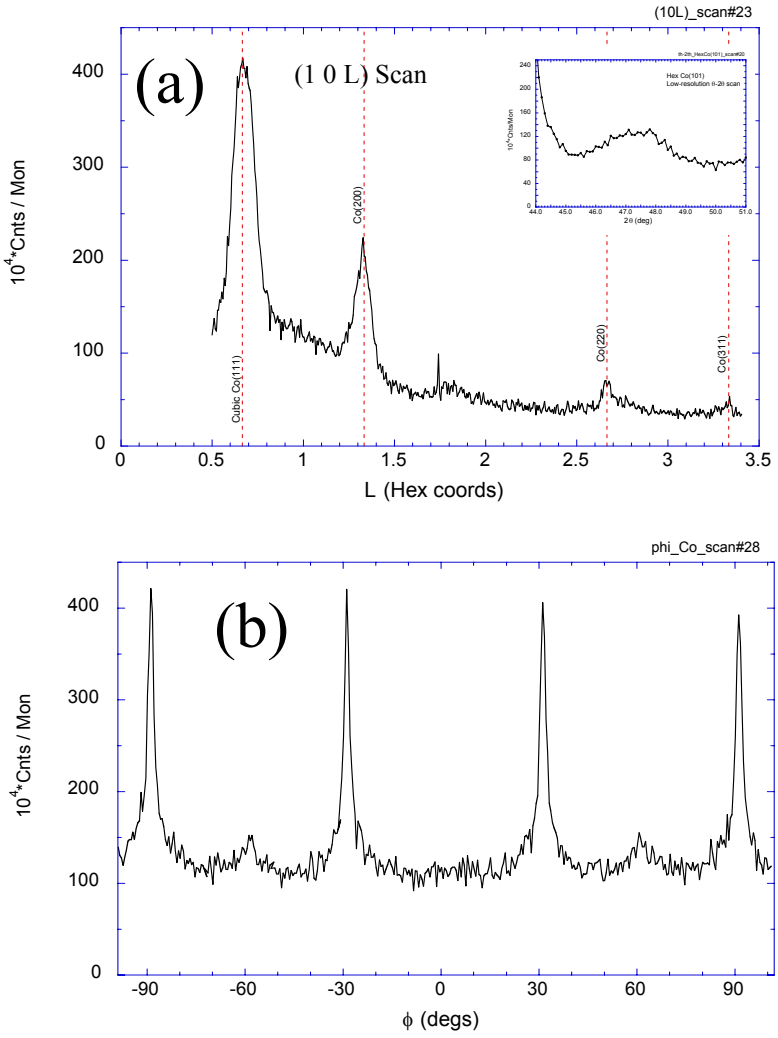

Figure 7-21. High-resolution XRD scans for 30%Co-doped ZnO film that has been annealed in forming gas at 500°C. (a) L-scan along the Co (10L). The inset shows an off-normal θ-2θ scan through the hexagonal Co (101). (b) phi-scan through the Co (200) at χ=35°.

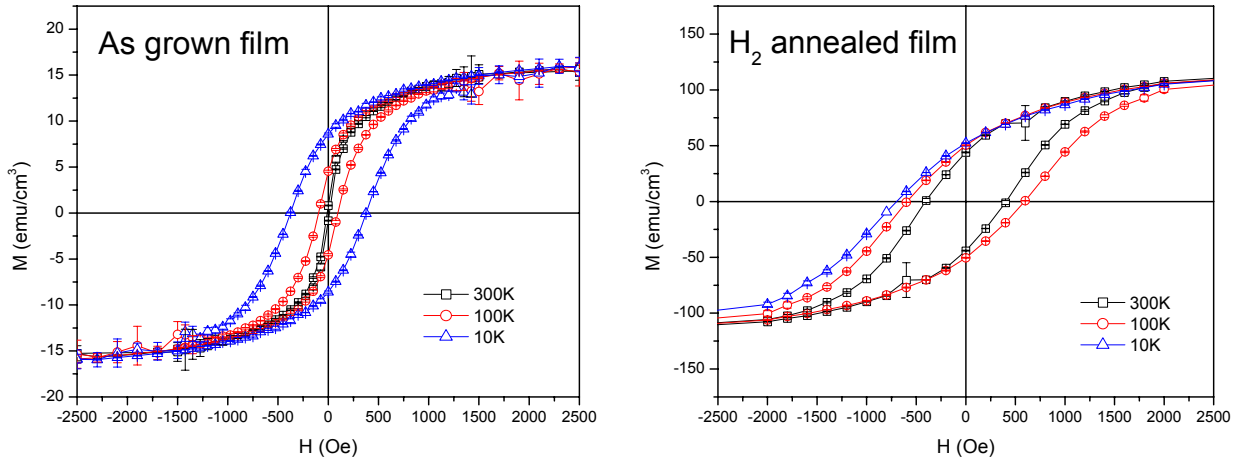

Figure 7-22. SQUID magnetometry for a 30%Co-doped ZnO film before and after annealing in forming gas at 500°C.

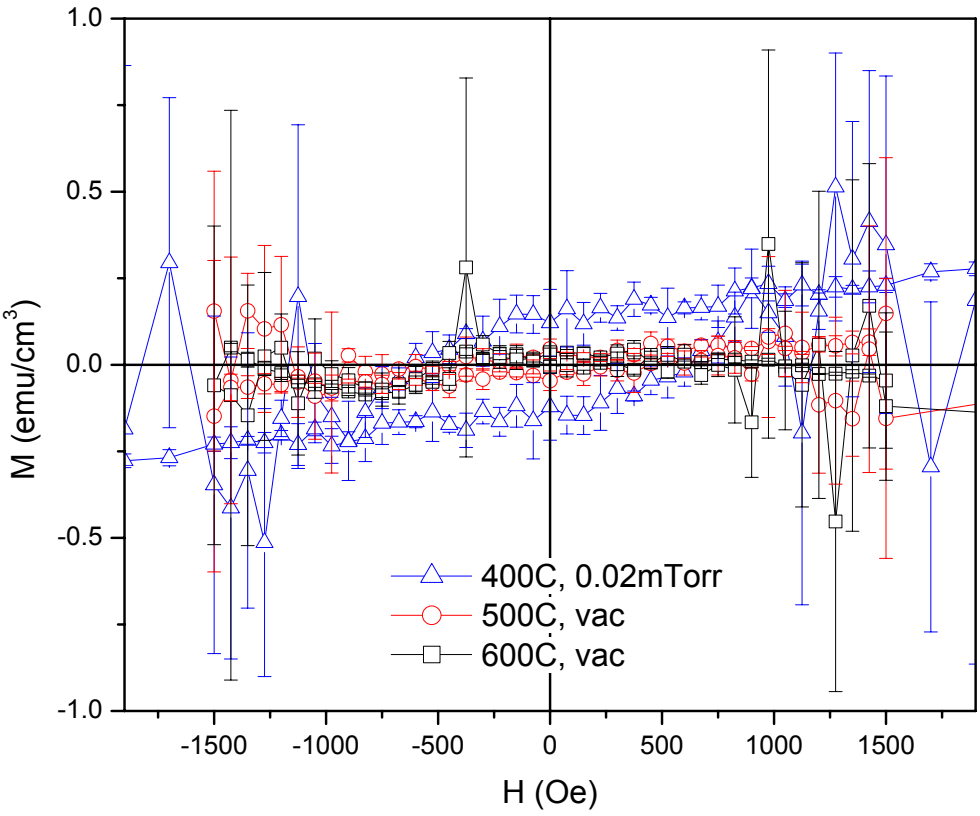

Figure 7-23. SQUID magnetometry for 30%Co-doped ZnO films deposited under differerent conditions.

CHAPTER 8
CONCLUSION

The advancement of spintronics as a practical technology depends upon the development and understanding of semiconductors that can support spin-polarized carrier operation above room temperature. The research presented in this dissertation explored the possibility of using wide band-gap oxide semiconductors as spintronic materials. Both transition-metal doped Cu_2O and ZnO were investigated. Mn and Co were used as the transition-metal dopants to provide localized spins in the host semiconductor lattice. Thin films of these materials were deposited using pulsed laser deposition. Various material properties including the structure, magnetic, and electronic transport properties were then characterized to gain a better understanding of the materials.

8.1 Mn-doped Cu_2O

The magnetic properties of Cu_2O films doped with 1 at.% Mn were investigated under different growth conditions. This research was stimulated by Dietl's theoretical prediction that carrier-mediated ferromagnetism is favored in Mn-doped, highly p-type, wide band-gap semiconductors, such as ZnMnO and GaMnN. Cu_2O is a naturally p-type semiconductor with a wide (direct) band-gap and therefore holds interest in exploring spin behavior in oxides.

The Mn solubility in Cu_2O was found to be small and the precipitation of Mn-oxides was favored at high growth temperatures. However, metastable incorporation of Mn in the Cu_2O could be achieved at low temperature (400°C). These phase pure samples were found to be non-ferromagnetic. Ferromagnetism with a Tc$\sim$50K was observed in the films deposited at higher temperatures, but appears to be associated with a Mn_3O_4 secondary phase which has a Tc near 50K.

Spintronic concepts based on ferromagnetic semiconductors require the distribution of charge carriers in the semiconductor to be spin-polarized. Magnetism derived from localized magnetic precipitates is of little utility for semiconductor-based spintronics if

the carriers are not polarized. Therefore, based on the collected data, it is concluded that Mn-doped Cu_2O has limited use as a ferromagnetic semiconductor under the studied growth conditions. The low solubility of Mn in the Cu_2O lattice limits experimentation using larger concentrations of Mn. Perhaps larger hole concentrations or alternative fabrication techniques could be used to induce ferromagnetism.

8.2 Mn-doped ZnO

Several of the proposed models for ferromagnetism in ZnO DMS emphasize the importance of holes mediating the exchange interaction between doped Mn spins. This research investigated the trends in the magnetization as a function of carrier concentration in order to elucidate the role of charge carriers on the ferromagnetism in these materials. The carrier concentration was varied using Sn and P as electronic codopants. Codoping allowed independent control over the magnetic and electronic properties by doping each separately. This provided a platform to study the effects of carrier concentration on the observed magnetic properties. Sn acts as an n-type dopant providing extra electrons to the ZnO. P acts a p-type dopant that supplies holes to compensate the native electron concentration in ZnO. Thin films doped with 3 at.%Mn, and either Sn or P as the codopant, were deposited in an oxygen atmosphere of 20mTorr in a temperature range of 400–600°C.

The electron concentration in the ZnMnO:Sn films was controlled by varying the Sn content. Initially, the magnetization increased with minimal Sn doping resulting in a maximum magnetization of 0.5 μ_B/Mn atom at 300K. However, with increased Sn doping there was an inverse correlation between the Sn content and the saturation magnetization. As the electron density increased with Sn doping, the magnetization decreased.

The trend in magnetization showed a similar carrier dependence using P as a codopant. Under conditions where the acceptor dopants were activated, the magnetization was enhanced. The resistivity of the as-deposited film was ∼4,000 Ω-cm at 300K with an

electron density of ~3x10^{15} cm^{-3}, and became too insulating to measure after annealing. The saturation magnetization after annealing was around 0.15 μ_B/Mn atom.

The correlation of saturation magnetization with electron density is interesting and provides some insight into the mechanism for ferromagnetism in ZnMnO. Overlap of the Mn d-states with the valence band suggests holes are necessary in order to induce ferromagnetic ordering. Magnetism in low free-electron density material is consistent with the bound magnetic polaron model in which bound acceptors mediate the ferromagnetic ordering. The holes may be delocalized, but with low mobility, thus yielding low conductivity. In this case, the carrier mediated mechanism may suffice without the need to invoke bound polarons as inherent to the ferromagnetic ordering. In either case, the addition of electrons to the system will move the Fermi energy level up in the band-gap, resulting in a decrease in hole density and a reduction in magnetization.

While the trend of magnetization versus carrier density was similar in the Sn and P codoped films, the measured magnetization was slightly different. The magnetization was anticipated to be larger for the annealed P-doped films, as compared to the Sn-doped films, since the Fermi level should reside closer to the valence band. However, this was not observed; films with minimal Sn doping exhibited a higher magnetization per Mn atom. The reason for this is unclear, but could be a result of other defects formed after the annealing process. The XPS data also suggested a change in valence of some of the Mn atoms after annealing. This may have caused a reduction in magnetic moment that competed with the suppressed electron density. Nevertheless, the overall trend of magnetization versus carrier density was consistent between the experiments.

The results of this work are consistent with the observations of Kittilstved and coworkers [32]. The authors concluded that ferromagnetism in ZnO is closely tied to the charge transfer electronic structure of the transition-metal dopant. For Mn, ferromagnetism is induced when the holes from the acceptor states hybridize with the

Mn ions. Ferromagnetism was observed when the ZnO was locally doped p-type, but no ferromagnetism was observed when doped n-type.

8.3 Co-doped ZnO

The effect of cobalt-doping on the magnetic and magneto-transport behavior in ZnO was also investigated. Ferromagnetism was found in films deposited at low temperature (400°C) in vacuum, while films deposited in oxygen or at higher temperatures were non-magnetic. Films deposited under vacuum had rather high electron concentrations and are presumably doped with oxygen vacancies. Segregation of cobalt metal occurred in films doped with 15% or greater Co concentrations when deposited in low base pressure ($<10^{-5}$ Torr) vacuum conditions. The precipitates were small ($\sim$5nm) and aligned with the ZnO lattice. The segregation could be suppressed by depositing in higher base pressures ($>10^{-5}$ Torr), but the process was not fully reproducible. These films also show ferromagnetism albeit with lower magnetization than the films with metallic cobalt. This suggests that the cobalt metal particles could be responsible for some of the observed magnetic properties in the films with precipitation. However, the role and the extent of magnetization from the particles is uncertain. The distribution of particles that behave ferromagnetically, or behave superparamagnetically because of their small size, and to what extent the film properties have on the ferromagnetism in the precipitated films, is unclear.

The cobalt-doped films also exhibited peculiar magnetoresistance that had a strong dependence on the carrier concentration. The MR was studied in films with 5%Co and 30%Co doping, along with an undoped ZnO film as a reference. At low temperature, the cobalt-doped films undergo a progression from positive to negative MR as the electron concentration is increased and the films cross over the metal-to-insulator transition (MIT). At large carrier concentrations, well into the metallic regime, the MR behavior for the undoped, 5%Co, and 30%Co films is quite similar. This suggests that the electronic transport is not greatly affected by the cobalt concentration above the MIT. One possible

explanation is that since the Fermi energy has moved fully into the conduction band, the transport is dominated by the character of the conduction band. In an applied magnetic field, the cobalt d-states and the donor impurity states are split into spin-up and spin-down sub-bands. If the Fermi energy lies in the conduction band, there is likely no overlap of the Fermi energy with the spin-polarized d-bands of the cobalt, and the conduction is characteristic of undoped ZnO.

A possible future experiment that may prove interesting in understanding the MR behavior could be executed through the fabrication of field-gated Hall bars. Voltage applied to a top gate electrode could be used to vary the electron concentration near the vicinity of the gate. Magnetoresistance and Hall measurements could then be performed at varying gate voltages to examine their behavior with different electron concentrations. Ideally, one could smoothly study the MR behavior across the MIT and closely examine the changes near the transition point.

APPENDIX A
HALL EFFECT SYSTEM AND EQUIPMENT

A.1 Introduction

I've added this information for readers interested in detailed information regarding the resistivity and Hall effect methods used in this work. I first wrote this section as a reference for my research group to introduce them to the equipment. However, after a few changes, I decided that this section also made a valuable addition to the dissertation. I've included operational information about our current equipment, simple Hall effect theory, and explanations for the advantages and disadvantages of certain measurement techniques. I hope this section will prove beneficial to those who come across it.

A.2 Hall Effect Equipment

The Hall effect was discovered by Edwin Hall in 1879 and has become a powerful tool for the characterization of electronic materials. The charge carrier type, concentration, and mobility can all be determined from accurate Hall measurements.

Most of the resistivity and Hall effect measurements in this thesis were performed using a Keithley high-impedance Hall effect system. Control over the temperature and magnetic field was accomplished by placing samples inside a Quantum Design (QD) Physical Property Measurement System (PPMS). The PPMS is a versatile tool for probing various material properties. Equipment options are available for measuring a sample's magnetic, electric, and thermal properties in the same piece of equipment. The PPMS's open architecture also allows room for user customization and other tools may be integrated into the system. For instance, customizable probe heads allow the introduction of extra signal cables or optical feedthrus into the sample arena. The PPMS acts as a platform, or a "measurement environment", to control the ambient temperature and field around the sample. The temperature of our system can be adjusted from 1.4K–400K, and there is a longitudinal superconducting magnet that can be swept to a maximum of ± 7 Tesla. The PPMS is a helium filled system. The helium is used

for cooling the sample space to low temperature and also keeps the magnet below its superconducting critical temperature. The helium bath is surrounded by a nitrogen filled jacket that reduces the helium boil-off. At low temperatures, the sample chamber must be pumped to prevent freezing of atmospheric gases in the system. This is controlled through an integrated gas handling system. There are packaged options for both DC resistance and AC transport measurements available from QD. However, some of the samples produced in our lab are highly resistive, >100 MΩ, and our current PPMS resistivity options can not support samples of such large resistance. Measuring transport properties on these materials required the use of separate electronics. A high-impedance Hall effect configuration using Keithley components was used, including a 236 Source Measurement Unit (SMU), two 6514 Electrometers, and a 7152 4x5 matrix switch card housed in a 7001 switching mainframe. A diagram of the equipment is give in Figure A-1. For consistency and convenience, the external electronics were used for most of the measurements in this work, even for samples that could be easily measured by the internal PPMS electronics. Integration and control over the PPMS and Keithley electronics was accomplished using the LabView programming language. LabView was used to program the automated resistivity and Hall routines, which included programs for Van der Pauw and Hall bridge samples, magnetic field and temperature sweeps, and time dependent measurements. If necessary, LabView also provides flexibility for creating new routines for future experiments.

Samples are mounted to pucks that can accommodate sample sizes up to 1cm x 1cm square. There are 12 available signal wires fed to the sample space that may be used for measurements. For example, the standard QD resistivity puck allows up to three samples configured for 4pt. measurements to be measured simultaneously through the 12 signal leads (4 leads are used for each of the three samples). Access to these wires from outside the system is granted through a Lemo connector.

The Keithley high-impedance Hall effect system is shown in Figure A-1. This section will provide a brief description of the equipment used and the reasons behind their selection. The basic premise of an electrical measurement is to provide a known stimulus to a sample and to measure the sample's response to that stimulus. For instance, a basic resistivity measurement may be made by applying a known current to a sample, measuring the subsequent potential difference, and calculating the sample's resistance by using Ohm's law. As with most scientific measurements, accuracy is of prime concern. Various internal and external factors can effect the accuracy of electrical measurements. These include error sources from the experimental set-up, including leakage currents, ground loops, equipment offset voltages and currents, and environmental noise. The sample itself will also provide sources of error, such as thermal Johnson noise, non-ohmic contacts, and photovoltaic effects. Some of these errors can be significantly reduced by the proper choice of equipment and measurement procedure.

The Keithley 236 SMU contains both source and measurement capabilities in one unit. The SMU is used to drive current into the sample and measure the voltage difference created. The 236 provides a current range of 100fA to 100mA providing flexibility for samples of various resistance. Both the source and sense leads pass through the 7152 switch card. The 7152 provides automated switching of the signal cables between the 4 sample contacts through a grid of interconnected relays. This can be seen in the switch card diagram included in Figure A-1. Each crossing point of the grid represents a relay that can be opened or closed to redirect the cabling to each sample contact point. These relays also switch the guard conductors. Switch cards eliminate the need to physically reconfigure the sample contacts for each leg of the Van der Pauw routine. The high and low signal voltages generated in the sample are sent to the Keithley 6514 electrometers. These electrometers have a huge input impedance (>200 TΩ) which reduces input loading errors on high resistance samples. In our set-up, the two electrometers act as unity gain buffers between the sample and the SMU voltmeter. The unity gain buffer is an amplifier

circuit that duplicates the input voltage at the output terminal of the amplifier. The voltage gain is unity ($\frac{V_o}{V_{in}}$=1). Since the buffer's input impedance is large it can replicate the voltage without drawing any current from the source. Ideally, voltage measurements draw zero current [153]. In fact, any current at the voltmeter input represents an error, called the input offset current. This is the advantage of placing a buffer amplifier (the electrometers) in the circuit. The output from the electrometers is then read by the SMU's voltmeter for measurement.

A.3 Sample Geometry and Measurement Technique

The two common sample geometries for Hall measurements are Hall bridge and Van der Pauw samples. While the exact dimensions of Hall bridge samples are needed for accurate data, the Van der Pauw technique allows samples of arbitrary shape and size. Both measurement techniques are described in the ASTM standard F76-86 "Standard Test Methods for Measuring Resistivity and Hall Coefficient and Determining Hall Mobility in Single-Crystal Semiconductors". Included in the ASTM standard are specifications for sample geometries and the mathematical equations used to calculate the material's electrical properties. Both types of sample geometries were used in this work. The LabView programs used to drive the measurement routines were based on the information provided in the ASTM standard. This section will give a brief explanation of the advantages and disadvantages of each measurement.

Resistivity measurements can be performed using a 2pt. method, where only 2 leads are connected to the sample, by shorting a voltmeter across the same leads used to drive current through the sample. A diagram for the 2pt. configuration is provided in Figure A-2. The drawback of 2pt. measurements is that, in addition to the sample resistance, the voltage drop across the contact and lead resistances are also measured by the voltmeter. This can cause serious loading errors if the contact and cable resistance is larger than the sample resistance. A more accurate approach requires 4 contacts to the sample. Current is driven into the sample through two leads and the voltage is measured across

the other two. Ideally, no current flows across the voltmeter, but this depends on the input resistance of the meter. Quality voltmeters have a large input resistance (10MΩ–10GΩ) to reduce the input offset current. Hall bridge samples are measured using the 4pt. contact method. Current is sourced between the two longitudinal contacts and the voltage is measured between two contacts situated parallel to the current direction. The hall voltage is measured across two contacts that are placed perpendicular to the current direction.

The Van der Pauw technique was first proposed by L.J. Van der Pauw in 1958. The technique is widely used since it provides a convenient method for probing the transport properties of materials. The Van der Pauw technique's primary advantage is that contacts may be placed arbitrarily around the sample perimeter. This enables samples of arbitrary shape and size to be measured directly. The need to fabricate complex sample geometries or detailed knowledge of the sample dimensions is eliminated. Only knowledge of the thickness is needed to calculate the volume resistivity and carrier density from their respective 2-dimensional sheet values. This can be highly beneficial in certain cases, such as when the sample material is difficult to process or when the facilities and/or the time for processing samples is not available.

There are several disadvantages to the Van der Pauw technique. There are errors associated with contact size effects and shorting of the Hall voltage [154]. Ideally, contacts should be kept as small as possible. As mentioned above, the Van der Pauw technique allows arbitrary placement of contacts to determine the resistivity of the sample. On the contrary, this is not true for the Hall voltage. Misalignment of the voltage leads will cause additional error. Deviations from perpendicular alignment with the applied current can cause mixing of the perpendicular and parallel components of the created voltage. This distorts the true Hall voltage being measured. Note that this is also true for Hall bridge samples; however, the fixed geometry of the bridge limits the misalignment. Current-reversal averaging techniques (described later) can help alleviate misalignment error. Another drawback of the technique is measurement time. Van der Pauw requires a

total of 8 voltage measurements around the sample—each side of the sample is measured under positive and negative current polarities—whereas a hall bridge patterned sample only requires 2 measurements. This can be especially problematic when long delay times are needed for the circuit to settle, such as when measuring high resistance samples. Settling time is a function of the RC time constant. It represents the time needed to saturate any shunt capacitance in the circuit to obtain an accurate measurement of the circuit voltage. This idea is represented in figure A-3. The Van der Pauw technique also requires a switching system if leads are hard wired to the sample. This system can be manual or automatic, and is used to reconfigure the current and voltage leads around the sample without having to remove and replace each sample contact during the measurement.

Small signal currents are needed to make measurements on high resistance sources. During Hall and resistivity measurements, ohmic heating in the sample should be kept to a minimum to retain measurement accuracy and reduce thermal noise. Since power is equal to resistance multiplied by the square of the current ($P=I^2R$), low currents are needed to keep the power dissipation low. Typically, keeping the power in the sample below 1-5 mW is suggested for general transport measurements. Leakage currents—currents that 'leak' into or out of the circuit through unwanted resistive pathways—can degrade the accuracy of low current measurements [153]. This can be a common error in low-level measurements using standard cables, where portions of the signal current can leak through the cable's insulation resistance. Use of a guarding technique with triaxial cables can reduce leakage currents. Triaxial cables contain an extra conductor that surrounds the signal cable (separated by an insulator) and lies underneath the ground sheath of the cable. A potential is driven along the guard that matches the potential on the signal cable. This creates a space of zero potential between the guard and signal and reduces the driving force for current leakage between them. The leakage current combined with the input offset current represents the total error current of the circuit

[153]. The open-loop gain of the guard also reduces the effects of cable capacitance by reducing the shunt capacitance charging time [153]. The Keithley electronics support the use of guarding and the equipment is connected using triaxial cables. However, the PPMS does not use triaxial cabling which poses a limitation of using guarded measurements with the current set-up (see the following sections for more details).

A.4 Hall Effect Method

The physics of the Hall effect can be found in almost any solid-state physics or electronic materials science book, as well as plenty of sources on the world wide web. It's not my intention of rehashing this information since it is easily found, but only to provide the basic ideas and equations for the measurement. The driving force behind the Hall effect is the Lorentz force acting between moving charge carriers and a magnetic-field applied perpendicular to the carrier's velocity. The Lorentz force is given by:

$$F = -q(\vec{v}x\vec{B}) \tag{A–1}$$

where q is the carrier charge (1.602x10^{-19} for electrons and holes), $\vec{v}$ is the carrier velocity, and $\vec{B}$ is the magnetic induction.

A current is applied to one end of the sample and carriers are driven through the length of the sample. The magnetic-field is applied perpendicular to the carrier velocity and pushes the carriers towards the edge of the sample as dictated by the Lorentz force. This results in a slight charge imbalance between the two sample edges. To maintain the flow of current, the charge imbalance creates a potential drop across the sample to balance the Lorentz force. This is the Hall voltage, V_H, and is given by:

$$V_H = \frac{I \times B_z}{n \times q \times t} \tag{A–2}$$

where n is the carrier concentration, t is the sample thickness, and I is the applied current. If the sample resistance is known, the carrier mobility, μ, can be calculated:

$$\mu = \frac{R_H}{n} \tag{A–3}$$

where R_H^{-1}=nq is defined as the Hall coefficient.

However, if the sample under consideration is composed of two carriers, such as a semiconductor with a sufficient number of electrons and holes in the material, a two carrier model for the Hall coefficient is more appropriate [154]:

$$R_H = \frac{p\mu_p^2 - n\mu_n^2}{e\left(p\mu_p + n\mu_n\right)^2} \tag{A–4}$$

Taking Hall voltages at three magnetic-field points (+H_1, H=0, and -H_1, where H_1 is some value of magnetic field) is usually sufficient to determine the Hall coefficient. The two measurements at $\pm H_1$ are used to average over both field polarities and the measurement at H=0 can be used calculate the carrier mobility. However, I have found it extremely beneficial to measure Hall voltages at many points over a full magnetic-field sweep. Since the Hall coefficient is proportional to the quotient of V_H/B, the coefficient can be calculated from the slope of a line fit through the data. This provides a better statistical average, averaging over many points rather than just three, and the accuracy of the data is easily examined based on how well the points follow a linear path. This proved particularly useful for difficult samples which exhibit weak Hall voltages that stagger between n- and p-type (positive and negative slope). Taking Hall measurements at varying-fields is also necessary for studying the anomalous Hall effect (AHE) in magnetic samples. In fact, sensitive magnetic properties can even be determined in samples that show a large AHE component.

A.5 Limitations and Tips for Better Measurements

There are several limitations of the current set-up that could use refinement. The main difficulty we have experienced is measuring Hall voltages on our p-type ZnO films. The doped holes in these materials are highly compensated by the intrinsic electron concentration, and both carrier types are present in the material. The Hall coefficient

for this condition was given above. The mobility of holes in these materials is small, and the condition for p-type material, $p\mu_p^2 > n\mu_n^2$, is difficult to fulfill. These samples produce a very weak Hall voltage, even at fields of 7T, and are extremely difficult to measure accurately. The electrometers have a resolution of 10 μV, which does not provide enough sensitivity for measuring the weak Hall voltage. Typically measurements are noisy and teeter between n- and p-type conductivity. Replacing the electrometer with a more sensitive voltmeter, such as a nanovoltmeter with nanovolt sensitivity, may provide enhanced measurement accuracy for these difficult samples.

The 236 SMU is a convenient tool because it provides sourcing and measuring capabilities in one cost-effective unit. However, this also provides a slight limitation when measuring highly-resistive samples. The SMU is not capable of performing measurements in 4 terminal mode when the potential difference between the source and sense leads exceeds 4 volts. This is easily seen during a measurement because every Van der Pauw voltage measurement around the sample converges to the same value. Whenever this was encountered, a digital multimeter was borrowed from another piece of equipment to perform the measurements. Since the other DMM was isolated from the SMU, this problem could be alleviated.

An additional limitation comes from interfacing the external Keithley electronics to the sample inside the PPMS. The wires inside the PPMS that connect the external port on the PPMS to the sample fixture are not triaxial. Therefore a discontinuity exists between the guarded triaxial cables from the Keithley electronics to the sample fixture—the guard is not carried all the way to the sample. Currently, the discontinuity in cable type occurs at a custom-made junction box. The guards terminate at the junction box, where only the center conductor (the portion carrying the signal) is carried to the PPMS cabling. Creating a PPMS probe that uses triaxial cables and carries the guard all the way to the sample should provide further measurement accuracy for samples that are difficult to measure.

Misalignment in the sample contacts can add spurious values to the measured voltages due to mixing of the parallel and perpendicular voltage components. A simple way to help separate the two components is by field averaging the collected data. The magnetoresistance of a sample will be an even function of the applied field. So the curve produced should have mirror symmetry reflected across the y-axis on a resistivity vs. field plot. Therefore, the magnetoresistance can be averaged by $R_{xx} = \frac{1}{2}$ [R_{xx}(+H) + R_{xx}(-H)]. On the contrary, the Hall resistivity is an odd function of field, which produces symmetry through the origin. Odd symmetry produces graphs that are unchanged after a 180 degree rotation around the origin. The Hall data can be averaged by $R_{xy} = \frac{1}{2}$[R_H(+H) - R_H(-H)]. These averaging techniques can be used for both single field sweeps and hysteretic sweeps, where the field is swept in one direction and then swept back in the reverse direction. When averaging the hysteretic sweeps it is advisable to average the initial downward sweep with the ascending return sweep and vice-versa [155]. While these simple averaging schemes can aid in separating the two components, the data may still be skewed if one component is much larger than the other.

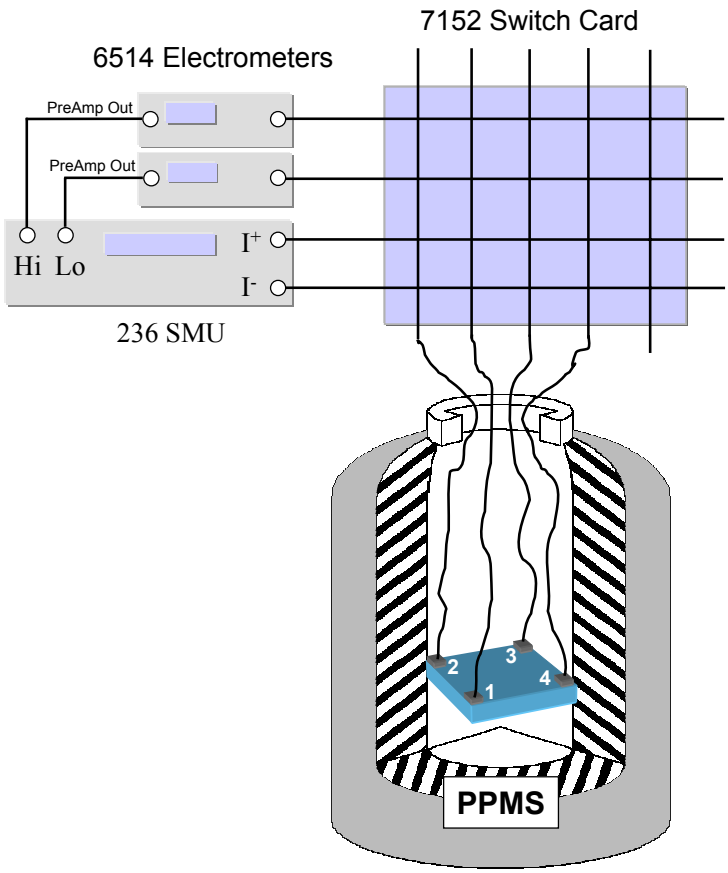

Figure A-1. The resistivity and Hall measurement system. The sample is placed inside the PPMS dewar to control the ambient temperature and magnetic field. The electrical data is collected with external Keithley electronics.

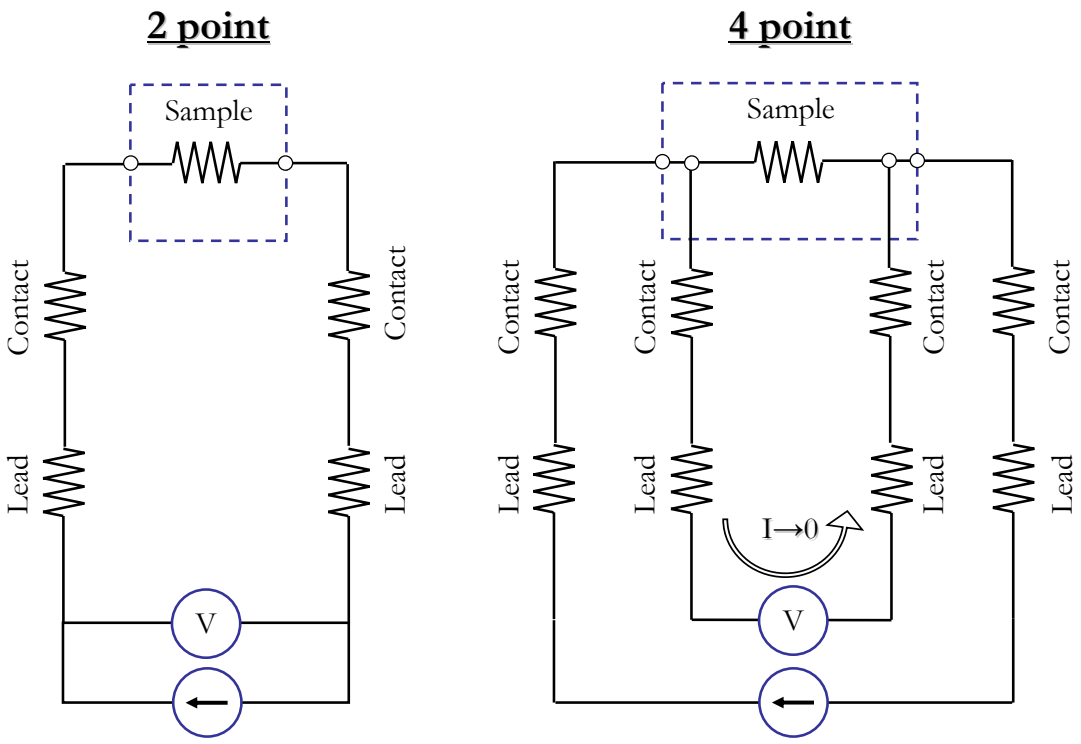

Figure A-2. Circuit diagrams for 2-point and 4-point resistivity measurements. In a 2pt. measurement, the contact and lead resistance are measured by the voltmeter. In a 4pt. measurement, the current through the voltmeter approaches zero, so only the sample voltage is measured.

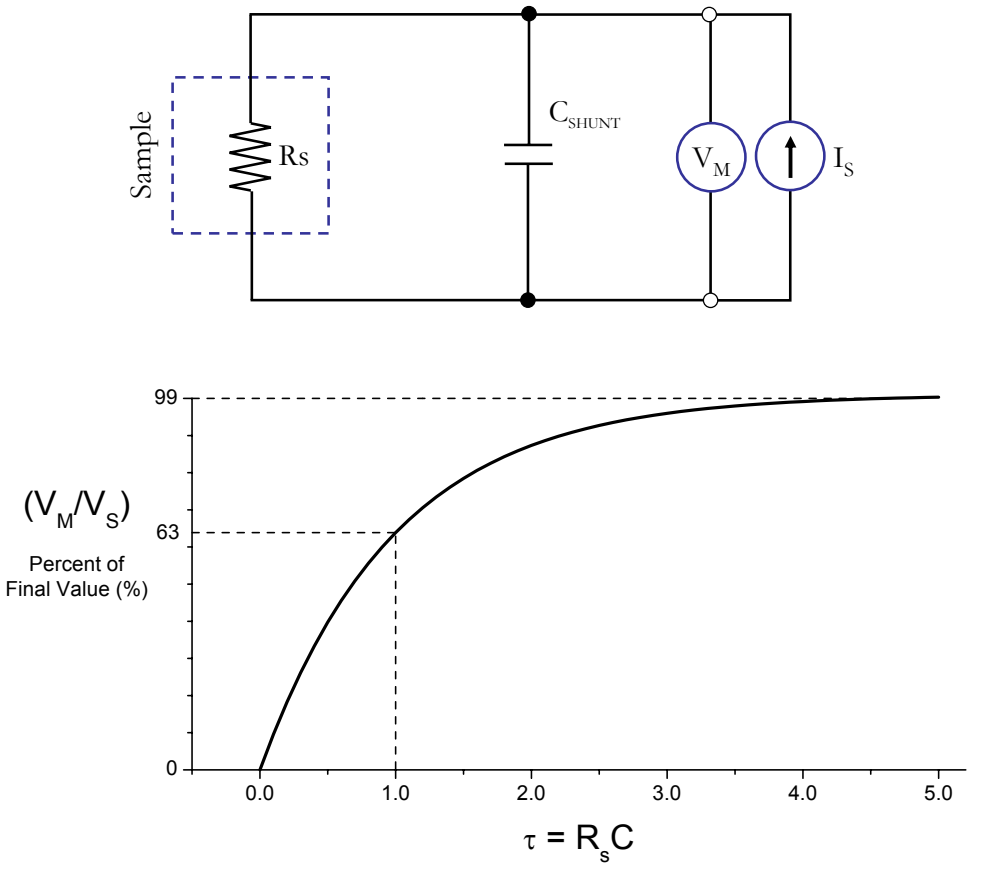

Figure A-3. Circuit shunt capacitance and settling time. The circuit shunt capacitance that must be fully charged before an accurate measurement of the circuit voltage, Vm, is possible. The graph shows the settling time necessary to reach a certain percentage of the final voltage. The settling time is given as multiples of the circuit's RC time constant. Adapted from [153].

REFERENCES

[1] "Introducing the 45nm next generation intel core microarchitecture," *Technology@Intel Magazine*, vol. 4, no. 10, pp. June 20, 2007, May 2007 2007.

[2] "Perpendicular recording: Powering new levels of disc drive capacity," Tech. Rep. TP-549, Seagate Technology, February 2006 2006.

[3] F. Liu, K. Stoev, P. Luo, Y. Liu, Y. Chen, J. Chen, J. Wang, S. F. Gu, K. T. Kung, M. Lederman, M. Krounbi, M. Re, A. Otsuki, and S. Hong, "Perpendicular recording heads for extremely high-density recording," *IEEE Transactions on Magnetics*, vol. 39, no. 4, pp. 1942–1948, 2003.

[4] M. H. Kryder, "Magnetic recording beyond the superparamagnetic limit," in *2000 IEEE International Magnetics Conference-2000 IEEE INTERMAG*, Toronto, Ont, Can, Apr 9-Apr 13 2000 2000, Seagate Research, Pittsburgh, PA, USA, pp. –01, Institute of Electrical and Electronics Engineers Inc., Piscataway, NJ, USA.

[5] S. Khizroev, Y. Hijazi, N. Amos, R. Chomko, and D. Litvinov, "Physics considerations in the design of three-dimensional and multilevel magnetic recording," *Journal of Applied Physics*, vol. 100, no. 6, pp. 063907, 2006.

[6] G. A. Prinz, "Spin-polarized transport," *Physics Today*, pp. 58–63, April 1995 1995.

[7] G. A. Prinz, "Magnetoelectronics," *Science*, vol. 282, no. 5394, pp. 1660–1663, 1998.

[8] S. A. Wolf, A. Y. Chtchelkanova, and D. M. Treger, "Spintronics - a retrospective and perspective," *IBM Journal of Research and Development*, vol. 50, pp. 101–110, 2006.

[9] S. A. Wolf, D. Treger, and A. Chtchelkanova, "Spintronics: The future of data storage?," *MRS Bulletin*, vol. 31, pp. 400–403, 2006.

[10] S. A. Wolf, D. D. Awschalom, R. A. Buhrman, J. M. Daughton, S. V. Molnar, M. L. Roukes, A. Y. Chtchelkanova, and D. M. Treger, "Spintronics: A spin-based electronics vision for the future," *Science*, vol. 294, no. 5546, pp. 1488–1495, 2001.

[11] G. Schmidt, D. Ferrand, L. W. Molenkamp, A. T. Filip, and B. J. van Wees, "Fundamental obstacle for electrical spin injection from a ferromagnetic metal into a diffusive semiconductor," *Phys.Rev.B*, vol. 62, no. 8, pp. R4790–R4793, Aug 2000.

[12] C. Haas, "Magnetic semiconductors," *Critical Reviews in Solid State and Materials Sciences*, vol. 1, no. 1, pp. 47, 1970.

[13] H. Ohno, "Making nonmagnetic semiconductors ferromagnetic," *Science*, vol. 281, no. 5379, pp. 951–956, 1998.

[14] J. K. Furdyna, "Diluted magnetic semiconductors," *Journal of Applied Physics*, vol. 64, no. 4, pp. R29–R64, August 15, 1988 1988.

[15] A. Haury, A. Wasiela, A. Arnoult, J. Cibert, S. Tatarenko, T. Dietl, and Y. M. d'Aubigne, "Observation of a ferromagnetic transition induced by two-dimensional hole gas in modulation-doped cdmnte quantum wells," *Physical Review Letters*, vol. 79, no. 3, pp. 511–514, 1997.

[16] H. Ohno, H. Munekata, S. von Molnar, and L. L. Chang, "New iii-v diluted magnetic semiconductors (invited)," *35th annual conference on magnetism and magnetic materials*, vol. 69, no. 8, pp. 6103–6108, April 15, 1991 1991.

[17] S. Koshihara, A. Oiwa, M. Hirasawa, S. Katsumoto, Y. Iye, C. Urano, H. Takagi, and H. Munekata, "Ferromagnetic order induced by photogenerated carriers in magnetic iii-v semiconductor heterostructures of (in,mn)as/gasb," *Physical Review Letters*, vol. 78, no. 24, pp. 4617–4620, Jun 1997.

[18] H. Munekata, H. Ohno, S. von Molnar, A. Segmuller, L. L. Chang, and L. Esaki, "Diluted magnetic iii-v semiconductors," *Physical Review Letters*, vol. 63, no. 17, pp. 1849–1852, Oct 1989.

[19] Y. Ohno, D. K. Young, B. Beschoten, F. Matsukura, H. Ohno, and D. D. Awschalom, "Electrical spin injection in a ferromagnetic semiconductor heterostructure," *Nature*, vol. 402, no. 6763, pp. 790–792, DEC 16 1999.

[20] A. M. Nazmul, S. Kobayashi, S. Sugahara, and M. Tanaka, "Electrical and optical control of ferromagnetism in iii-v semiconductor heterostructures at high temperature ([similar to] 100k)," *Japanese Journal of Applied Physics, Part 2: Letters*, vol. 43, no. 2, pp. 233–236, 2004.

[21] T. Dietl, H. Ohno, F. Matsukura, J. Cibert, and D. Ferrand, "Zener model description of ferromagnetism in zinc-blende magnetic semiconductors," *Science*, vol. 287, no. 5455, pp. 1019–1022, 2000.

[22] S. J. Pearton, C. R. Abernathy, D. P. Norton, A. F. Hebard, Y. D. Park, L. A. Boatner, and J. D. Budai, "Advances in wide bandgap materials for semiconductor spintronics," *Materials Science and Engineering R: Reports*, vol. 40, no. 4, pp. 137, 2003.

[23] H. Ohno and F. Matsukura, "A ferromagnetic iiiv semiconductor: (ga,mn)as," *Solid State Communications*, vol. 117, no. 3, pp. 179–186, 2001.

[24] T. Dietl, "Ferromagnetic semiconductors," *Semiconductor Science and Technology*, vol. 17, no. 4, pp. 377–392, 2002.

[25] H. Katayama-Yoshida and K. Sato, "Materials design for semiconductor spintronics by ab initio electronic-structure calculation," *Physica B: Condensed Matter*, vol. 327, no. 2-4, pp. 337–343, 2003/4.

[26] K. Sato and H. Katayama-Yoshida, "First principles materials design for semiconductor spintronics," *Semiconductor Science and Technology*, vol. 17, no. 4, pp. 367–376, 2002.

[27] K. Sato and H. Katayama-Yoshida, "Material design for transparent ferromagnets with zno-based magnetic semiconductors," *Japanese Journal of Applied Physics, Part 2: Letters*, vol. 39, no. 6B, pp. 555–558, 2000.

[28] M. Berciu and R. N. Bhatt, "Effects of disorder on ferromagnetism in diluted magnetic semiconductors," *Physical Review Letters*, vol. 87, no. 10, pp. 107203–1, 2001.

[29] P. A. Wolff, R. N. Bhatt, and A. C. Durst, "Polaron-polaron interactions in diluted magnetic semiconductors," *Journal of Applied Physics*, vol. 79, no. 8, pp. 5196–5198, 1996.

[30] A. Kaminski and S. D. Sarma, "Polaron percolation in diluted magnetic semiconductors," *Physical Review Letters*, vol. 88, no. 24, pp. 247202–1, 2002.

[31] J. M. D. Coey, M. Venkatesan, and C. B. Fitzgerald, "Donor impurity band exchange in dilute ferromagnetic oxides," *Nature Materials*, vol. 4, no. 2, pp. 173–179, 2005.

[32] K. R. Kittilstved, W. K. Liu, and D. R. Gamelin, "Electronic structure origins of polarity-dependent high-tc ferromagnetism in oxide-diluted magnetic semiconductors," *Nature Materials*, vol. 5, no. 4, pp. 291–297, 2006/04/ 2006.

[33] R. Janisch, P. Gopal, and N. A. Spaldin, "Transition metal-doped tio2 and zno - present status of the field," *Journal of Physics Condensed Matter*, vol. 17, no. 27, pp. R657–R689, 2005.

[34] C. Liu, F. Yun, and H. Morkoc, "Ferromagnetism of zno and gan: A review," *Journal of Materials Science: Materials in Electronics*, vol. 16, no. 9, pp. 555–597, 2005.

[35] S. A. Chambers, "Ferromagnetism in doped thin-film oxide and nitride semiconductors and dielectrics," *Surface Science Reports*, vol. 61, no. 8, pp. 345–381, 2006.

[36] S. J. Pearton, D. P. Norton, M. P. Ivill, A. F. Hebard, J. M. Zavada, W. M. Chen, and I. A. Buyanova, "Zno doped with transition metal ions," *IEEE Transactions on Electron Devices*, vol. 54, no. 5, pp. 1040–1048, 2007.

[37] T. Fukumura, Z. Jin, A. Ohtomo, H. Koinuma, and M. Kawasaki, "An oxide-diluted magnetic semiconductor: Mn-doped zno," *Applied Physics Letters*, vol. 75, no. 21, pp. 3366–3368, 1999.

[38] T. Fukumura, Z. Jin, M. Kawasaki, T. Shono, T. Hasegawa, S. Koshihara, and H. Koinuma, "Magnetic properties of mn-doped zno," *Applied Physics Letters*, vol. 78, no. 7, pp. 958–960, 2001.

[39] P. Sharma, A. Gupta, K. V. Rao, F. J. Owens, R. Sharma, R. Ahuja, J. M. O. Guillen, B. Johansson, and G. A. Gehring, "Ferromagnetism above room temperature in bulk and transparent thin films of mn-doped zno," *Nature Materials*, vol. 2, no. 10, pp. 673–677, 2003.

[40] D. C. Kundaliya, S. B. Ogale, S. E. Lofland, S. Dhar, C. J. Metting, S. R. Shinde, Z. Ma, B. Varughese, K. V. Ramanujachary, L. Salamanca-Riba, and T. Venkatesan, "On the origin of high-temperature ferromagnetism in the low-temperature-processed mn-zn-o system," *Nature Materials*, vol. 3, no. 10, pp. 709–714, 2004.

[41] X. M. Cheng and C. L. Chien, "Magnetic properties of epitaxial mn-doped zno thin films," *Journal of Applied Physics*, vol. 93, no. 10, pp. 7876–7878, 2003.

[42] Z.-W. Jin, Y. Z. Yoo, T. Sekiguchi, T. Chikyow, H. Ofuchi, H. Fujioka, M. Oshima, and H. Koinuma, "Blue and ultraviolet cathodoluminescence from mn-doped epitaxial zno thin films," *Applied Physics Letters*, vol. 83, no. 1, pp. 39–41, July 7, 2003 2003.

[43] K. Ueda, H. Tabata, and T. Kawai, "Magnetic and electric properties of transition-metal-doped zno films," *Applied Physics Letters*, vol. 79, no. 7, pp. 988, 2001.

[44] S. Ramachandran, A. Tiwari, and J. Narayan, "Zn0.9co0.1o-based diluted magnetic semiconducting thin films," *Applied Physics Letters*, vol. 84, no. 25, pp. 5255–5257, June 21, 2004 2004.

[45] C. B. Fitzgerald, M. Venkatesan, J. G. Lunney, L. S. Dorneles, and J. M. D. Coey, "Cobalt-doped zno a room temperature dilute magnetic semiconductor," *Applied Surface Science*, vol. 247, no. 1-4, pp. 493–496, 2005/7/15 2005.

[46] J. H. Park, M. G. Kim, H. M. Jang, S. Ryu, and Y. M. Kim, "Co-metal clustering as the origin of ferromagnetism in co-doped zno thin films," *Applied Physics Letters*, vol. 84, no. 8, pp. 1338–1340, February 23, 2004 2004.

[47] Z. Jin, T. Fukumura, M. Kawasaki, K. Ando, H. Saito, T. Sekiguchi, Y. Z. Yoo, M. Murakami, Y. Matsumoto, T. Hasegawa, and H. Koinuma, "High throughput fabrication of transition-metal-doped epitaxial zno thin films: A series of oxide-diluted magnetic semiconductors and their properties," *Applied Physics Letters*, vol. 78, no. 24, pp. 3824–3826, June 11, 2001 2001.

[48] D. A. Schwartz and D. R. Gamelin, "Reversible 300 k ferromagnetic ordering in a diluted magnetic semiconductor," *Advanced Materials*, vol. 16, no. 23, pp. 2115–2119, 2004.

[49] K. R. Kittilstved, N. S. Norberg, and D. R. Gamelin, "Chemical manipulation of high-tc ferromagnetism in zno diluted magnetic semiconductors," *Physical Review Letters*, vol. 94, no. 14, pp. 147209, 2005.

[50] S. J. Pearton, W. H. Heo, M. Ivill, D. P. Norton, and T. Steiner, "Dilute magnetic semiconducting oxides.," *Semiconductor Science and Technology*, vol. 19, no. 10, pp. R59–R74, 2004.

[51] J. H. Kim, H. Kim, D. Kim, Y. E. Ihm, and W. K. Choo, "Magnetic properties of epitaxially grown semiconducting zn1-xcoxo thin films by pulsed laser deposition," *Journal of Applied Physics*, vol. 92, no. 10, pp. 6066–6071, 2002.

[52] S.-W. Lim, M.-C. Jeong, M.-H. Ham, and J.-M. Myoung, "Hole-mediated ferromagnetic properties in zn1-xmnxo thin films," *Japanese Journal of Applied Physics, Part 2: Letters*, vol. 43, no. 2, pp. 280–283, 2004.

[53] T. Wakano, N. Fujimura, Y. Morinaga, N. Abe, A. Ashida, and T. Ito, "Magnetic and magneto-transport properties of zno: Ni films," *Physica E: Low-Dimensional Systems and Nanostructures*, vol. 10, no. 1, pp. 260–264, 2001.

[54] H. Saeki, H. Tabata, and T. Kawai, "Magnetic and electric properties of vanadium doped zno films," *Solid State Communications*, vol. 120, no. 11, pp. 439–443, 2001.

[55] Y. M. Cho, W. K. Choo, H. Kim, D. Kim, and Y. Ihm, "Effects of rapid thermal annealing on the ferromagnetic properties of sputtered zn1-x(co0.5fe0.5)xo thin films," *Applied Physics Letters*, vol. 80, no. 18, pp. 3358–3360, 2002.

[56] D. P. Norton, M. E. Overberg, S. J. Pearton, K. Pruessner, J. D. Budai, L. A. Boatner, M. F. Chisholm, J. S. Lee, Z. G. Khim, Y. D. Park, and R. G. Wilson, "Ferromagnetism in cobalt-implanted zno," *Applied Physics Letters*, vol. 83, no. 26, pp. 5488–5490, 2003.

[57] S. J. Han, J. W. Song, C. H. Yang, S. H. Park, J. H. Park, Y. H. Jeong, and K. W. Rhie, "A key to room-temperature ferromagnetism in fe-doped zno: Cu," *Applied Physics Letters*, vol. 81, no. 22, pp. 4212–4214, 2002.

[58] S. W. Jung, S. J. An, G.-C. Yi, C. U. Jung, S.-I. Lee, and S. Cho, "Ferromagnetic properties of zn1-xmnxo epitaxial thin films.," *Applied Physics Letters*, vol. 80, no. 24, pp. 4561–4563, 2002.

[59] P. Sharma, A. Gupta, F. J. Owens, A. Inoue, and K. V. Rao, "Room temperature spintronic material - mn-doped zno revisited," in *International Symposium on Advanced Magnetic Technologies*, Taipei, Taiwan, Nov 13-16 2003 2004, Japan Science and Technology Agency, Sendai 980-8577, Japan, vol. 282, pp. 115–121, Elsevier, Amsterdam, 1000 AE, Netherlands.

[60] M. Venkatesan, C. B. Fitzgerald, J. G. Lunney, and J. M. D. Coey, "Anisotropic ferromagnetism in substituted zinc oxide," *Physical Review Letters*, vol. 93, no. 17, pp. 177206–1, 2004.

[61] K. Rode, A. Anane, R. Mattana, J. P. Contour, O. Durand, and R. LeBourgeois, "Magnetic semiconductors based on cobalt substituted zno," *Journal of Applied Physics*, vol. 93, no. 10, pp. 7676–7678, 2003.

[62] S. G. Yang, A. B. Pakhomov, S. T. Hung, and C. Y. Wong, "Room temperature magnetism in sputtered (zn,co)o films," in *2002 International Magnetics Conference (Intermag 2002)*, Amsterdam, Netherlands, Apr 28-May 2 2002 2002, Magnetics Innovation Center, Mat. Characterization/Prep. Facil., Hong Kong Univ. of Sci. and Technol., Kowloon, Hong Kong, vol. 38, pp. 2877–2879, Institute of Electrical and Electronics Engineers Inc.

[63] D. P. Norton, S. J. Pearton, A. F. Hebard, N. Theodoropoulou, L. A. Boatner, and R. G. Wilson, "Ferromagnetism in mn-implanted zno:sn single crystals," *Applied Physics Letters*, vol. 82, no. 2, pp. 239–241, 2003.

[64] M. Ivill, S. J. Pearton, D. P. Norton, J. Kelly, and A. F. Hebard, "Magnetization dependence on electron density in epitaxial zno thin films codoped with mn and sn," *Journal of Applied Physics*, vol. 97, no. 5, pp. 053904, 2005.

[65] G. Lawes, A. S. Risbud, A. P. Ramirez, and R. Seshadri, "Absence of ferromagnetism in co and mn substituted polycrystalline zno," *Physical Review B (Condensed Matter and Materials Physics)*, vol. 71, no. 4, pp. 045201, January 15, 2005 2005.

[66] M. H. Kane, K. Shalini, C. J. Summers, R. Varatharajan, J. Nause, C. R. Vestal, Z. J. Zhang, and I. T. Ferguson, "Magnetic properties of bulk zn1-x mnx o and zn1-x cox o single crystals," *Journal of Applied Physics*, vol. 97, no. 2, pp. 023906–1, 2005.

[67] A. C. Tuan, J. D. Bryan, A. B. Pakhomov, V. Shutthanandan, S. Thevuthasan, D. E. McCready, D. Gaspar, M. H. Engelhard, J. R. J.W., K. Krishnan, D. R. Gamelin, and S. A. Chambers, "Epitaxial growth and properties of cobalt-doped zno on alpha-al2o3 single-crystal substrates," *Physical Review B (Condensed Matter and Materials Physics)*, vol. 70, no. 5, pp. 054424, August 1, 2004 2004.

[68] T. Fukumura, H. Toyosaki, and Y. Yamada, "Magnetic oxide semiconductors," *Semiconductor Science and Technology*, vol. 20, no. 4, pp. 103–111, 2005.

[69] N. H. Hong, V. Briz, and J. Sakai, "Mn-doped zno and (mn, cu)-doped zno thin films: Does the cu doping indeed play a key role in tuning the ferromagnetism?," *Applied Physics Letters*, vol. 86, no. 8, pp. 082505, 2005.

[70] N. H. Hong, J. Sakai, and A. Hassini, "Magnetism in v-doped zno thin films," *Journal of Physics Condensed Matter*, vol. 17, no. 1, pp. 199–204, 2005.

[71] I. Satoh and T. Kobayashi, "Magnetic and optical properties of novel magnetic semiconductor cr-doped zno and its application to all oxide p-i-n diode," *Applied Surface Science*, vol. 216, no. 1, pp. 603–606, 2003.

[72] R. K. Zheng, H. Liu, X. X. Zhang, V. A. L. Roy, and A. B. Djurisic, "Exchange bias and the origin of magnetism in mn-doped zno tetrapods," *Applied Physics Letters*, vol. 85, no. 13, pp. 2589–2591, 2004.

[73] K. W. Nielsen, J. B. Philipp, M. Opel, A. Erb, J. Simon, L. Alff, and R. Gross, "Ferromagnetism in mn-doped zno due to impurity bands," *Superlattices and Microstructures*, vol. 37, no. 5, pp. 327–332, 2005.

[74] M. A. Garcia, M. L. Ruiz-Gonzalez, A. Quesada, J. L. Costa-Kramer, J. F. Fernandez, S. J. Khatib, A. Wennberg, A. C. Caballero, M. S. Martin-Gonzalez, M. Villegas, F. Briones, J. M. Gonzalez-Calbet, and A. Hernando, "Interface double-exchange ferromagnetism in the mn-zn-o system: New class of biphase magnetism," *Physical Review Letters*, vol. 94, no. 21, pp. 217206, 2005.

[75] J. J. Dubowski, "Pulsed laser evaporation and epitaxy of thin semiconductor films," *Chemtronics*, vol. 3, no. 2, pp. 66–76, 1988.

[76] D. H. Lowndes, *Growth and Doping of Compound Semiconductor Films by Pulsed Laser Ablation*, vol. 30 of *Laser Ablation and Desorption*, chapter 11, pp. 475–571, Academic Press, San Diego, 1996.

[77] F.-X. Rong, "Liquid target pulsed laser deposition," *Applied Physics Letters*, vol. 67, no. 7, pp. 1022–1024, 1995.

[78] R. C. Budhani, P. Pant, R. K. Rakshit, K. Senapati, S. Mandal, N. K. Pandey, and J. Kumar, "Magnetotransport in epitaxial films of the degenerate semiconductor zn 1-xcoxo," *Journal of Physics Condensed Matter*, vol. 17, no. 1, pp. 75–86, 2005.

[79] J. H. Simmons and K. S. Potter, *Optical Materials*, Academic Press, New York, 2000.

[80] W. D. Callister, *Materials Science and Engineering: An Introduction*, John Wiley and Sons, New York, 1997.

[81] L. O. Grondahl, "The copper-cuprous-oxide rectifier and photoelectric cell," *Rev.Mod.Phys.*, vol. 5, no. 2, pp. 141–168, Apr 1933.

[82] A. O. Musa, T. Akomolafe, and M. J. Carter, "Production of cuprous oxide, a solar cell material, by thermal oxidation and a study of its physical and electrical properties.," *Solar Energy Materials and Solar Cells*, vol. 51, no. 3-4, pp. 305–316, 1998.

[83] N. Kikuchi and K. Tonooka, "Electrical and structural properties of ni-doped cu2o films prepared by pulsed laser deposition," *Thin Solid Films*, vol. 486, no. 1, pp. 33–37, 2005.

[84] M. Nolan and S. D. Elliott, "The p-type conduction mechanism in cu2o: a first principles study," *Physical Chemistry Chemical Physics*, vol. 8, no. 45, pp. 5350–5358, 2006.

[85] A. P. Young and C. M. Schwartz, "Electrical conductivity and thermoelectric power of cuprous oxide.," *Journal of Physics and Chemistry of Solids*, vol. 30, no. 2, pp. 249–252, 1969.

[86] A. E. Rakhshani, "The role of space-charge-limited-current conduction in evaluation of the electrical properties of thin cu2o films," *Journal of Applied Physics*, vol. 69, no. 4, pp. 2365–2369, 1991.

[87] G. P. Pollack and D. Trivich, "Photoelectric properties of cuprous oxide," *Journal of Applied Physics*, vol. 46, no. 1, pp. 163–172, 1975.

[88] W. H. Brattain, "The copper oxide rectifier," *Reviews of Modern Physics*, vol. 23, no. 3, pp. 203–212, 1951.

[89] M. Wei, N. Braddon, D. Zhi, P. A. Midgley, S. K. Chen, M. G. Blamire, and J. L. MacManus-Driscoll, "Room temperature ferromagnetism in bulk mn -doped cu2 o," *Applied Physics Letters*, vol. 86, no. 7, pp. 072514, 2005.

[90] Y. L. Liu, S. Harrington, K. A. Yates, M. Wei, M. G. Blamire, J. L. MacManus-Driscoll, and Y. C. Liu, "Epitaxial, ferromagnetic cu2 - x mnxo films on (001) si by near-room-temperature electrodeposition," *Applied Physics Letters*, vol. 87, no. 22, pp. 222108, 28 November 2005 2005.

[91] L. Pan, H. Zhu, C. Fan, W. Wang, Y. Zhang, and J. Q. Xiao, "Mn-doped cu2o thin films grown by rf magnetron sputtering," *Journal of Applied Physics*, vol. 97, no. 10, pp. 10–318, 2005.

[92] S. N. Kale, S. B. Ogale, S. R. Shinde, M. Sahasrabuddhe, V. N. Kulkarni, R. L. Greens, and T. Venkatesan, "Magnetism in cobalt-doped cu2o thin films without and with al, v, or zn codopants," *Applied Physics Letters*, vol. 82, no. 13, pp. 2100–2102, 2003.

[93] J. Antony, Y. Qiang, M. Faheem, D. Meyer, D. E. McCready, and M. H. Engelhard, "Ferromagnetic semiconductor nanoclusters: Co-doped cu2o," *Applied Physics Letters*, vol. 90, no. 1, pp. 013106, 1 January 2007 2007.

[94] M. Sieberer, J. Redinger, and P. Mohn, "Electronic and magnetic structure of cuprous oxide cu2o doped with mn, fe, co, and ni: A density-functional theory study," *Physical Review B (Condensed Matter and Materials Physics)*, vol. 75, no. 3, pp. 035203, January 15, 2007 2007.

[95] A. E. Rakhshani, "Preparation, characteristics and photovoltaic properties of cuprous oxide - a review.," *Solid-State Electronics*, vol. 29, no. 1, pp. 7–17, 1986.

[96] Y. Matsumoto, M. Murakami, T. Shono, T. Hasegawa, T. Fukumura, M. Kawasaki, P. Ahmet, T. Chikyow, S.-Y. Koshihara, and H. Koinuma, "Room-temperature ferromagnetism in transparent transition metal-doped titanium dioxide.," *Science (Washington, DC, United States)*, vol. 291, no. 5505, pp. 854–856, 2001.

[97] S. A. Chambers, S. Thevuthasan, R. F. C. Farrow, R. F. Marks, J. U. Thiele, L. Folks, M. G. Samant, A. J. Kellock, N. Ruzycki, D. L. Ederer, and U. Diebold, "Epitaxial growth and properties of ferromagnetic co-doped tio2 anatase," *Applied Physics Letters*, vol. 79, no. 21, pp. 3467, 2001.

[98] L. W. Guo, D. L. Peng, H. Makino, K. Inaba, H. J. Ko, K. Sumiyama, and T. Yao, "Structural and magnetic properties of mn3o4 films grown on mgo(0 0 1) substrates by plasma-assisted mbe.," *Journal of Magnetism and Magnetic Materials*, vol. 213, no. 3, pp. 321–325, 2000.

[99] A. Chartier, P. D'Arco, R. Dovesi, and V. R. Saunders, "Ab initio hartree-fock investigation of the structural, electronic, and magnetic properties of mn3o4," *Physical Review B: Condensed Matter and Materials Physics*, vol. 60, no. 20, pp. 14042–14048, 1999.

[100] Y. Petroff, P. Y. Yu, and Y. R. Shen, "Photoluminescence in copper(i) oxide.," *Physical Review B: Solid State*, vol. 12, no. 6, pp. 2488–2495, 1975.

[101] Y. Sun, K. Rivkin, J. Chen, J. B. Ketterson, P. Markworth, and R. P. Chang, "Strain splitting of 1s yellow orthoexciton of epitaxial orthorhombic cu2o films on mgo [110]," *Physical Review B*, vol. 66, no. 24, pp. 245315, DEC 15 2002.

[102] T. Ito, H. Yamaguchi, K. Okabe, and T. Masumi, "Single-crystal growth and characterization of cu2o and cuo.," *Journal of Materials Science*, vol. 33, no. 14, pp. 3555–3566, 1998.

[103] D. J. Kenway, C. Duvvury, and F. L. Weichman, "Evidence of a competitive phenomenon between the 0.72 mm and 0.93 mm luminescences of copper(i) oxide.," *Journal of Luminescence*, vol. 16, no. 2, pp. 171–175, 1978.

[104] N. Kikuchi, K. Tonooka, and E. Kusano, "Mechanisms of carrier generation and transport in ni-doped cu2o," *Vacuum*, vol. 80, no. 7, pp. 756–760, 2006.

[105] H. T. Cao, Z. L. Pei, J. Gong, C. Sun, R. F. Huang, and L. S. Wen, "Preparation and characterization of al and mn doped zno (zno: (al, mn)) transparent conducting oxide films," *Journal of Solid State Chemistry*, vol. 177, no. 4, pp. 1480–1487, 2004.

[106] Z.-B. Gu, C.-S. Yuan, M.-H. Lu, J. Wang, D. Wu, S.-T. Zhang, S.-N. Zhu, Y.-Y. Zhu, and Y.-F. Chen, "Magnetic and transport properties of (mn, co)-codoped zno films prepared by radio-frequency magnetron cosputtering," *Journal of Applied Physics*, vol. 98, no. 5, pp. 053908, 2005.

[107] M. A. Langell, C. W. Hutchings, G. A. Carson, and M. H. Nassir, "High resolution electron energy loss spectroscopy of mno(100) and oxidized mno(100)," *Journal of Vacuum Science Technology A: Vacuum, Surfaces, and Films*, vol. 14, no. 3, pp. 1656, 1996.

[108] J. Han, P. Q. Mantas, and A. M. R. Senos, "Defect chemistry and electrical characteristics of undoped and mn-doped zno," *Journal of the European Ceramic Society*, vol. 22, no. 1, pp. 49–59, 2002.

[109] Z. Zhou, K. Kato, T. Komaki, M. Yoshino, H. Yukawa, M. Morinaga, and K. Morita, "Effects of dopants and hydrogen on the electrical conductivity of zno," *Journal of the European Ceramic Society*, vol. 24, no. 1, pp. 139–146, 2004.

[110] N. Ohashi, J. Tanaka, T. Ohgaki, H. Haneda, M. Ozawa, and T. Tsurumi, "Isothermal capacitance transient spectroscopy for deep levels in co- and mn-doped zno single crystals," *Journal of Materials Research*, vol. 17, no. 6, pp. 1529–1535, 2002.

[111] F. P. D., J. Morales, W. E. L., E. Andrade, and M. Miki-Yoshida, "Influence of al, in, cu, fe and sn dopants in the microstructure of zinc oxide thin films obtained by spray pyrolysis," *Thin Solid Films*, vol. 366, no. 1, pp. 16–27, 2000.

[112] A. Bougrine, A. E. Hichou, M. Addou, J. Ebothe, A. Kachouane, and M. Troyon, "Structural, optical and cathodoluminescence characteristics of undoped and tin-doped zno thin films prepared by spray pyrolysis," *Materials Chemistry and Physics*, vol. 80, no. 2, pp. 438–445, 2003.

[113] J.-H. Lee and B.-O. Park, "Transparent conducting zno:al, in and sn thin films deposited by the sol-gel method," *Thin Solid Films*, vol. 426, no. 1, pp. 94–99, 2003.

[114] H. Sato, T. Minami, and S. Takata, "Highly transparent and conductive group iv impurity-doped zno thin films prepared by radio frequency magnetron sputtering," *Journal of Vacuum Science Technology A: Vacuum, Surfaces, and Films*, vol. 11, no. 6, pp. 2975–2979, November 1993 1993.

[115] E. Holmelund, J. Schou, S. Tougaard, and N. B. Larsen, "Pure and sn-doped zno films produced by pulsed laser deposition," in *Cola 2001*, Tsukuba, Japan, Oct 1 2001 2002, Dept. of Optics and Fluid Dynamics, Riso National Laboratory, DK-4000 Roskilde, Denmark, vol. 197-198, pp. 467–471, Elsevier Science B.V.

[116] I. Turkevych, R. Grill, J. Franc, P. Hoschl, E. Belas, P. Moravec, M. Fiederle, and K. W. Benz, "Preparation of semi-insulating cdte doped with group iv elements by post growth annealing," *Crystal Research and Technology*, vol. 38, no. 3, pp. 288–296, 2003.

[117] O. Panchuk, A. Savitskiy, P. Fochuk, Y. Nykonyuk, O. Parfenyuk, L. Shcherbak, M. Ilashchuk, L. Yatsunyk, and P. Feychuk, "Iv group dopant compensation effect in cdte," *Journal of Crystal Growth*, vol. 197, no. 3, pp. 607–611, 1999.

[118] T. Dietl, M. Sawicki, L. V. Khoi, J. Jaroszynski, P. Kossacki, J. Cibert, D. Ferrand, S. Tatarenko, and A. Wasiela, "Ferromagnetism in ii-vi compounds," *physica status solidi (b)*, vol. 229, no. 2, pp. 665–672, 2002.

[119] Y. Heo, Y. Kwon, Y. Li, S. Pearton, and D. Norton, "Properties of phosphorus-doped (zn,mg)o thin films and device structures," *Journal of Electronic Materials*, vol. 34, no. 4, pp. 409–415, 04/07 2005.

[120] R. Gresch, W. Mueller-Warmuth, and H. Dutz, "X-ray photoelectron spectroscopy of sodium phosphate glasses," *Journal of Non-Crystalline Solids*, vol. 34, no. 1, pp. 127–136, 1979.

[121] R. Franke, T. Chasse, P. Streubel, and A. Meisel, "Auger parameters and relaxation energies of phosphorus in solid compounds," *Journal of Electron Spectroscopy and Related Phenomena*, vol. 56, no. 4, pp. 381, 1991.

[122] C. H. Bates, W. B. White, and R. Roy, "The solubility of transition metal oxides in zinc oxide and the reflectance spectra of mn2+ and fe2+ in tetrahedral fields," *Journal of Inorganic and Nuclear Chemistry*, vol. 28, pp. 397–405, 1966.

[123] I. Horcas, R. Fernandez, J. M. Gomez-Rodriguez, J. Colchero, J. Gomez-Herrero, and A. M. Baro, "Wsxm: A software for scanning probe microscopy and a tool for nanotechnology," *Review of Scientific Instruments*, vol. 78, no. 1, pp. 013705, January 2007 2007.

[124] H.-T. Zhang and X.-H. Chen, "Controlled synthesis and anomalous magnetic properties of relatively monodisperse coo nanocrystals," *Nanotechnology*, vol. 16, no. 10, pp. 2288–2294, 2005.

[125] Y. Ichiyanagi, Y. Kimishima, and S. Yamada, "Magnetic study on co3o4 nanoparticles," *Journal of Magnetism and Magnetic Materials*, vol. 272-276, no. Supplement 1, pp. E1245–E1246, 2004/5.

[126] C. Song, F. Zeng, K. W. Geng, X. B. Wang, Y. X. Shen, and F. Pan, "The magnetic properties of co-doped zno diluted magnetic insulator films prepared by direct current reactive magnetron co-sputtering," *Journal of Magnetism and Magnetic Materials*, vol. 309, no. 1, pp. 25–30, 2007/2.

[127] K. Samanta, P. Bhattacharya, and R. S. Katiyar, "Optical properties of zn1-xcoxo thin films grown on al2o3 (0001) substrates," *Applied Physics Letters*, vol. 87, no. 10, pp. 101903, 2005.

[128] P. Koidl, "Optical absorption of co2+ in zno," *Physical Review B*, vol. 15, no. 5, pp. 2493–2499, Mar 1977.

[129] K. J. Kim and Y. R. Park, "Spectroscopic ellipsometry study of optical transitions in zn1-xcoxo alloys," *Applied Physics Letters*, vol. 81, no. 8, pp. 1420, 2002.

[130] M. Bouloudenine, N. Viart, S. Colis, and A. Dinia, "Bulk zn1 xcoxo magnetic semiconductors prepared by hydrothermal technique," *Chemical Physics Letters*, vol. 397, no. 1-3, pp. 73–76, 2004.

[131] S. V. Bhat and F. L. Deepak, "Tuning the bandgap of zno by substitution with mn2+, co2+ and ni2+," *Solid State Communications*, vol. 135, no. 6, pp. 345–347, 2005/8.

[132] X.-C. Liu, E.-W. Shi, Z.-Z. Chen, H.-W. Zhang, L.-X. Song, H. Wang, and S.-D. Yao, "Structural, optical and magnetic properties of co-doped zno films," *Journal of Crystal Growth*, vol. 296, no. 2, pp. 135–140, 2006/11.

[133] Y. R. Lee, A. K. Ramdas, and R. L. Aggarwal, "Energy gap, excitonic, and internal mn2+ optical transition in mn-based ii-vi diluted magnetic semiconductors," *Phys.Rev.B*, vol. 38, no. 15, pp. 10600–10610, Nov 1988.

[134] Y. Z. Peng, T. Liew, W. D. Song, C. W. An, K. L. Teo, and T. C. Chong, "Structural and optical properties of co-doped zno thin films," *Journal of Superconductivity*, vol. 18, no. 1, pp. 97–103, 02/01 2005.

[135] Y. Z. Yoo, T. Fukumura, Z. Jin, K. Hasegawa, M. Kawasaki, P. Ahmet, T. Chikyow, and H. Koinuma, "Zno-coo solid solution thin films," *Journal of Applied Physics*, vol. 90, no. 8, pp. 4246, 2001.

[136] U. Ozgur, Y. I. Alivov, C. Liu, A. Teke, M. A. Reshchikov, S. Dogan, V. Avrutin, S. J. Cho, and H. Morkoc, "A comprehensive review of zno materials and devices," *Journal of Applied Physics*, vol. 98, no. 4, pp. 041301, 2005.

[137] N. Khare, M. J. Kappers, M. Wei, M. G. Blamire, and J. L. MacManus-Driscoll, "Defect-induced ferromagnetism in co-doped zno," *Advanced Materials*, vol. 18, no. 11, pp. 1449, 2006.

[138] T. Chanier, M. Sargolzaei, I. Opahle, R. Hayn, and K. Koepernik, "Lsda + u versus lsda: Towards a better description of the magnetic nearest-neighbor exchange coupling in co- and mn-doped zno," *Physical Review B (Condensed Matter and Materials Physics)*, vol. 73, no. 13, pp. 134418, April 1, 2006 2006.

[139] W. Teizer, F. Hellman, and R. C. Dynes, "Hall effect at a tunable metal-insulator transition," *Phys.Rev.B*, vol. 67, no. 12, pp. 121102, Mar 2003.

[140] S. R. Shinde, S. B. Ogale, J. S. Higgins, H. Zheng, A. J. Millis, V. N. Kulkarni, R. Ramesh, R. L. Greene, and T. Venkatesan, "Co-occurrence of superparamagnetism and anomalous hall effect in highly reduced cobalt-doped rutile tio2-delta; films," *Physical Review Letters*, vol. 92, no. 16, pp. 166601–1, 2004.

[141] X. N. Jing, N. Wang, A. B. Pakhomov, and K. K. Fung, "Effect of annealing on the giant hall effect," *Physical Review B: Condensed Matter*, vol. 53, no. 21, pp. 14–032, 1996.

[142] J. C. Denardin, M. Knobel, X. X. Zhang, and A. B. Pakhomov, "Giant hall effect in superparamagnetic granular films," in *Vision Geometry VII*, San Diego, CA, United States, Jul 20-22 1998 2003, Inst. de Fisica Gleb Wataghin, Universidade Estadual de Campinas, Campinas S.P. 13083-970, Brazil, vol. 262, pp. 15–22, Elsevier.

[143] C. P. Bean and J. D. Livingston, "Superparamagnetism," *Journal of Applied Physics*, vol. 30, no. 4, pp. S120–S129, April 1959 1959.

[144] D. Jiles, *Introduction to magnetism and magnetic materials*, Chapman and Hall, London ; New York, 1998.

[145] P. A. Cox, *Transition metal oxides : an introduction to their electronic structure and properties*, Clarendon Press; Oxford University Press, Oxford; New York, 1995.

[146] T. Andrearczyk, J. Jaroszynski, G. Grabecki, T. Dietl, T. Fukumura, and M. Kawasaki, "Spin-related magnetoresistance of n-type zno:al and zn1 - xmnxo:al thin films," *Physical Review B (Condensed Matter and Materials Physics)*, vol. 72, no. 12, pp. 121309, September 15, 2005 2005.

[147] P. Stamenov, M. Venkatesan, L. S. Dorneles, D. Maude, and J. M. D. Coey, "Magnetoresistance of co-doped zno thin films," *50th Annual Conference on Magnetism and Magnetic Materials*, vol. 99, no. 8, pp. 08M124, 15 April 2006 2006.

[148] F. G. Pikus and G. E. Pikus, "Weak localization and negative magnetoresistance in wurtzite-type crystals," *Solid State Communications*, vol. 100, no. 2, pp. 95–99, 1996.

[149] Q. Xu, L. Hartmann, H. Schmidt, H. Hochmuth, M. Lorenz, R. Schmidt-Grund, C. Sturm, D. Spemann, and M. Grundmann, "Metal-insulator transition in co-doped zno: Magnetotransport properties," *Physical Review B (Condensed Matter and Materials Physics)*, vol. 73, no. 20, pp. 205342, May 15, 2006 2006.

[150] C. H. Park and D. J. Chadi, "Hydrogen-mediated spin-spin interaction in zncoo," *Physical Review Letters*, vol. 94, no. 12, pp. 127204, 2005.

[151] T. Lei, J. L. K.F., and T. D. Moustakas, "Heteroepitaxy, polymorphism, and faulting in gan thin films on silicon and sapphire substrates," *Journal of Applied Physics*, vol. 74, no. 7, pp. 4430–4437, October 1, 1993 1993.

[152] H. J. Kim, I. C. Song, J. H. Sim, H. Kim, D. Kim, Y. E. Ihm, and W. K. Choo, "Electrical and magnetic properties of spinel-type magnetic semiconductor znco[sub 2]o[sub 4] grown by reactive magnetron sputtering," *J. Appl. Phys.*, vol. 95, no. 11, pp. 7387–7389, June 1, 2004 2004.

[153] *Low Level Measurements Handbook: Precision DC Current, Voltage, and Resistance Measurements*, Keithley Instruments, INC., Cleveland, OH, 2004.

[154] D. C. Look, *Electrical characterization of GaAs materials and devices*, Wiley, Chichester ; New York, 1993.

[155] J. R. Lindemuth and B. C. Dodrill, "Anomalous hall effect magnetometry studies of magnetization processes of thin films," *Journal of Magnetism and Magnetic Materials*, vol. 272-276, pp. 2324–2325, 2004.

BIOGRAPHICAL SKETCH

Mathew Ivill was born in Ft. Myers, Florida. He was named after his grandfather, who also only had one 't' in his name. He grew up and attended school in the city of Cape Coral, Florida, where he lived with his parents, Richard and Linda, and older brother David.

Mathew began his undergraduate study at the University of Florida in 1996 (the year of UF's first national championship football title) and found his way into the Department of Materials Science and Engineering his sophomore year. In 2000, during his final year of undergraduate study, he began research in Dr. David Norton's group, growing epitaxial CeO_2 films on InP substrates. He later earned his B.S. in Materials Science and Engineering in the spring of 2001. He spent the following summer at Sandia National Lab in Livermore, CA, fabricating and testing samples to study the interface adhesion between PMMA and silicon (while also enjoying the beautiful national parks around California). Upon his return as a graduate student to the University of Florida, he began studying the effects of transition-metal doping in oxides for the field of spintronics. He was also fortunate enough to take some time off from his studies to live in London, England for 5 months. He has presented at 7 professional conferences, and was awarded the Grand Prize in Materials Science at the Florida Chapter of the American Vacuum Society, Orlando, two years in a row for his posters on transition-metal doped ZnO.

In his free time during graduate school, he was a member of the Gator Kendo Club. He has also enjoyed playing intramural softball with the Braised Cabbages.